Interreg
Italy - Croatia
ADRIREEF
European Regional Development Fund

EUROPEAN UNION

CNR
IRBIM
ISTITUTO PER LE RISORSE BIOLOGICHE E LE BIOTECNOLOGIE MARINE

Work Package 4.1

Monitoring case studies in Italy

Porto Recanati - Porto Potenza Picena Artificial Reef

Final report

Deliverables: D4.1.1, D4.1.2, D4.1.3, D4.1.4, D4.1.5, D4.1.6

Titles:
D4.1.1 Explorative survey with multibeam echosounder (MBES) and/or ROV/scuba
D4.1.2 Set up of an integrated monitoring system in situ
D4.1.3 Images and data transferred at land and visualized through different media
D4.1.4 Investigations through MBES carried out during the testing phase
D4.1.5 Extension of monitoring execution to other parameters (i.e. biological components)
D4.1.6 Collection and reporting of obtained data

Due date of deliverable: M22 **Actual submission date**: M32

Case study responsible PP: CNR-IRBIM

External expertise: D. Scaradozzi - Università Politecnica delle Marche - Italy

Authors: Fabi G., Armelloni E.N., Campanelli A., Ferrà C., Montagnini L., Moro F., Penna P. , Scanu M., Scaradozzi D., Spagnolo A., Strafella P., Tassetti A.N.

Role:

Coordination of activities: G. Fabi;
MBES: A.N. Tassetti (survey at sea, data analysis, reporting), A. Minelli (survey at sea);
Fixed near-real time oceanogranogranic monitoring system: P. Penna, F. Moro (design, realization, data collection, data analysis, reporting); G. Giuliani (realization);
Water column physical and bio-chemical parameters: A. Campanelli (data collection, data analysis, reporting), G. Caccamo, M. Betti (data collection), F. Grilli (data analysis);
Benthic communities: L. Montagnini (data collection and photo analysis); P. Strafella (photo analysis, reporting);
Mussel population: L. Montagnini (data collection, data analysis, reporting); E. Manini (microbiological analysis, reporting); A. Spagnolo (data analysis, reporting);
UVC: E.N. Armelloni, M. Scanu (underwater sampling, video analysis, recognition software development, data analysis, reporting); C. Ferrà (video analysis, recognition software development); L. Montagnini (ROV surveys); P. Penna, F. Moro (recognition software development, reporting);
3-D reconstruction: L. Montagnini (data collection); D. Scaradozzi (data analysis, reporting);
Report editing: G. Fabi, A. Spagnolo
Dissemination: F. Moro, P. Penna, A. Spagnolo.

Dissemination level:

PU	Public (must be available on the website)	[]
PP	Restricted to other programme participants (including the Commission Services)	[x]
RE	Restricted to a group specified below by the consortium (including the Commission Services)	[]
CO	Confidential, only for members of the consortium (including the Commission Services)	[]

Specified group (if applicable):

Table of contents:

EXECUTIVE SUMMARY

This report describes the results of a monitoring programme carried out from June 2019 until June 2021 at the artificial reef of Porto Recanati - Porto Potenza Picena (central Adriatic Sea), located in the coastal area of the Marche region, 5.6 km offshore and at 13.5m depth. The reef was chosen as a Case study within the Adrireef project as it can be considered as representative of the several artificial reefs deployed along the Italian coast of the central-northern Adriatic sea.

Monitoring of reefs is essential for the continuous evaluation of their structural and ecological evolution, hence their capacity of sustaining different economic activities, in line with the principles of Blue Economy. This activity, funded by the EU through the Interreg Italy-Croatia CBC programme, was initiated in recognition of the underexploited potential for sustainable use of some natural and artificial reefs located in the Adriatic Sea and is part of the Adrireef (Innovative exploitation of Adriatic Reefs in order to strengthen blue economy) project.

Aim of the project is a transborder investigation aimed at highlighting the unexploited potential of 7 selected reefs, natural or artificial, located offshore the Italian and Croatian coasts of the Adriatic Sea.

During the monitoring, innovative technologies with low environmental impact were tested, based on the outcomes of Adrireef WP3.4 “Identification of technologies for underwater monitoring of reefs”. However, a few modifications have been introduced to reflect Case Studies specifics or to address unexpected situations occurred during practical activities at sea.

At the Porto Recanati - Porto Potenza Picena AR geomorphological features and eventual changes in the physical structure of the reef, water column parameters, benthic communities and mussels population settled on the artificial structures, as well as finfish assemblage have been investigated using as much as possible innovative and eco-friendly technologies. In particular, an oceanographic observing system (fixed buoy), able to transfer data at land in real time, has been designed and realized to record water and atmospheric parameters, while benthic communities were investigated through photographic samplings. To evaluate the biomass of mussel population we had initially planned to develop a non-invasive methodology consisting of underwater photogrammetry associated with scraping samplings for photogrammetry validation but, due to the frequent poor visibility, the photographic set of suitable quality for processing was not sufficient; for this reason in 2021 we only proceeded with scraping sampling. Mussels were also analysed in terms of chemical, toxicological and microbiological contents. Finally, finfish assemblage was assessed using a combination of visual census methodologies: scuba divers and a remotely operated vehicle (ROV). At the same time, a software prototype to analyze, recognize and classify the images produced by both mono and stereo underwater image acquisition systems has been developed. In addition, underwater photos of a pyramid were taken for the 3-dimensional reconstruction of the structure through a novel methodological

approach collecting optical data for photogrammetric processing in poor visibility, highly biological structured environment.

The overall results indicate that the artificial reef of Porto Recanati - Porto Potenza Picena provides a range of ecosystem functions and services which could favour the development of new sustainable activities and/or the implementation of existing ones leading to an improvement of the local economy according to the principles of the Blue Growth. Considering the features of the reefs highlighted by the monitoring phase it results that the most suitable activities to be implemented in the area would be the professional small-scale fisheries with set gear, the collection of mussels settled on the man-made structures, the recreational fishing (e.g., fishing trips, fishing tourism) and diving. Obviously, the sustainable development of one or more of the above activities would necessarily require an adequate management aimed to avoid spatial conflicts and overexploitation of the reef resources.

1. INTRODUCTION

The artificial reef (AR) is located 5.6 km offshore between Porto Recanati and Porto Potenza Picena (central Adriatic Sea), facing the coastal plain shaped by the Potenza river (Figures 1.1 and 1.2). The site is approximately 10 km South of the Conero Promontory, and lies in the first portion of a flat and sandy coastline that continues uninterruptedly southwards until Pedaso. The area is mainly exposed to SE and NE winds and receives nutrient-rich fresh water input from the Potenza and the Musone rivers. The AR, deployed in spring 2001, lies at around 13.0 m depth on a flat sand-muddy seabed and is located far from natural and artificial hard substrates. Fine sediments with the presence of coarser fractions characterize the sea bottom, without any natural rocky outcrops or seagrass meadows. Poor underwater visibility is therefore very common due to current-induced suspension of sand and mud as well as to rivers' inflow.

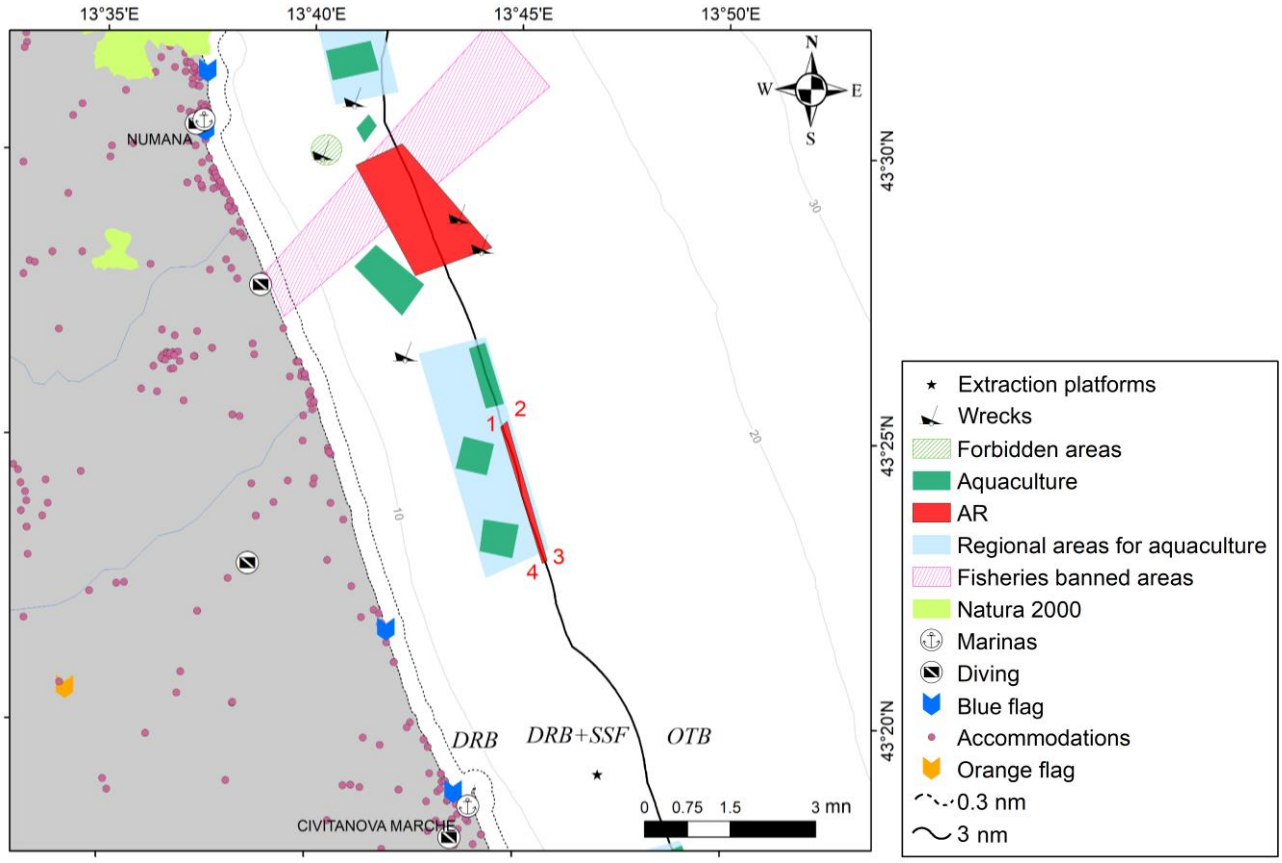

Figure 1.1 - Map of the artificial reef Porto Recanati - Porto Potenza Picena (1,2,3,4).

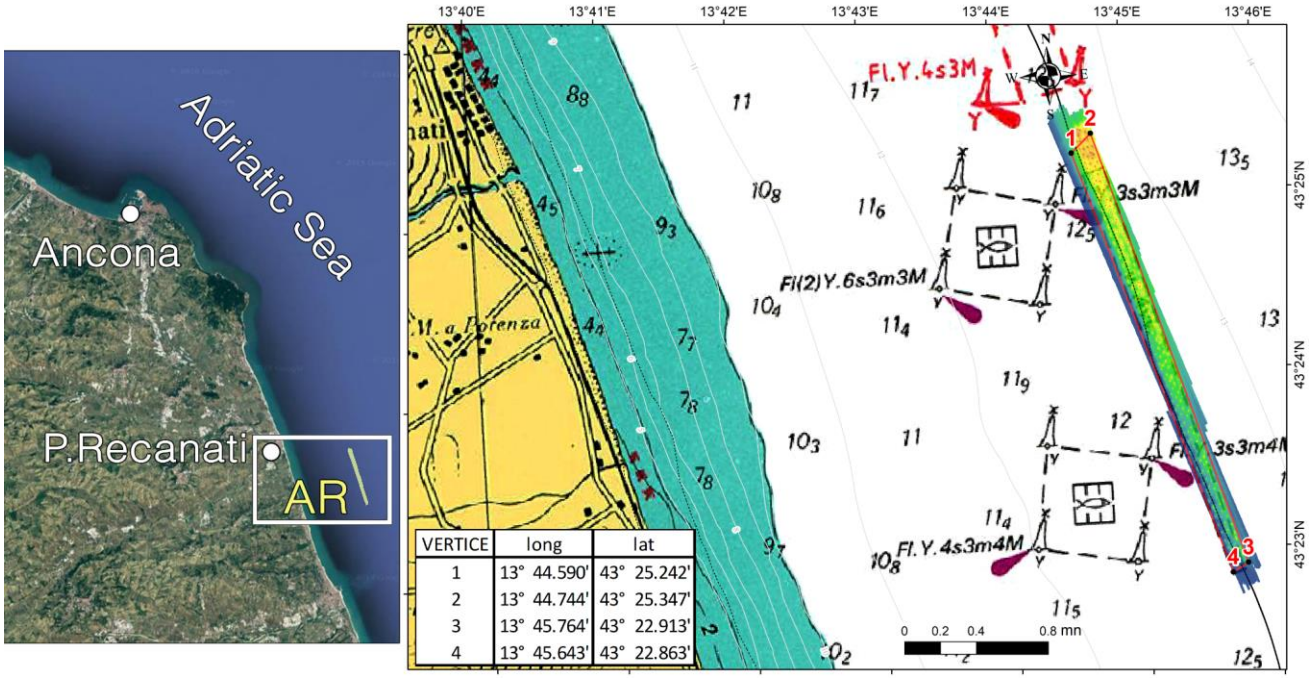

Figure 1.2 - Location of the AT (left) and its geographical coordinates obtained with multibeam echo sounder (right).

The AR covers an area of about 54.5 ha and consists of 252 pyramids positioned at a distance of around 60-80 m from each other and of 506 concrete poles. Each pyramid is made of five cubic concrete blocks (2x2x2 m), four at the bottom and one at the top (height: 4 m), having rough surfaces to promote the settlement of sessile organisms, and holes of different dimensions to provide shelter and habitat for various marine organisms. The concrete poles have a height of 4 m and are placed at regular intervals of around 20 m from each other, between the pyramids and along the reef perimeter.

Results obtained within the monitoring carried out over five years after the reef deployment have shown qualitative and quantitative changes in benthic and fish communities. These observations rely on studies conducted when the AR was still a “young” reef, where both the biological and ecological processes were likely to be ongoing. It is well-known that on ARs, like any hard substrate, a series of progressive modifications in the structure of benthic and ephibenthic communities might occur, leading to sequences of colonization, the presence of steady-states, and even possible “regression phases'' characterized by a reduced amount of species. Indeed, the absence of detailed information on the biotic communities inhabiting the reef may hamper the sustainable and ecologically responsible management of future fishery systems in the area. Thus, specific studies on the ecological state after 20 years of deployment have been useful either to gain a better understanding of the ecological role of the AR and to obtain useful information for maximizing the effectiveness of future installations. In addition, updating information on the ecological

status is useful to better identify the possible optimal utilization of the reef, following the principles of the Blue economy.

Unfortunately, due to numerous factors including the Covid-19 pandemic, it was not possible to exactly apply the monitoring as planned and described in the Deliverables of Activity 3.4. However, the applied methodologies were thought to pursue three main objectives: to create a data set useful to promote the AR usages, monitor the biological status of the reef, and develop and test low impact, automated sampling and novel methodologies.

The artificial reef of Porto Recanati - Porto Potenza Picena was selected as Case study among the ARs deployed in the Marche coastal area based on the results of an exploratory survey with a multibeam echosounder (MBES) conducted in 2018-2019. That survey was also useful to assess the bulk volume of the AR and to produce an updated map of the site. Considering the extent of the structure, it allowed us to identify 3 sampling sub-areas within the AR, described in the following paragraphs. A second survey was carried out during the monitoring phase to investigate eventual changes in the physical structure of the reef.

A fixed buoy equipped with a solar panel, rechargeable battery, a data logger and a router + 4G antenna was moored at the AR. This setting enabled continuous sampling, and real-time data transmission of a few water column parameters from the core of the reef.

All the remaining samplings were performed in each sub-area, in order to consider the possible presence of a North-South gradient. The mussel coverage and biomass were investigated since 2019 through photogrammetry technique but, due to the difficulty to take highly optimized photos in poor environmental conditions (frequent high turbidity), only the data from scraping carried out in 2021 were utilized.

Photographic samples of the benthic community settled on the reef were also collected on a biannual basis, while the fish assemblage was assessed on a monthly basis using a combination of visual census methodologies: scuba divers and a remotely operated vehicle (ROV). Finally, underwater photos of a pyramid were taken for the 3-dimensional reconstruction of the structure.

2. GEOMORPHOLOGICAL MAPPING

2.1. Description of equipment and acquisition/processing techniques

An exploratory MBES survey was carried out in December 2018-February 2019 to identify the most suitable artificial reef to be used as Case study, among those that are deployed along the Marche Region coast. A second MBES survey in December 2020 was considered necessary to investigate morphological changes because during one of the scuba surveys one concrete pyramid was found to have collapsed.

Measurements were made with a Kongsberg EM2040CD MBES from CNR-IRBIM's 14 m-long research vessel, Tecnopesca II (Figure 2.1). The EM2040CD is a compact, dual-transducer version of the EM2040 MBES designed primarily for seafloor-echo detection at ranges < 600 m. The transducers are hull-mounted at ~0.8 m depth. Each transducer yields a 2D fan ("swath") of backscatter samples within an array of 400 beams.

Figure 2.1 - EM2040DC multibeam echosounder (left) hull-mounted on R/V "Tecnopesca I" (right).

A number of parameters are configurable by the user within the Kongsberg Seafloor Information System (SIS) software, from which the system determines the number, steering angle, spacing and opening angle of the beams in the swath (Figure 2.2).

Water sound speed was measured continuously with a miniSVS Sound Velocity Sensor mounted close to the transducers to enable real-time beamforming and sample-range calculation by the Seafloor Information System (SIS) software. During multibeam surveys, sound velocity profiles (SVP) were also collected at a minimum of twice daily, once in the morning and once in the afternoon. This was adequate since little to no stratification of the water column was present.

The beam steering angles and sample depths were corrected for vessel pitch, roll, heave and yaw in real time using measurements from a Kongsberg Seatex Motion Reference Unit MRU 5 and an Anschütz Gyro Compass Equipment Standard 20 Compact Type 110–222 NG001.

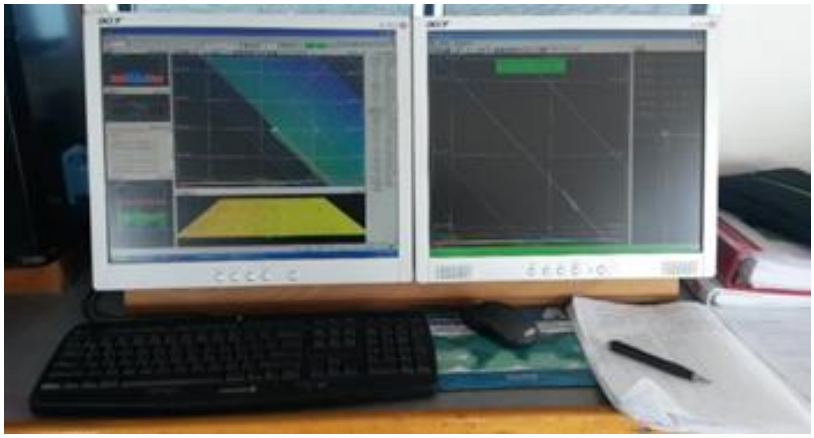

Figure 2.2 - On board dedicated hydrographic workstation and Seafloor Information System (SIS) user interface for data acquisition and control.

The vessel location was measured with an SPS855 GNSS Modular Receiver and all sensors were synchronised to the GPS-measured UTC time. The time-referenced vessel position and attitude, and MBES beam-steering angle, sample range and sample backscattering magnitude for each ping were saved to a series of proprietary-format binary data files with .ALL filename extensions, combining the positioning, attitude, sound velocity and sounding data.

Surveys consisted of 31 evenly spaced, parallel transects ~ 4/5 km in length (Figure 2.3 left). The transects were run in alternating North-South direction at ~2 to 2.6 m/s (~4 to 5 knots) and ~360 kHz, choosing the spacing between transects (~20 m) based on the water depth to ensure a minimum of 30% across-swath overlap between adjacent lines. Overlap provided data redundancy and worked as a safeguard when swath width was reduced due to unexpected changes in seafloor type or during a rapid change in vessel direction (resulting in a data gap). The seafloor was detected in real time from the MBES measurements by the SIS software using the “Tracking” detector mode, since reef modules and related sudden depth changes were expected on the seafloor.

Sounded poles were annotated during the acquisition using the tools provided in the SIS planning module, and additional 165 lines were acquired in East-West directions switching where necessary to “Minimum Depth” detector mode to better sound concrete poles.

The SIS-detected seafloor depth and backscatter measurements were processed with CARIS HIPS & SIPS software, taking into account tide corrections, manual editing and quality control tools. A Digital Terrain Model (DTM) of the seafloor was created as a Combined Uncertainty and Bathymetry Estimator (CUBE) surface with a resolution of 0.2 m (Figure 2.3 right).

The CUBE-based editing also enabled the identification of erroneous data and the quality control of the soundings. Gridded bathymetric data were delivered in UTM 33N WGS84 and with a resolution of 0.20 m (XYZ ASCII and GeoTiff file formats). Bathymetric charts and isobaths (0.25 m intervals) are added in Annex I - Bathymetric maps (Pdf file format).

FInally, a difference surface was generated from the two bathymetric models (2019 and 2020) to investigate morphological changes over the monitoring years.

The equipment and software we used for both surveys is summarized below:

- EM2040DC (Kongsberg, Kongsberg, Norway) multibeam sonar with operating frequency of 200-400 kHz, maximum swath width 130 °, number of beams (dual swath) 800, and beam width of 1x1° at 400 kHz. The multibeam echosounder is permanently hull-mounted on R/V “Tecnopesca I”;
- SPS855 GNSS Receiver (sampling rate 2 Hz, Trimble, Sunnyvale, CA, USA) for positioning with Omnistar HP/XP/VBS subscription;
- Sensor for motion compensation Kongsberg Seatex MRU 5 and Anschütz Gyro Compass Equipment Standard 20 Compact Type 110–222 NG001 (0.02° roll and pitch accuracy, and 0.1° heading accuracy; Raytheon Anschütz, Kiel, Germany);
- Real-time sound velocity probe Valeport MiniSVS (Valeport, Devon, UK) at the sonar head. It is installed in a fixed position above the transducer, thus supporting beam steering control of the data;
- Probe AML Oceanographic Smart SV&P, providing corrections for the sound velocity profile through the entire water column.
- Seafloor Information System (SIS) software , for data acquisition and control;
- Teledyne Caris Hips and Sips Version (version 11.0, Teledyne, Fredericton, NB, Canada) and QPS Fledermaus (version 7.8.0, Quality Positioning Services B.V., Zeist, The Netherlands) software, for post-processing, cleaning, correcting and valorization of multibeam sounding data.

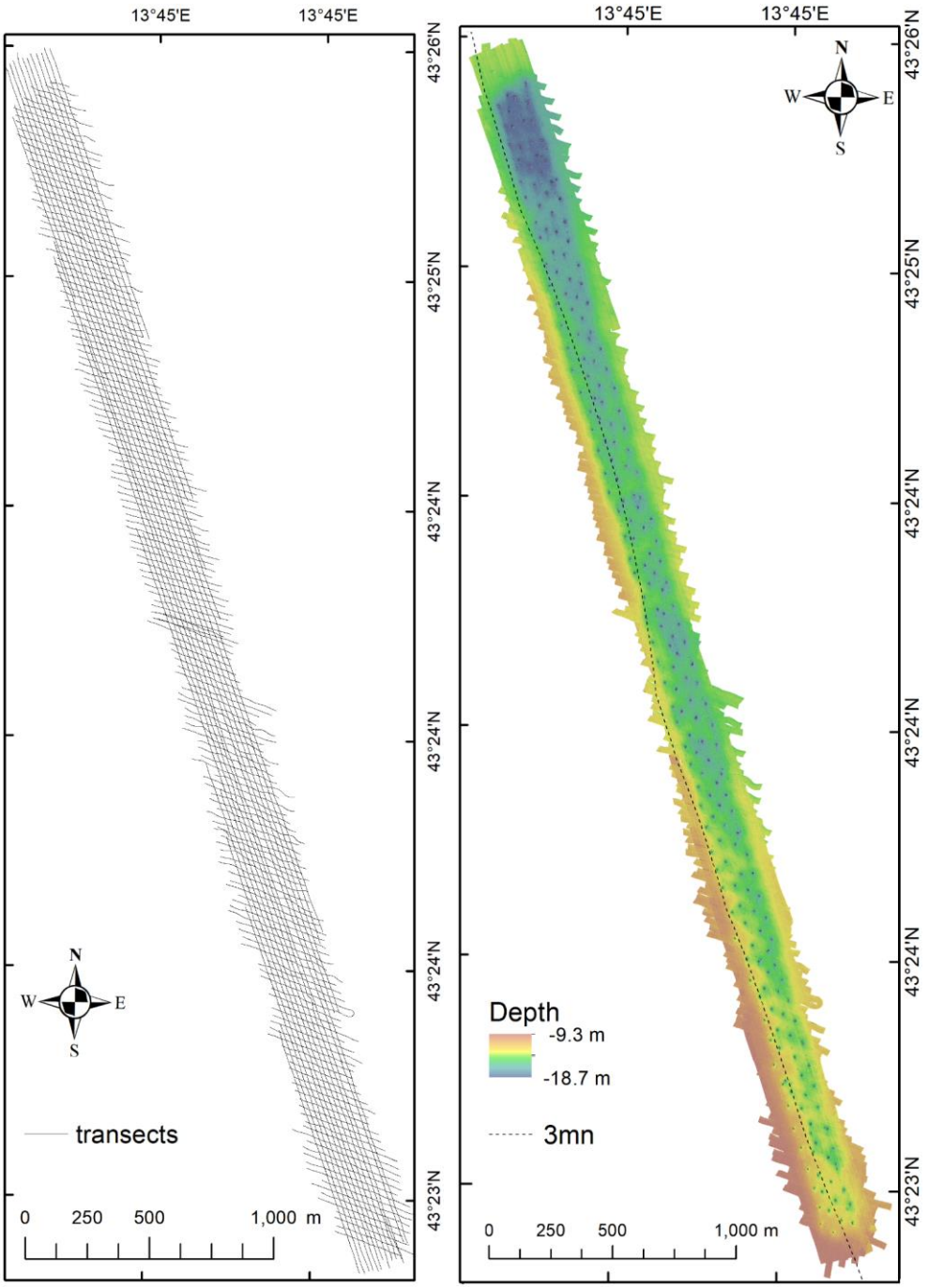

Figure 2.3 - Planning of MBES acoustic survey (left) and hill-shaded bathymetric map (right).

2.2. Survey results

MBES enabled the characterization of the Porto Recanati – Porto Potenza Picena AR in terms of compliance with the original drawing and structural integrity.

The detail and coverage provided by the multibeam sonar, along with the ability to render and visualize the seafloor bathymetry and every single AR structure in 3D, allowed to map the reef and measure its units at the snapshots on time represented by the two MBES surveys (December 2018 and December 2020).

The sounded structures were perfectly identifiable and dimensionally correct (Figure 2.4), and quite in line with the original schematic plan (Figure 2.5) that placed 252 2-layer pyramids following a 60 x 60 m grid and 506 poles among the pyramids to give a structural continuity and increase the ecological functionality of the artificial reef.

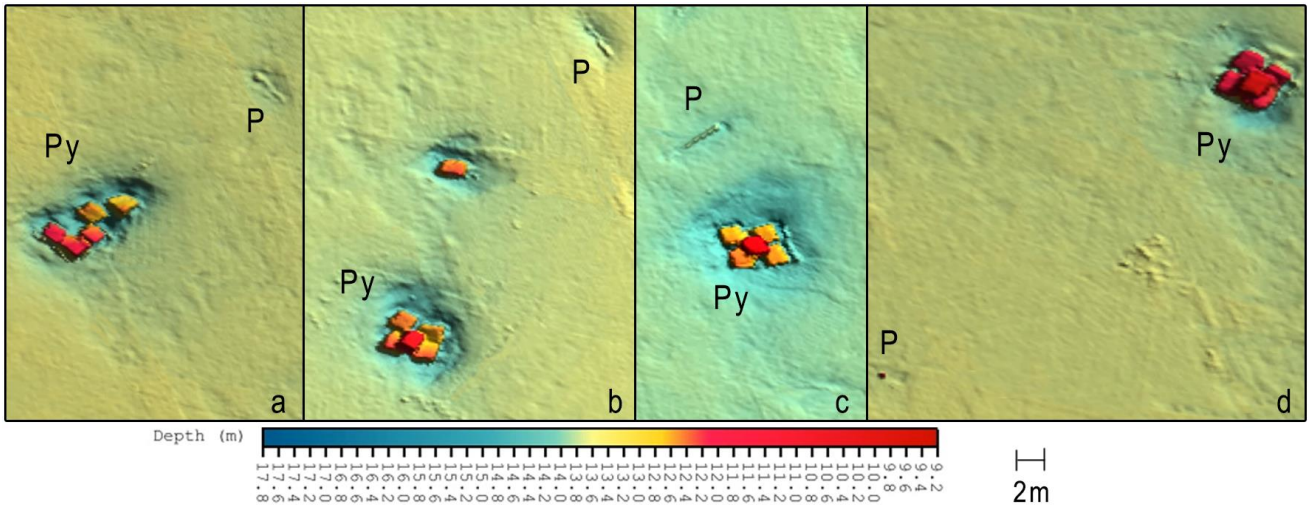

Figure 2.4 - Structures of the reef of Porto Recanati – Porto Potenza Picena: 2-layer pyramids (Py) and poles (P). Examples of a collapsed pyramid (a) and collapsed poles (a, b and c), a not-intact pyramid (b), two undamaged pyramids (c and d) and a standing pole (d).

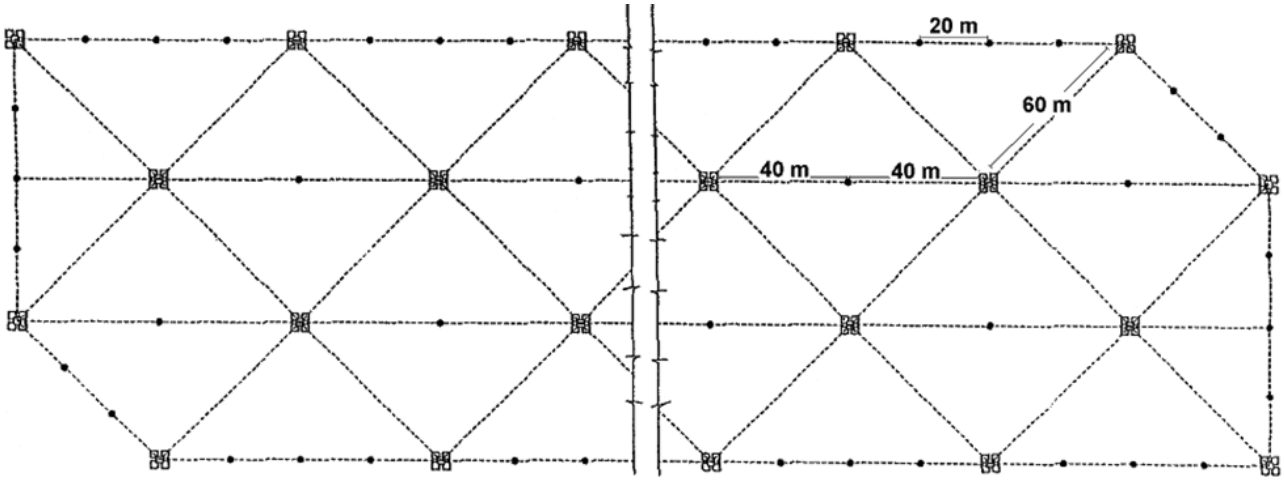

Figure 2.5 - Original schematic plan of the Porto Recanati – Porto Potenza Picena AR.

In 2018 most of the concrete poles were found to have collapsed, while the pyramids were mostly intact (Figure 2.6), even though slight scour signatures had been well depicted at the sides of the concrete bases underlying the pyramids, followed by banks of removed substrate.

The mean depth of the ambient seafloor was measured at 13.5 m, while the minimum depth of the top of the poles was measured to be 9.3 m.

A deepening of the whole AR area was clearly visible only in the northern part of the reef, where the mean depth was 14.00 m with the inner seafloor 0.30 m deeper than the outer surface (Figure 2.3 right).

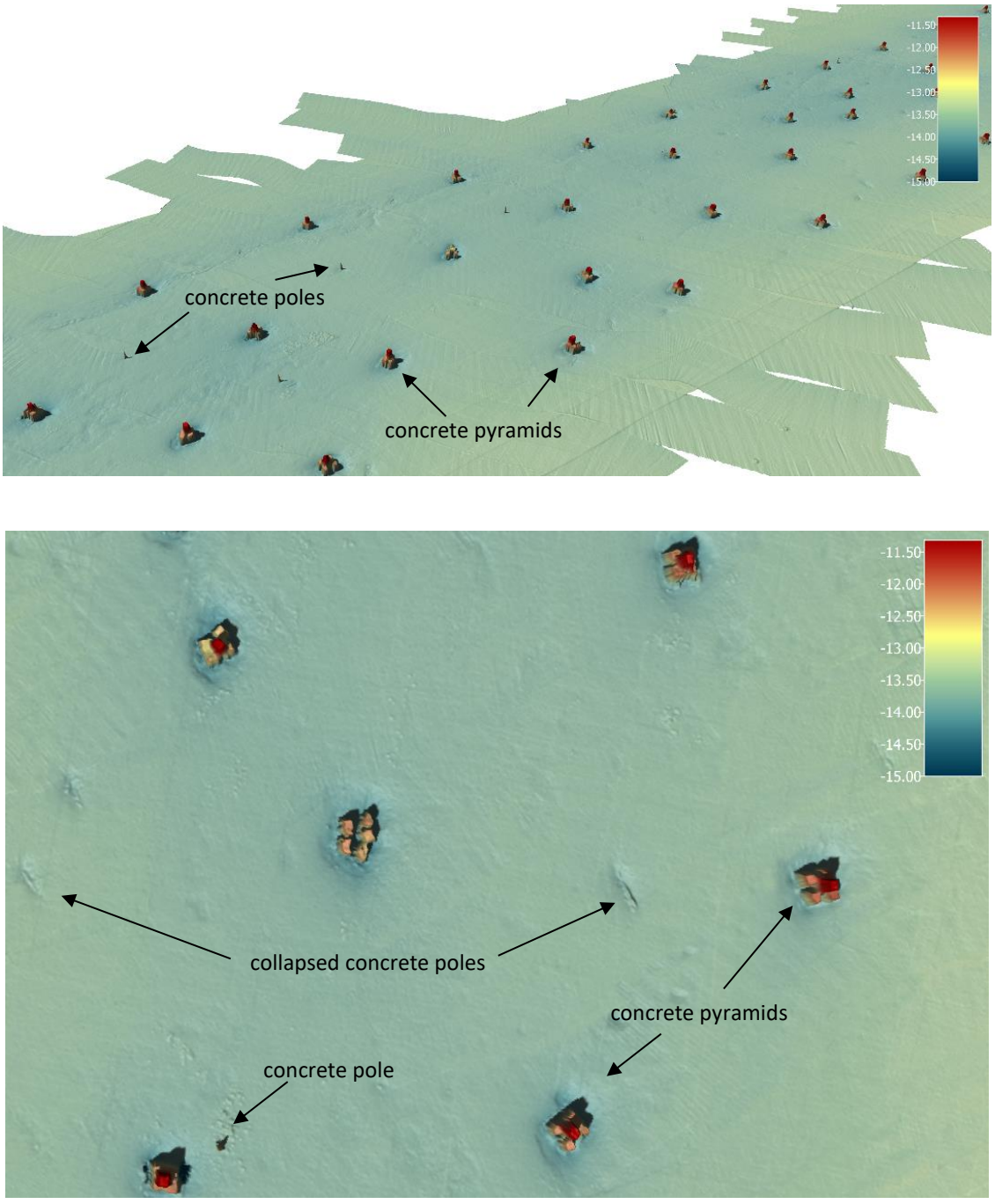

Figure 2.6 - 3D perspective close-up views of the artificial reef and its structures (concrete poles and pyramids).

The difference between surfaces, created by subtracting the bathymetric grid of the survey 2018 from the surface 2020, was minimal, with a mean absolute difference on the order of a few centimeters. It showed barely visible areas of deposition (positive values, red areas in Figure 2.7) and erosion (negative values, blue areas in Figure 2.7) between the two surveys, and enabled rapid verification of the collapse of two pyramids.

No additional significant collapses were observed in 2020, while some smaller vertical/horizontal movements of the single units had kept on occurring and scour signatures had been well depicted, likely as a consequence of the local currents (cfr. Chapter 4.1).

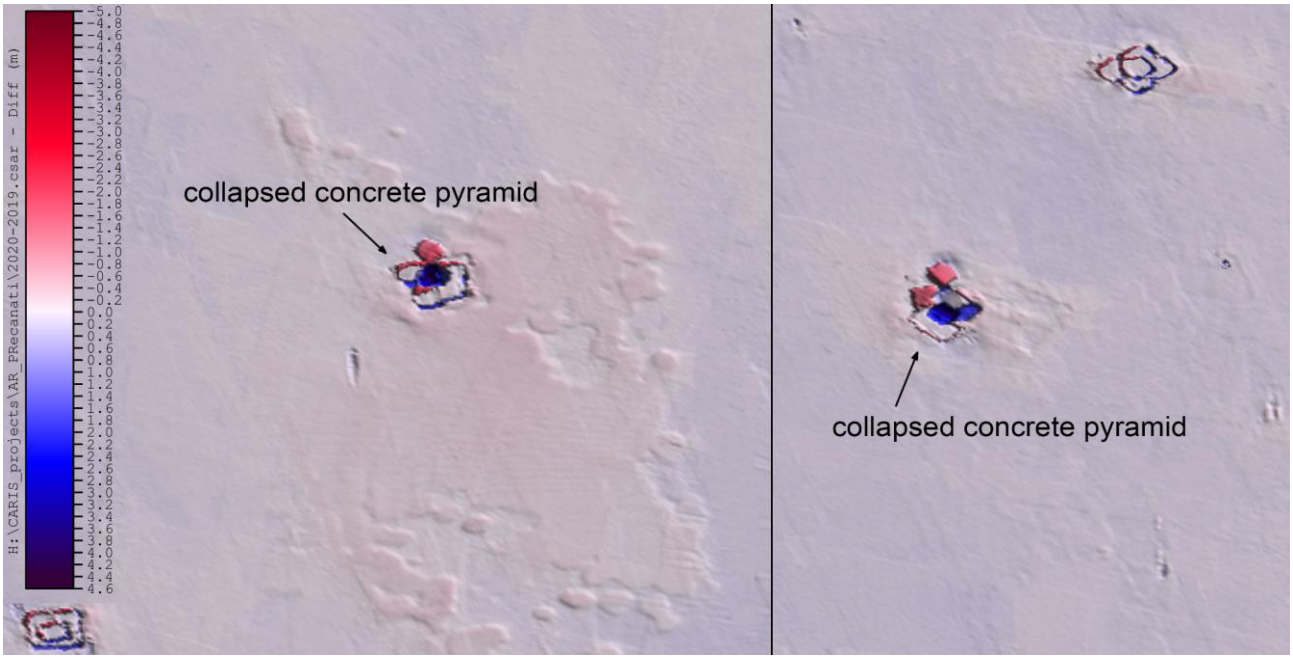

Figure 2.7 - Difference surface 2020-2018 and the collapse of 2 pyramids. Positive values (in red) highlight concrete blocks that collapsed in 2020, and so sounded in that position only in 2020. Their position in 2018 was in correspondence with negative values (in blue).

The outcomes obtained so far suggested how a multibeam echosounder, if foreseen in a systematic monitoring program, might be key in drawing post-reef deployment comparisons and gaining a mechanistic and predictive understanding of how the reef functions ecologically and physically during its life.

The explorative MBES survey was useful for planning other investigations and in particular:

- the continuous water monitoring, by identifying the best location to fix the oceanographic buoy (Figure 2.8); this was chosen in the middle and inner side of the AR, in order to avoid impact on its structures and prevent loss or damage of the buoy caused by trawling;
- the visual census and 3-dimensional reconstruction samplings, by identifying 3 suitable sub-areas, one in the North, one in the center, and one in the South of the AR (A, B and C respectively, Figure 2.9); these were selected in order to be comparable in terms of structures involved (2 standing poles and 2 pyramids in each sub-area) and to be easily sampled by scuba divers (without having to dive excessively long distances between structures).

Finally, a more readable map of the northern part of the AR (with explicit coordinates and distances between structures) was produced and distributed to fishers which are active in this area (Annex II - Map for fishers, Pdf file format) in order to encourage their involvement.

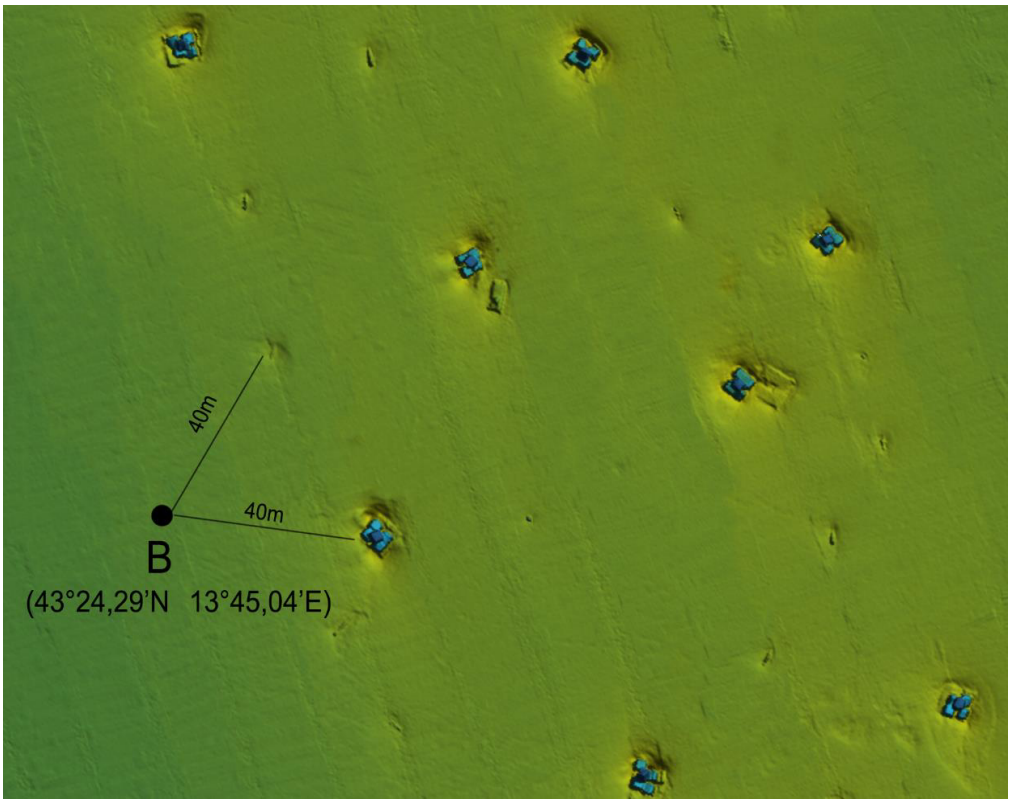

Figure 2.8 - Position of the fixed buoy (B) that was moored in correspondence with the central sub-area B.

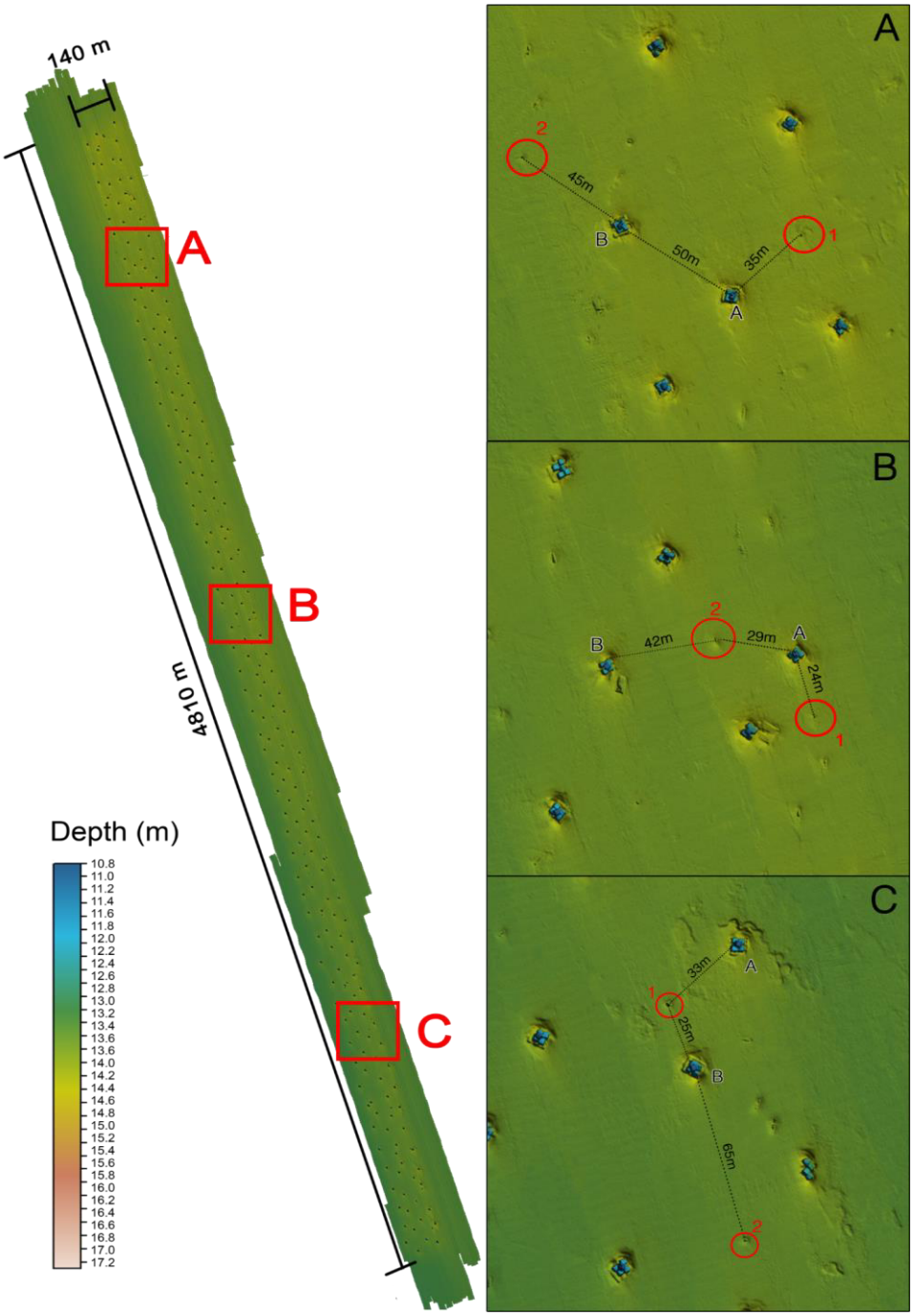

Figure 2.9 - Sampling sub-areas and related transects between structures (2 standing poles and 2 pyramids).

3. SAMPLING TECHNIQUES AND METHODS OF ANALYSIS

3.1. Speed and direction of water currents

The measurement of physical (intensity of flows and direction, temperature, salinity, turbidity and dissolved oxygen) and chemical (nutrients, organic matter, toxic contaminants) parameters of the water column was carried out at different temporal and spatial scale by a fixed near-real time oceanographic observing system buoy (Chapter. 3.1.1) and by means of oceanographic campaigns carried out by boat (Chapter 3.2.1).

3.1.1. Data Collection

The development of the real time oceanographic observing system required several steps: (i) research and purchase of an oceanographic buoy suitable for our purposes, (ii) design and implementation of the hydro-meteorological monitoring system; (iii) collection of meteorological/hydrological data; (iv) implementation of the freely accessible database.

Following the study of reliability and best quality/price ratio, a FLOATEX oceanographic buoy was purchased (Figure 3.1.). In addition, the mooring line, composed of a ballast of about 1000 kg and 24 m of iron chain with a diameter of 25 cm, was designed and constructed (Figure 3.2).

Figure 3.1 - Rendering of the buoy without any sensor.

Figure 3.2 *- Mooring system of the buoy composed of a ballast of about 1000 kg and 24 m of iron chain with a diameter of 25 cm.*

The second step was the design of the system and modules necessary to collect the water parameters. Once the fundamental parameters were selected, the most suitable sensors and equipment were identified from the market (Annex III). The system consists of a datalogger (central unit) with the functions of managing the communication with the sensors and data collection, a compact weather station, a router LTE, an optical oxygen sensor, a sensor for water temperature and salinity, an optical turbidity sensor, and an Acoustic Doppler Current Profiler (ADCP).

The ADCP was programmed with 10 cells (also called bin) of 1 meter. It is provided with an internal high accuracy, full 3D Attitude and Heading Reference Sensor (AHRS) which compensates for the oscillations of the buoy caused by the wave motion. Precise synchronization is required because the lag between velocity and orientation measurements translates into discrepancies between where the ADCP computes the location of each bin, and their true location in the water column (Figure 3.3).

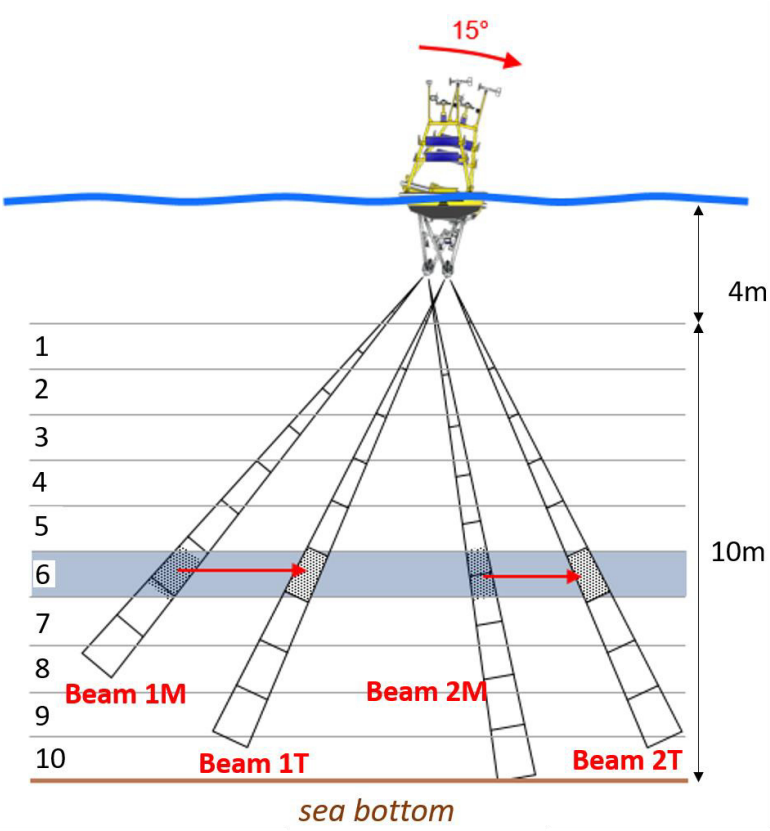

Figure 3.3 - Vertical arrangement of the cells from the surface to the bottom and example of translation of the measure from field measures (beam 1M and 2M) to true values (Beam 1T and 2T). The translation is automatically calculated by the ADCP through AHRS and its internal magnetometer and accelerometer. Modified from Velasco et al., 2018.

The third step was to study in depth the subsystems and sensors, taking particular care of communication, energy consumption, physical connection, and the format of the data output (Figure 3.4). During this activity, the most delicate procedure consisted of the implementation and test of the scripts for the management of communication, data reading and data transfer between the datalogger and each sensor.

Subsequently, a complete abstracted firmware was implemented: all the source codes produced in the previous step were integrated into subroutines and functions were inserted into a complete reading cycle performed every 20 minutes (the sensor reading routines are performed almost continuously and subsequently processed every 20 minutes). The router was then integrated and a new routine for the management of connection was implemented. Being the system powered by 2 battery packs and 2 photovoltaic panels (it was not possible to insert additional batteries due to the buoy stability), the firmware was optimized to save energy (management of sensor sleep mode, optimization of router consumption, etc.). The data collected by the datalogger are sent to a remote CNR server in real-time every 20 minutes.

Figure 3.4 - Testing phase in the laboratory.

A specific software (alert tool) that analyzes the data in real time has been implemented to make it possible to check the data quality assurance and to know the operating status of the equipment. In case of malfunctions in data transmission or/and inconsistent data, an error message is sent to the system managers via e-mail and telegram application. In addition, the alert system sends a notification in case of significant wave motion (it analyzes the tilt values of the weather station and ADCP), if there are out-of-scale (or sensor drifting or freezing) values of the main physical measured parameters (Figure 3.5) and/or if the buoy position deviates significantly from the assigned area.

Finally, a free accessible data presentation platform was implemented using a web solution provided by Grafana Labs To make the data publicly available (Annex IV).

Figure 3.5 - Alert tool: example of Telegram notification.

After the testing phase, the submerged part of the buoy was covered with a specific antifouling paint (Figure 3.6). The buoy was deployed at sea (Figure 3.7) in the pre-established area (Figure 2.8) on July 2, 2020 and was operational until October 22, 2020 when it was recovered to avoid the risk it could be damaged or lost due to the winter storms. The buoy was positioned again at sea on May 26, 2021 (Figure 3.8) and it is currently operational.

Figure 3.6 - The system ready for deployment.

Figure 3.7 - Meteo-oceanographic buoy deployment (July 2, 2020).

Figure 3.8 - Meteo-oceanographic buoy deployment (May 26, 2021).

3.1.2. Data Analysis

CNR staff has developed a MySQL database and a procedure to collect and analyze the physical data received from the buoy and other ancillary data. An automatic script checks data consistency and supports operators in data validation, generating a QC dataset. The interoperability of data is guaranteed by the use of an internationally recognized vocabulary (NERC) and standardized data format (ODV Ocean Data View).

A transformation from cartesian (East-North) to polar (intensity and direction) was applied for easier data management and visualization. Particular attention was paid to the analysis of ADCP data during the post processing phase, in particular for amplitude and correlation data. The instrument works by measuring the reflection of an acoustic signal from particulate matter in the water. *Amplitude*, or signal strength, is the strength of the return signal for each beam and is output in dB. Amplitude decreases with the distance from the instrument and also establishes the maximum usable range (in our application is the bottom detection at 14 meters). The *correlation* is a statistical measure of similar behaviour between two variables which in our case are the received signals with respect to time. Correlation is output in %, where 100% means perfect correlation and 0% means no similarity. The magnitude of the correlation is thus a quality measure of the velocity data, and as the correlation decreases so does the data accuracy.

The Nortek Signature500 ADCP (Annex III) was programmed with 14 bin, 1 meter wide cells where the currentometer measures the current by means of acoustic signals (Figure 3.3). All velocity, direction, amplitude and correlation data were stored as raw data for each of the 14 bin cells.

The ADCP has been fixed to the buoy at a depth of 3.5m, to which a surface layer of 0.5m of blank must be added where the ADCP is unable to measure for physical and structural reasons. Considering that the current data refer to the center of the cell (in our case 1 meter) and adding the distances described above, the measurements obtained by the ADCP in bin cell number 1 refer to a height of 4.5m from the surface. In the same way, cells 5 and 9 refer to heights of 8.5 and 12.5 meters respectively. Figure 3.9 shows the amplitude [dB] and the correlation [%] recorded at each measurement made by the ADCP for each cell and each ping.

In order to filter only the valid data produced by the ADCP, a specific quality check script was created with a threshold of amplitude >60 and correlation >70 as indicated by the manufacturer Nortek (Principles of Operation – Signature, https://support.nortekgroup.com/). The script allows to mark every single record of measures with a specific flag (flag = 4 = bad) making it easy to filter the valid data discarding all the values with this flag.

The amplitude trends are very good, while for the correlation there are surface disturbances due to the wave motion or to the position of the mooring chain which sometimes aligns with the ADCP beam. Close to the bottom some data are not perfectly correlated as well, and also in this case they are due to the vertical oscillations of the buoy which approaches the instrument towards the bottom.

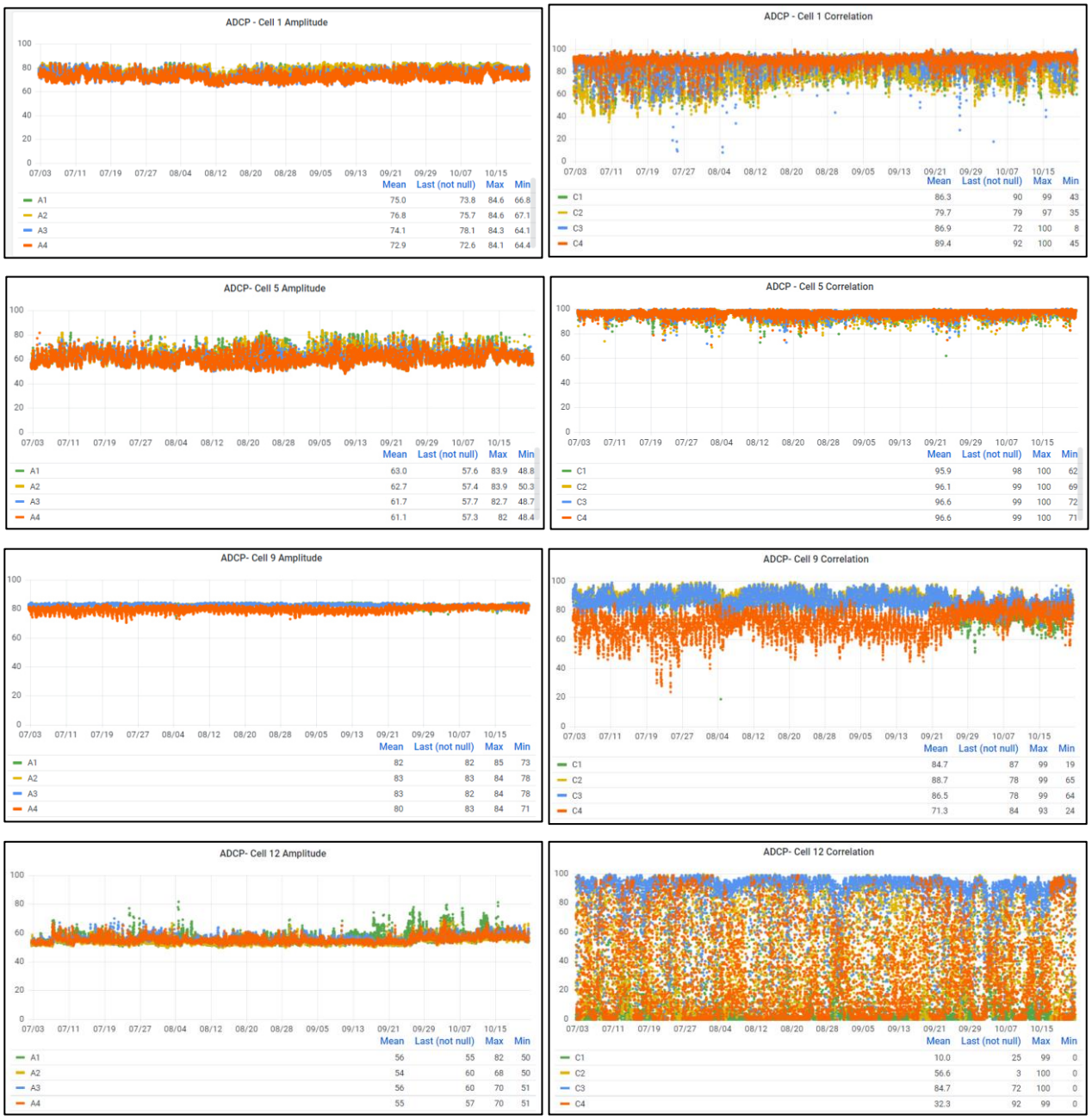

FIgure 3.9 - Amplitude (left) and correlation (right) values for 4 bin cells (1-5-9-12). Data shown are not filtered and they refer to the deployment in 2020. Notice the very low amplitude and correlation values for cell n. 12 which is located at a depth beyond the seabed.

The data corresponding to cell number 10 were discarded after QC but could still be retrieved after a more thorough post-processing. Cells from 11 to 14 were discarded a priori as the return signals were strongly disturbed, but they were used to ensure adequate power of the acoustic signal to reach the bottom even in the event of high tide or rough sea.

Taking into account the above considerations and with the aim of fully characterizing the water column with regard to sea currents, cells n. 1, 5 and 9 corresponding to a depth of 4.5, 8.5, 12.5m respectively from the surface were selected for this study.

Considering that the currentometer is installed downlooking and that the buoy is subjected to strong oscillations caused by the wave motion (Figure 3.10), the produced filtered measurements can be considered excellent, having reached over 99% of valid data during the overall monitoring period.

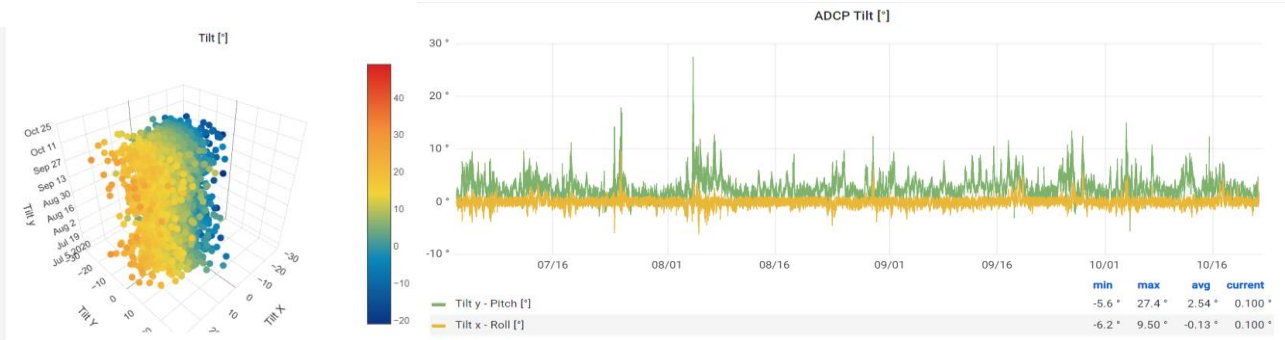

Figure 3.10 - Compact meteo station (left) and ADCP (right) tilt time series during deployment in 2020. The figure shows the oscillations (pitch and roll) of the buoy caused by the wave motion.

3.2. Water column parameters

3.2.1. Data Collection

The measurement of water column physical (temperature, salinity, and turbidity) and bio-chemical (nutrients, dissolved oxygen and chlorophyll as fluorescence) parameters other than current speed and direction was carried out at different temporal and spatial scale, by the fixed near-real time oceanographic observing system (cfr. Chapter 3.1) and by means of oceanographic campaigns.

A total of four oceanographic cruises were carried out in the period October 2020 - June 2021. Data were collected in n. 7 stations located within the AR (Figure 3.11) on October 22, 2020; January 20, 2021; May 11, 2021 and June 22, 2021.

Temperature, salinity, oxygen and turbidity data were collected both with the sensors mounted on the buoy (in real time, every 20 minutes) and during the oceanographic cruises.

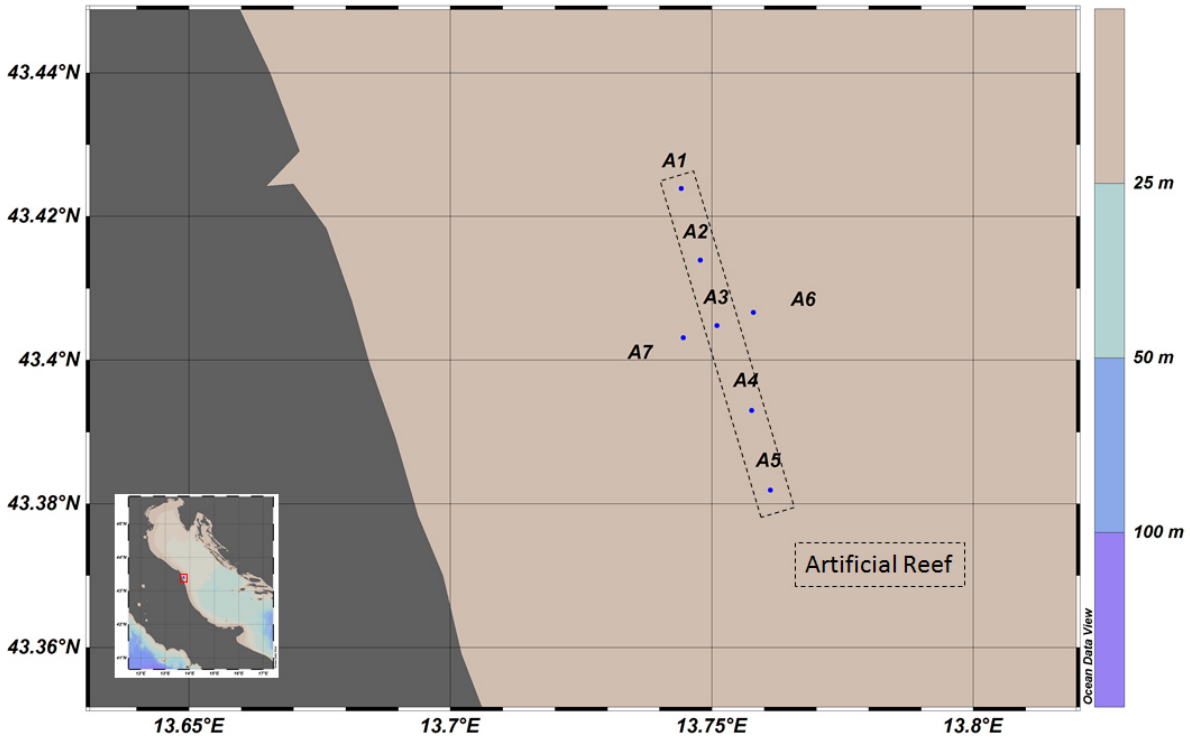

Figure 3.11 - Location of the 7 stations located within the Porto Recanati - Porto Potenza Picena AR.

Temperature and salinity profiles were measured at each station with a SeaBird Electronics SBE 19-plus CTD (Conductivity Temperature Depth; Figure 3.12), while turbidity, fluorescence and dissolved oxygen were measured by CTD sensors. Seawater samples were collected at the surface and close to the bottom using a Niskin bottle (Figure 3.12) that had previously been rinsed, to avoid contamination. Samples for nutrient analysis (Nitrite, Nitrate, Ammonium, Orthophosphate and Orthosilicate) were filtered (GF/F Whatman, nominal pore size 0.7 µm) and stored at -22 °C in polyethylene vials.

Figure 3.12 - CTD SBE19 plus (left) and Niskin bottle (right).

3.1.2. Data Analysis

Regarding the quality assurance of the buoy data, all the sensors have been calibrated by the manufacturer which guarantees the stability of the sensors for at least 2 years before carrying out a new calibration. An antifouling system allows the attenuation of the typical drift of the oceanographic sensors over time.

Only the turbidity sensor (Annex III) required a calibration which was carried out in the CNR laboratory (Figure 3.13). The polynomial coefficients were obtained by measuring the voltage, having a range from 0 to 5 Volts, of 3 different concentrations of formazin. These coefficients have been applied to the raw data of the sensor. For all the other parameters no transformations from raw data into engineering units have been necessary.

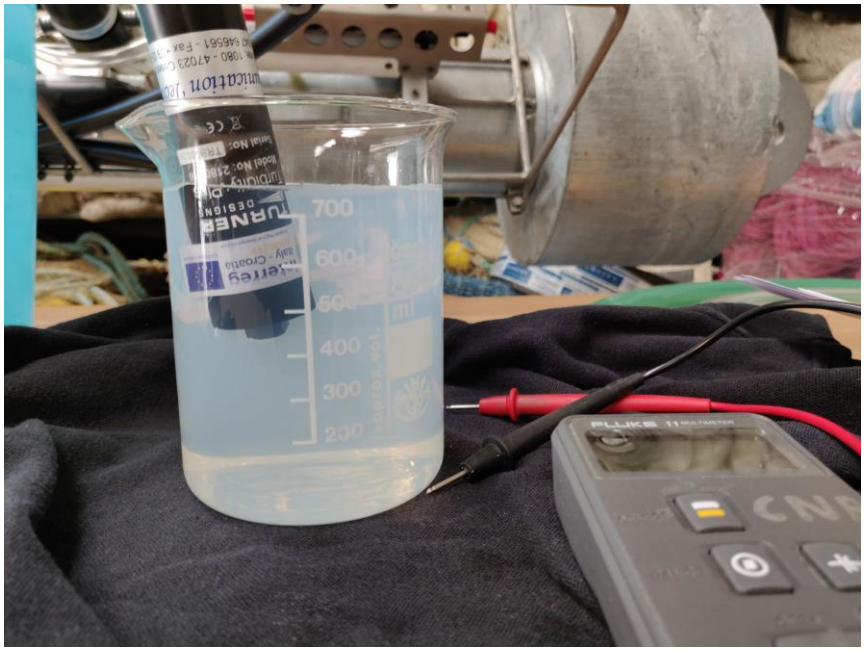

Figure 3.13 - Calibration of turbidity sensor at CNR laboratory.

The datalogger installed on-board communicates with sensors at a variable rate according to the type of measurement. Raw data are recorded in the local storage and every 20 minutes the data logger processes them to create a single record.

The meteo-oceanographic data, excluding the currentometric data, have undergone a QC according to the methodologies indicated in the Quality Control Standards for SEADATANET (https://www.seadatanet.org/Standards/Data-Quality-Control). In particular, in addition to checking the date and time (the geographic coordinates associated with the data are considered fixed for the entire dataset), remaining outliers (spikes, out of scale data, freezing data, etc) were detected and interpolations calculated only when there was only one over-range value. Each numerical value was associated with quality flags (Seadatanet L20, https://vocab.seadatanet.org/v_bodc_vocab_v2/search.asp?lib=L20) in order to not modify the observed raw data points. No media or transformation was applied on the data.

With regard to the data collected during the oceanographic campaigns, the 4 Hz CTD data were processed according to UNESCO (1988) standards, and pressure was averaged to 0.5 db intervals. Vertical profiles of temperature, salinity, fluorescence, turbidity and oxygen were mapped using the software ODV 5.4.0. Nutrients – ammonium-NH_4, nitrite-NO_2, nitrate-NO_3, orthophosphate-PO_4 and orthosilicate-SiO_4 underwent colorimetric analysis (Parsons *et al.*, 1985). Absorbances were measured with a BRAN+LUEBBE QUAATRO AutoAnalyzer (Fig. 3.14).

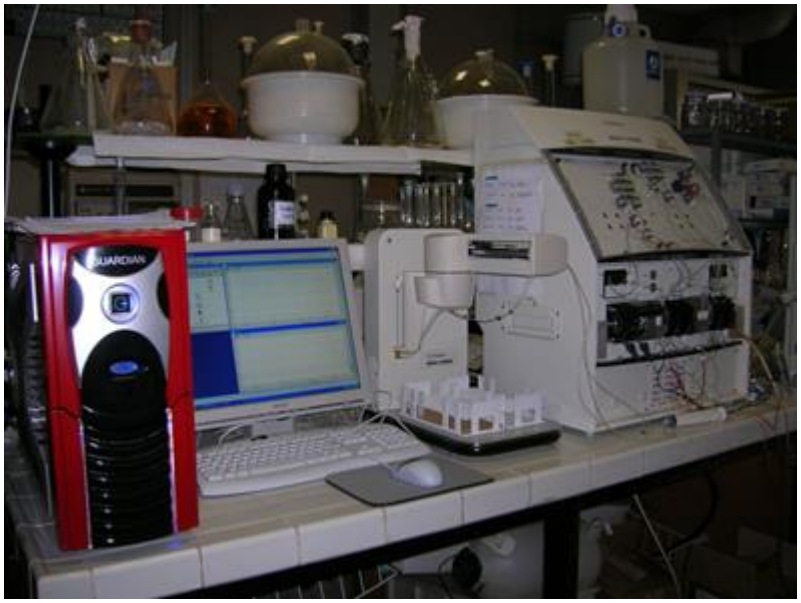

Figure 3.14 - Autoanalyzer QUAATRO - BRAN+LUEBBE.

3.3. Benthic community settled on the artificial reef

3.3.1. Data collection

Based on the outputs of the preliminary MBES survey which showed how most concrete poles had collapsed, the investigations aimed to describe the benthic colonization were focussed on the concrete pyramids. The following factors were taken into consideration in the designing of the sampling strategy:

1. North-Sud gradient, consisting of three levels corresponding to the three sampling sub-areas located at the northern-side (Area A), central-side (Area B) and southern-side (Area C);
2. slope, including two levels: O “horizontal face” and V “vertical Face”;
3. depth with two levels: B “bottom block” and V “upper block” (Figure 3.15).

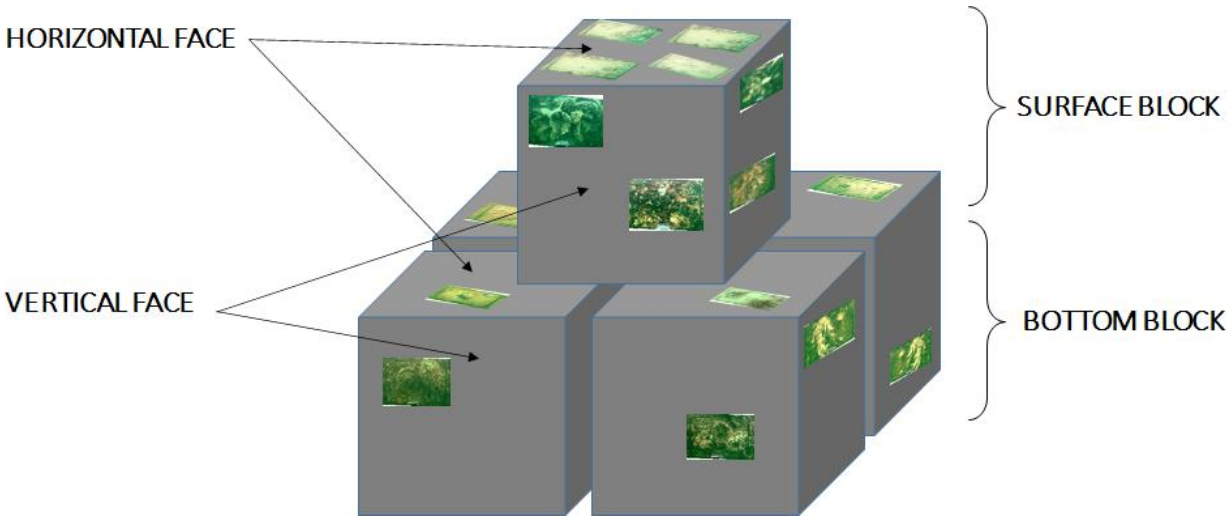

Figure 3.15 - Scheme of photo sampling with the factors taken into account.

In order to obtain sufficient data to characterize the benthic community settled on the structures and evaluate eventual annual variations, differently from what initially proposed we considered it more appropriate to carry out a three-year sampling and collect 4 replicates by each level of factors for a total of 48 photos/year.

Photographic sampling was preferred to scraping sampling as it is not disruptive. The samples were collected during June and July of each year from 2019 to 2021 by scuba divers. At each station, four replicates, each consisting of a picture of a frame 16cm x 24cm (total area = 384cm^2), were shot on the horizontal and vertical surfaces of base and upper blocks (Figure 3.15). The photos were taken with a Nikon COOLPIX W300 digital camera provided with an aluminum frame and underwater speedlight Nikon SB-N10 (Figure 3.16).

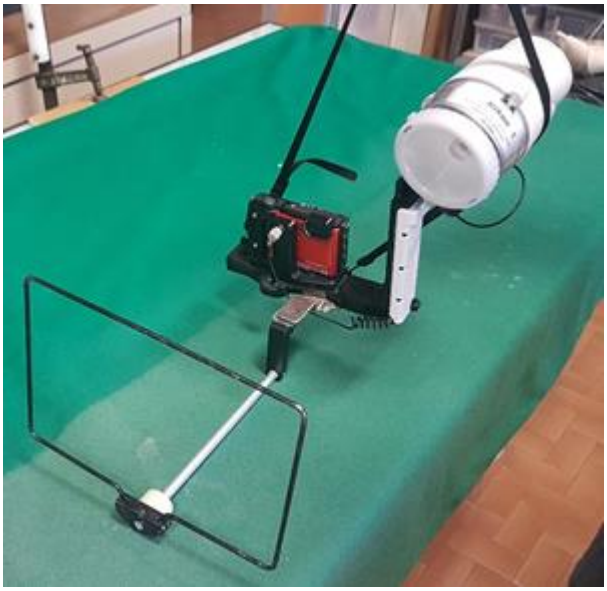

Figure 3.16 - Nikon COOLPIX W300 digital camera provided with the aluminum frame and underwater speedlight Nikon SB-N10.

3.3.2. Data Analysis

The photos were analyzed using the Image Analysis system PhotoQuad software (Trygonis and Sini, 2012) to investigate taxa composition and average coverage. Taxa coverage (i.e., the percentage surface area of the covered substrate as a projection of the specimens) was calculated using freehand regions tools in photoQuad (Figure 3.17). Since no living specimens were collected, the identification at species level was only possible for a few taxa.

Taxonomic and descriptive faunal manuals (Riedl, 1991; Nikiforos, 2005; Rinaldi, 2017; Luther and Fiedler, 2018) have been used to classify the taxa from the frame pictures (Figure 3.18). The nomenclature herein used follows the World Register of Marine Species (WoRMS Editorial Board 2020).

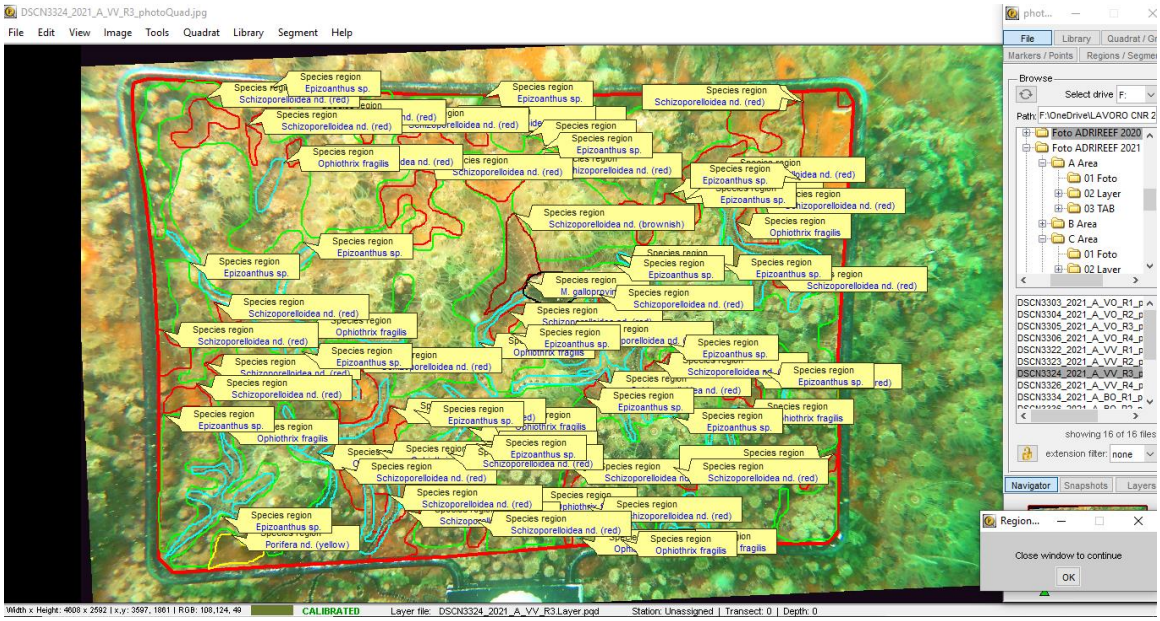

Figure 3.17 - PhotoQuad software screenshot with the taxa *assigned to the ROIs (Region of Interest).*

Figure 3.18 - Underwater frame picture.

The percentage of living habits and the percentage of each taxon found in the overall sampling period in the three areas were calculated to estimate the community composition and main living habits.

The average coverage percentage either by year and by area, depth and slope factor levels in the overall sampling period and in each year were calculated to provide an overview of the coverage degree in each considered factor level.

In order to estimate which levels had higher coverage values, JASP 0.14 software was used to draw the Flexplot (Fife, 2019; 2020) showing the relationship between the depth factor variables, i.e. bottom block (B) and upper block (V), in X axis and the coverage percentage of the independent variables, i.e. horizontal (O) and vertical (V) slopes, in Y axis through graphical displays of data, plotting in the same graph the scatter-plots of the three areas by year.

JASP 0.14 software and Past 4 - the Past of the Future (Hammer *et al.*, 2001) were used to perform the inferential statistical analysis aimed to verify the statistical significance of the differences observed among the coverage percentage of the investigated factors and to investigate more in depth the composition of the benthic population settled on the artificial substrates.

The Shapiro-Wilk test ($p < 0.05$) was performed to check the assumption of data normal distribution of the data of the coverage percentage and of the species composition, considering either the years and "area", "depth" and "slope" levels in the overall sampling period as well as the "slope" variables per each year, ,each "area" and "depth" factors (Shapiro and Wilk, 1965):

$$W = \frac{\left(\sum_{i=1}^{n} a_i x_{(i)}\right)^2}{\sum_{i=1}^{n} (x_i - \bar{x})^2}$$

Shapiro-Wilk test: x(1) ≤x(2) ≤ ⋯ ≤ x(n) are the ordered values of a sample x1, x2, ..., xn, and "a(i)" are tabulated coefficients.

The Student's t-test (*0.05 ≤ p < 0.01 = significant; p ≤ 0.01 = highly significant*) was used to highlight eventual dissimilarities between the variables per each year and per "area", "depth" and "slope" factors (Blair *et al.*, 1980):

$$t = \frac{Z}{s} = \frac{\bar{X} - \mu}{\widehat{\sigma}/\sqrt{n}}$$

Student's t-test: X is the sample mean from a sample X1, X2, …, Xn, of size n, s is the standard error of the mean, $\widehat{\sigma}$ is the estimate of the standard deviation of the population, and μ is the population mean).

When the data did not show a normal distribution (either transformed or not), the non-parametric statistical test, Wilcoxon signed-rank test (0.05 ≤ p < 0.01 = significant; p ≤ 0.01 = highly significant; Wilcoxon, 1945),

has been used to compare all the levels in order to assess dissimilarities between the average ranks of their population:

$$W = \sum_{i=1}^{N} \varphi(X_i) R(|X_i|)$$

Wilcoxon signed-rank test: where $\varphi(X_i) = 1$ *if X i >0 and 0 otherwise, and* $R(|X_i|)$ *is the rank of* $|X_i|$ *among* $|X_1|, \ldots, |X_N|$

Finally, the SIMPER (sample discrimination) analysis was performed to calculate, from the Bray-Curtis dissimilarity matrix, the contribution of each species (%) to the dissimilarity between the group variables showing dissimilarity, and to display the contribution of each species in each variable.

3.4. Mussel population

3.4.1. Data collection

3.4.1.1 Population structure

The investigation aimed to describe the structure and distribution of the mussel (*Mytilus galloprovincialis*) population settled on the artificial substrates of the AR. The factors taken into consideration in the sampling strategy were:

North-South gradient, consisting of three level corresponding to the three sampling sub-areas located at the northern, central and southern parts of the reef;

seafloor elevation, which includes <2m and >2m from the bottom;

structure shape, considering two levels: pyramids and poles.

In order to describe the patterns of biomass and density distribution of mussels for implementing a sustainable harvesting strategy, we tried to develop a non-invasive methodology consisting of the underwater photogrammetry associated with scraping samplings for photogrammetry validation. This methodology is widespread in tropical seas for morphometric measurement of coral reef (Neyer et al., 2018; Rossi et al., 2020). The number of samples was one for each factor (12 samples) to be collected for 2 years. However, due to the frequent poor visibility, typical of the central-western Adriatic Sea, after several attempts we were not able to obtain a sufficient photographic set of suitable quality for processing. For this reason, in June 2021, we decided to only proceed with the scraping sampling. During this survey, samples were taken by scuba divers using two different frames: a 40x40 frame for pyramids and a 30x40 specific curved frame for the poles (Figure 3.19. The adopted sampling strategy was the same described above.

Figure 3.19 - Photo of the frames used for the scraping sampling: on the left a regular frame 40x40 utilized on the pyramids; on the right the curved frame 30x40 used on the poles.

The samples of *M. galloprovincialis* taken by scraping were "cleaned" removing the epiphytes and weighed (total weight) directly on the boat.

3.4.1.2 Bioaccumulation of contaminants and pathogens

Three pools of mussels for chemical (bioaccumulation of contaminants), toxicological (levels of toxins) and microbiological (pathogens) analysis were collected in spring of 2020 and 2021 from the vertical walls of the pyramids. The specimens for the chemical investigations were frozen, while those earmarked the other two typologies of analysis were stored at 4°C and analysed within 24 h from the harvesting.

3.4.2. Data analysis

3.4.2.1 Population structure

In the laboratory, the mussels were measured (Shell length) to the lower millimeter by means of a calliper. The average density (N. individuals / m^2) was calculated for each area, type of structure (pyramid and pole), and depth (<2m; > 2m).

The length data of the mussels were aggregated into 0.5cm length classes in order to estimate the *M. galloprovincialis* size-frequency distribution per each area, type of structure and depth level. The size-frequency distributions were obtained through Past 4 - the Past of the Future (Hammer *et al.*, 2001).

Differences in mean-sizes per each area, type of structure and depth level were analyzed using a 2-tailed t-test.

The biomass was calculated by weighting the alive mussels from samples collected through scraping; this weight, referred to the size of the frame used (40x40cm for the pyramids and 30x40cm for the poles), was then related to 1 m^2.

The estimation of overall commercial production (mussel TL≥50 mm) of the AR was computed starting from the current average sizes and densities of mussels on the pyramids and on the poles and considering the time necessary to reach the commercial size as well as an overall mortality as derived by previous studies (Giulini and Maffei, 1994).

3.4.2.2 Bioaccumulation of contaminants and harmful bacteria

The chemical contaminants, toxins and pathogenic microorganisms to be detected were selected based on the EC Regulations 466/01, 853/04, 854/04, 2073/05, 1881/06 and UE Regulation 1259/2011 which regulate the harvesting and market of molluscs basing on defined parameters.

The chemical and toxicological analyses were carried out by the analysis laboratory "LAV srl" of Rimini (Italy), whereas the microbiological ones were conducted by the personnel of CNR-IRBIM. The following substances and pathogens have been detected:

- Heavy metals (Mercury, Arsenic, Cadmium, Lead) (UNI EN 16174-2012 +UNI EN 16171-2016);
- PCBs (EPA 3545 A 2007 + EPA 8270 E 2018);
- PAHs (EPA 3545 A 2007 + EPA 8270 E 2018);
- ASP (Amnesic Shellfish Poison) (AESAN-EURLMB Domoic Acid vers. 1 2008);
- PSP (Paralytic Shellfish Poison) (AOAC 2005.06);
- Liposoluble toxins (Okadaic acid and total derivates, total Azaspiracids, total Pectenotoxins, total Yessotoxins) (AESAN-EURLMB Marine Biotoxins vers. 5 2015);
- Escherichia coli (ISO/TS 16649-3:2005);
- Intestinal Enterococci (ISO 6579:2002/Cor.1:2004).

3.5. Fish assemblage

The fish assemblage was monitored to evaluate the suitability of the AR for diving activities, recreational fishing and/or professional small-scale fishery. Data were collected through Underwater Visual Census (UVC), performed by scuba divers (SD) and by a Remote Operated Vehicle (ROV).

3.5.1. Data collection

Samplings were conducted on the three sub-areas described in Figure 2.9, and took place between July 2020 and June 2021. Five surveys were carried out by SDs and 5 using ROV for a total of 10 replicates (Figure 3.20). SDs samplings were conducted during summer and fall, while the ROV was used in those months when the climatic conditions were less favourable to divers. Due to Covid restrictions which limited the number of people onboard, only one sampling could be conducted in parallel by SD and ROV (May 2021), to collect data for comparing the two methodologies. An attempt to collect data in parallel was also done in June 2021, however the strong sea current observed in such sampling hindered the possibility of deploying the ROV.

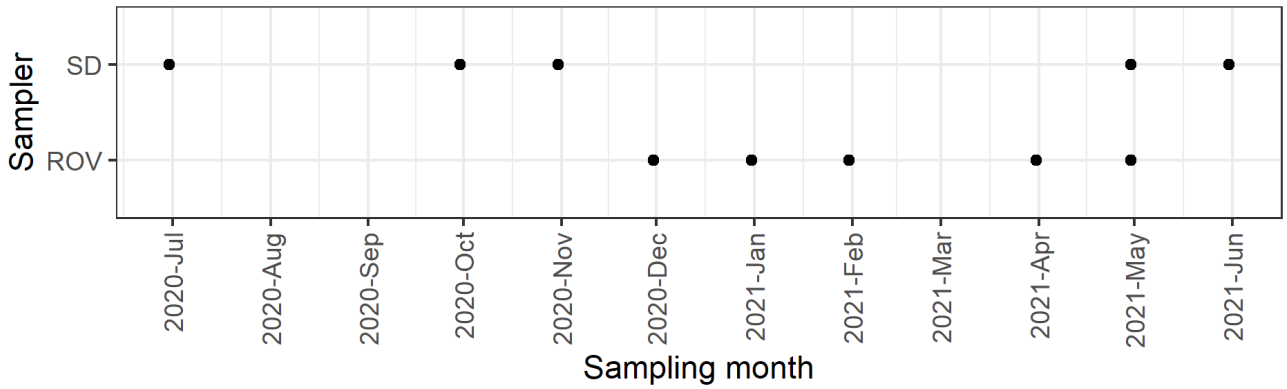

Figure 3.20 - *Sampling months (SD = scuba divers; ROV = remote operated vehicle).*

SDs team consisted of two scientific divers, trained on visual census techniques and identification of fish size within five years before the beginning of the project. Each sampling was conducted by both operators simultaneously, which collected data independently by means of a plastic dive-board (Figure 3.21). Data were reported on the diving log book and digitized in the CNR databases. When possible, the monthly samplings in the 3 sub-areas (area A, B and C) were conducted on the same day in order to have the same sea conditions.

ROV consists of a BlueROV 2 Heavy (Figures 3.22 and 3.23), a heavy duty self-powered ROV with 4 hours of autonomy and 8 thrusters (4 vertical and 4 horizontal) which are capable of delivering approximately 5kg thrust each. For the survey both the standard camera (high-definition camera with a field of view in the water of 110 degrees, a light sensitivity of 0.01 lux) and 2 GOPRO HERO 8 cameras (high-performance cameras that allow to shoot videos until 5.6K and field of view until 170°) mounted in a stereo configuration were used to capture the videos. The light compartment included 6 adjustable LED projectors with a power of 1500 lumens each and a light beam angle of 135°.

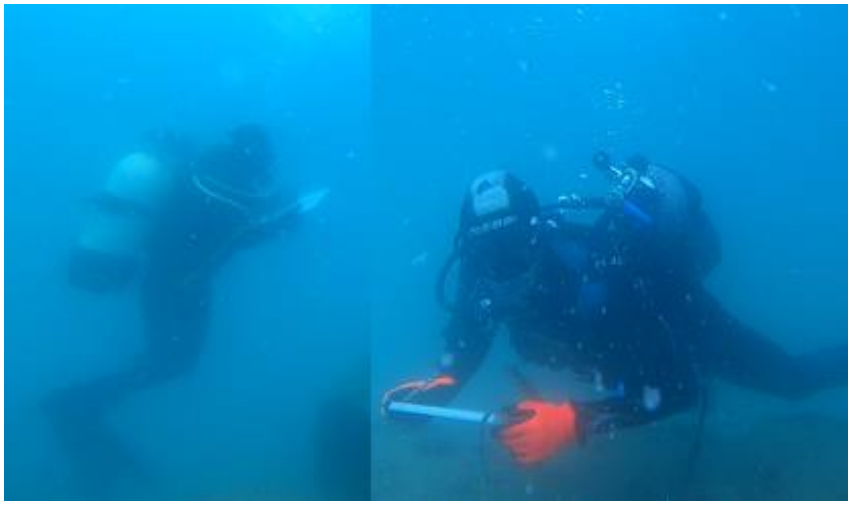

Figure 3.21 - Scuba divers during visual census.

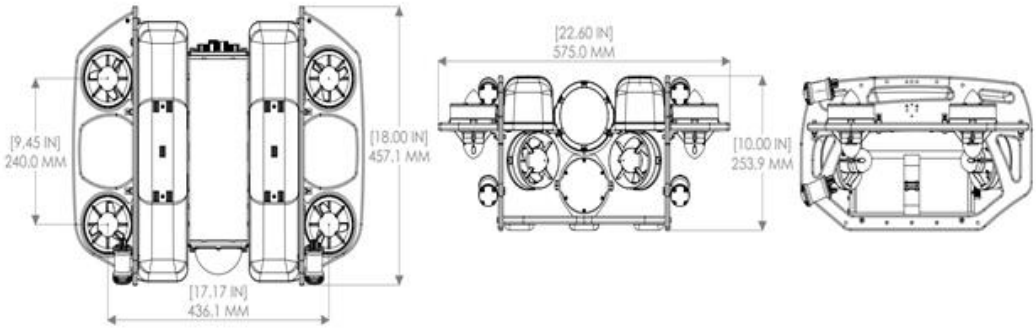

Figure 3.22 - BlueROV 2 Heavy technical scheme.

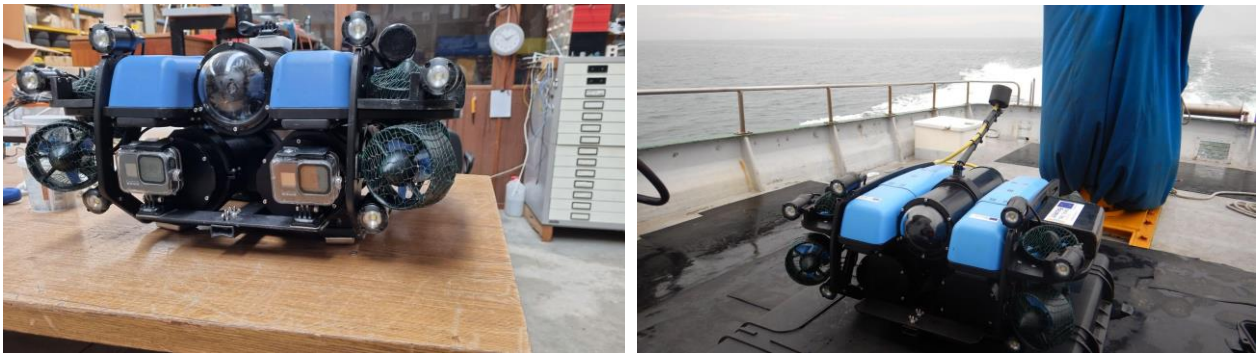

Figure 3.23 - Photos of the BlueROV 2 Heavy.

SD and ROV samples were collected according to the same sampling strategy, based on a systematic sampling design. On each of the investigated areas were *a priori* identified fixed paths, constituted by two pyramids, two poles and three transect lines connecting the structures (Figure 2.9). Lanes were laid along the selected transect lines, to facilitate the deployment of samplings. The sampling strategy was a mixture of strip transect, used to sample the line transects (Bortone and Kimmel, 1991), and mobile point count (Rilov and Benayahu, 2000), adopted to sample poles and pyramids. During the strip transects the samplers moved continuously at a constant speed along the path, recording the observations falling within a fixed distance from their position. During the strip transect, divers and ROV maintained a constant speed of near 17 meters per minute. Mobile point count is a relatively new technique, specifically designed for artificial structures, where the observers first record the most conspicuous and visible fish within a fixed area or volume, then approach the structure to closely examine for cryptic species, including an inspection of holes and crevices. This methodology was particularly suited for the investigated artificial reef, because of its structures providing many shelters for fish. Mobile counting lasted on average three minutes for poles and six minutes for pyramids. Observations were recorded only when falling within a radius of 1.5m from the investigated structure. The rationale of the 1.5 m radius was driven by the ROV angle of view.

The strengths and weaknesses of the two techniques may be derived from the literature and diving experience. Regarding SDs, there are constraints linked to environmental factors (Water depth and temperature, water transparency, currents) that may affect diving operations, and others related to the limited bottom time that may affect data collection quality. In particular, the time at the observer's disposal is generally limited and collected data cannot be revised, potentially affecting the identification of species (Andaloro *et al*., 2011). ROV may not be influenced by temperature and depth, while it may be strongly limited by currents and water turbidity. Video recorded may be revised, thus improving the possibility of species identification, however, resolution and field of vision of the camera are lower than the human eye, potentially leading to double-counting of the same individuals. In addition, standard videos do not allow for a correct estimation of the distance between the camera and the target, making it impossible to infer fish size.

To overcome this problem, in the original planning of the ROV sampling, it was considered to use a depth camera to be able to infer fish size. A camera depth module was created with the aim of interfacing the depth camera to the ROV Bluerobotics as well as to be used by divers (Figure 3.24). The Intel D435i commercial depth camera (https://www.intelrealsense.com/depth-camera-d435i/) was housed within a pair of watertight cylinders and equipped with battery, voltage regulator, control card (Jetson Nano) for data backup with its own solid-state drive (SSD), wifi dongle for remote control and setup. The drivers for the management of the camera and the software made available free of charge by Intel for the calibration and setup of the depth camera parameters were installed. The system had the purpose of assisting the acquisitions through the ROV and allowing the automatic classification of "fish" based on their length. The system was calibrated in the air and tested at sea; however, due to COVID pandemic restrictions, it was not possible to finalize the testing phase at sea in time to use the equipment for the data collection. The delayed

implementation of the depth camera was thus overcome with the use of the 2 GOPRO HERO 8 cameras mounted on the ROV in a stereo configuration (Figure 3.23).

Figure 3.24 - Camera depth module.

At the same time, a software prototype to analyze, recognize and classify the images produced by both mono and stereo underwater image acquisition systems has been developed. The final objective was to optimize the identification process of the fish species and completely automate the UVC saving man work either at sea and in the laboratory.

The methodology used is Deep Learning, a part of a broader family of machine learning methods based on artificial neural networks. A module allows the analysis of images in order to automatically identify the presence of organisms of interest, based on a set of images (training set) labeled by an expert biologist (Figure 3.25). Using images and videos available in the CNR archives, a list of a few species which can occur at the AR has been compiled. Only those species for which we had at least 100 sharp images have been selected (Table 3.I).

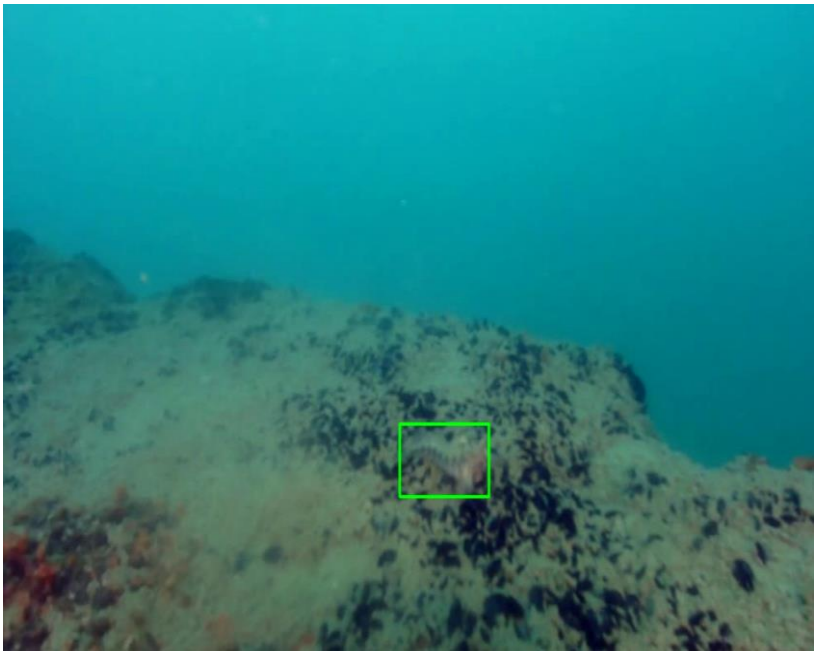

Figure 3.25 - An example of the tagging operation necessary to define a training set of images tagged by an expert.

Table 3.I - List of the fish species selected to train the recognition software.

Boops Boops	*Parablennius tentacularis*
Diplodus annularis	*Sciaena umbra*
Diplodus vulgaris	*Scorpaena* spp.
Oblada melanura	*Seriola dumerili*
Parablennius gattorugine	*Serranus cabrilla*
Parablennius rouxi	*Serranus hepatus*

The software made it possible to tag individual targets by generating xml mappings, separated by dedicated disk folders and usable also on other networks.

On the basis of these images, once the defined regions of interest (RoI) are known, for example corresponding to fish, the recognition module will automatically acquire the ability to perform the same operation on new images of the same typology. An example of automatic recognition is reported in Figure 3.26.

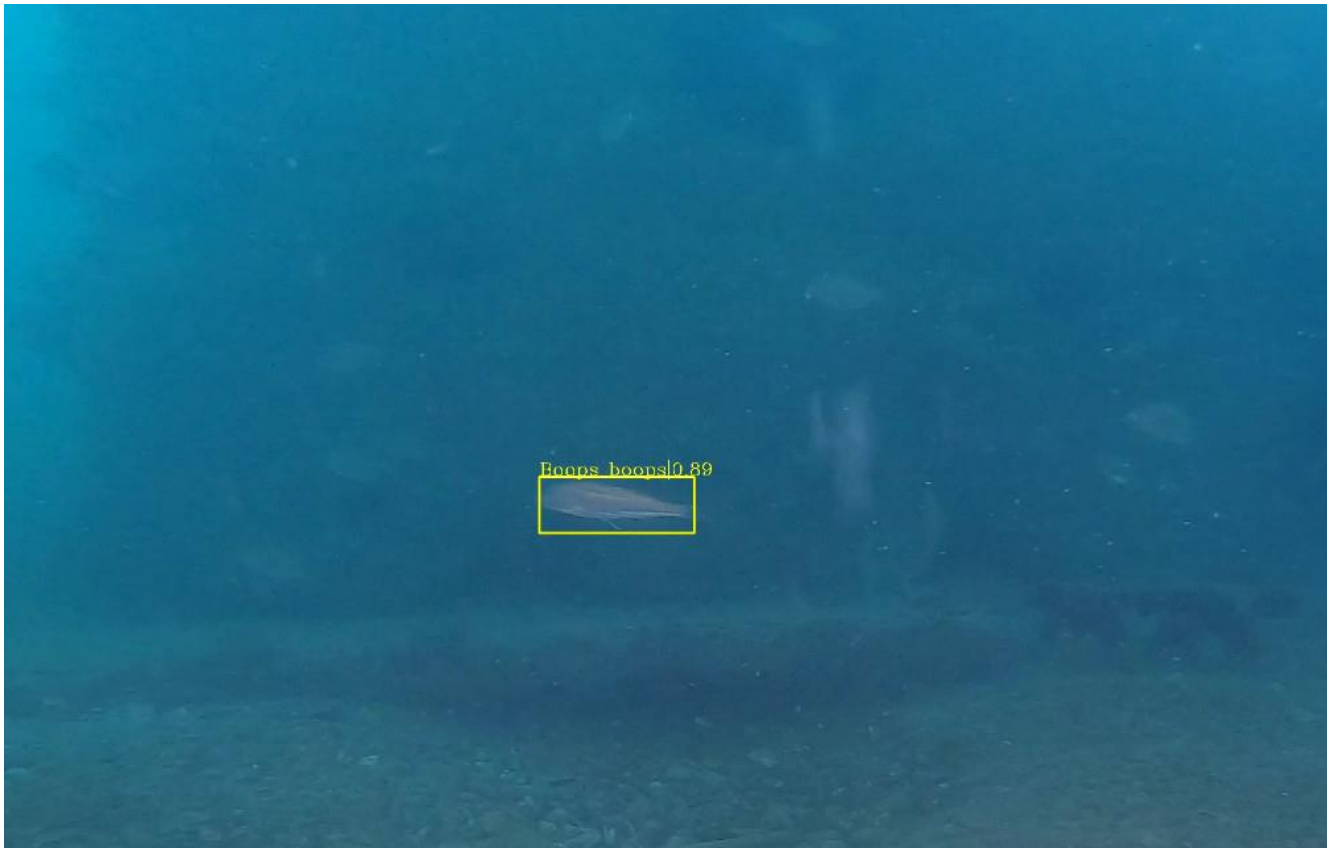

Figure 3.26 - Example of automatic recognition of a fish species by using deep learning. Above the yellow box is reported the name of the species, while the number indicates the probability [%] of recognition success.

Another software module performs the temporal integration in order to establish the count of the number of organisms detected in a video recording. The module carries out a tracking process of the detected organisms in order to avoid, however possible, the multiple counting of the same individuals, if they remain in the field of view of the camera for several consecutive frames. Figure 3.27 shows an example of classification and counting generated by the processing of a video produced by ROV.

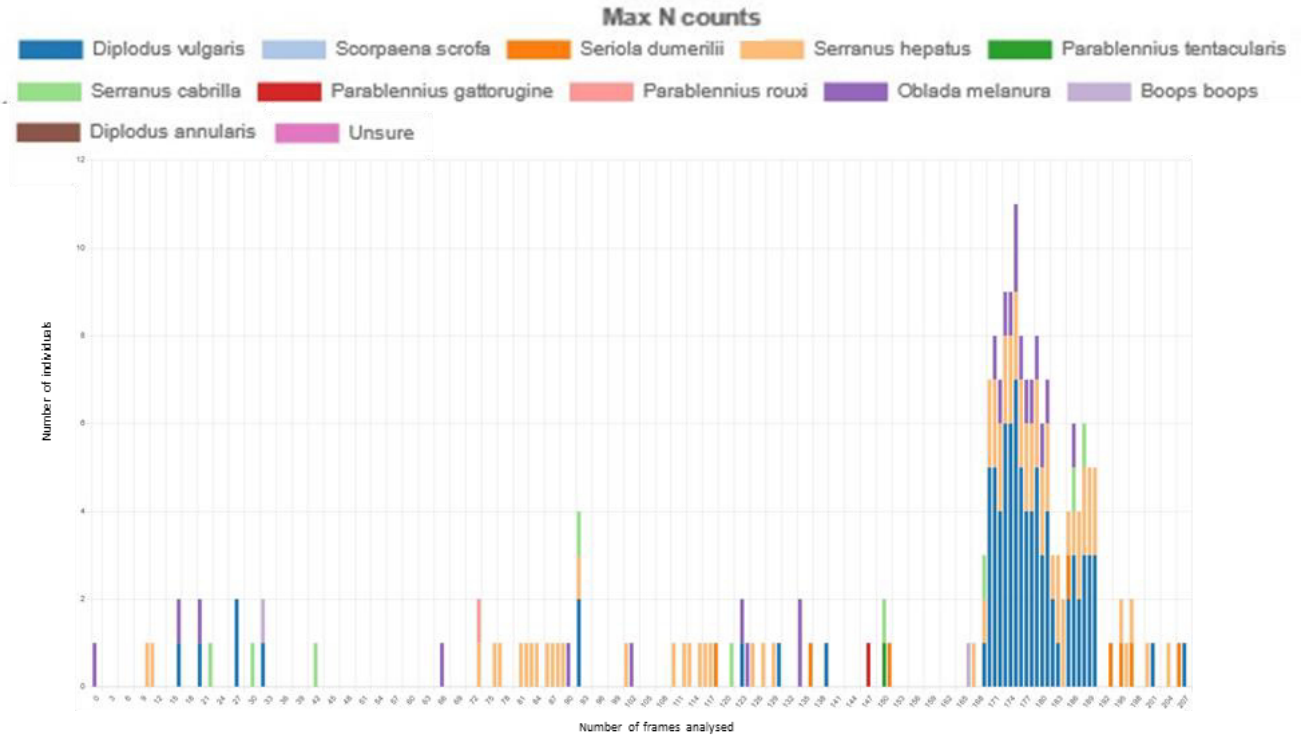

Figure 3.27 - Number of specimens classified by species generated by the processing of a video ROV through the use of deep learning methodologies. y axis: number of individuals; x axis: n. of the frame analysed.

The final result [%] of the video processing is shown in Figure 3.28, where *Precision [%]* is defined as the number of true positives over the number of true positives plus the number of false positives and *Recall* [%] is defined as the number of true positives over the number of true positives plus the number of false negatives.

At present, the software does not resolve about 20% of cases (using a threshold of 0.770), which would be in line with the percentages reached by recognition softwares reported in the literature using cameras in motion and with dynamic and complex background (81.44% as reported in Salman *et al*., 2020). However, given that our final goal was to implement a fully automated visual census through video analysis, the prototype is still under development to try to get close to 90-95%% of resolved cases, similarly to the percentages which are achieved by processing videos generated by fixed cameras positioned near reefs or Fishing Aggregate Devices (FADs) and in conditions of high water transparency (Konovalov *et al*., 2019). In order to achieve such a result, we are applying a methodology which allows a further refinement of the results by tagging all unsolved cases. The result of this analysis will enrich the neural network again, thus generating a virtuous process that will lead to the predetermined results.

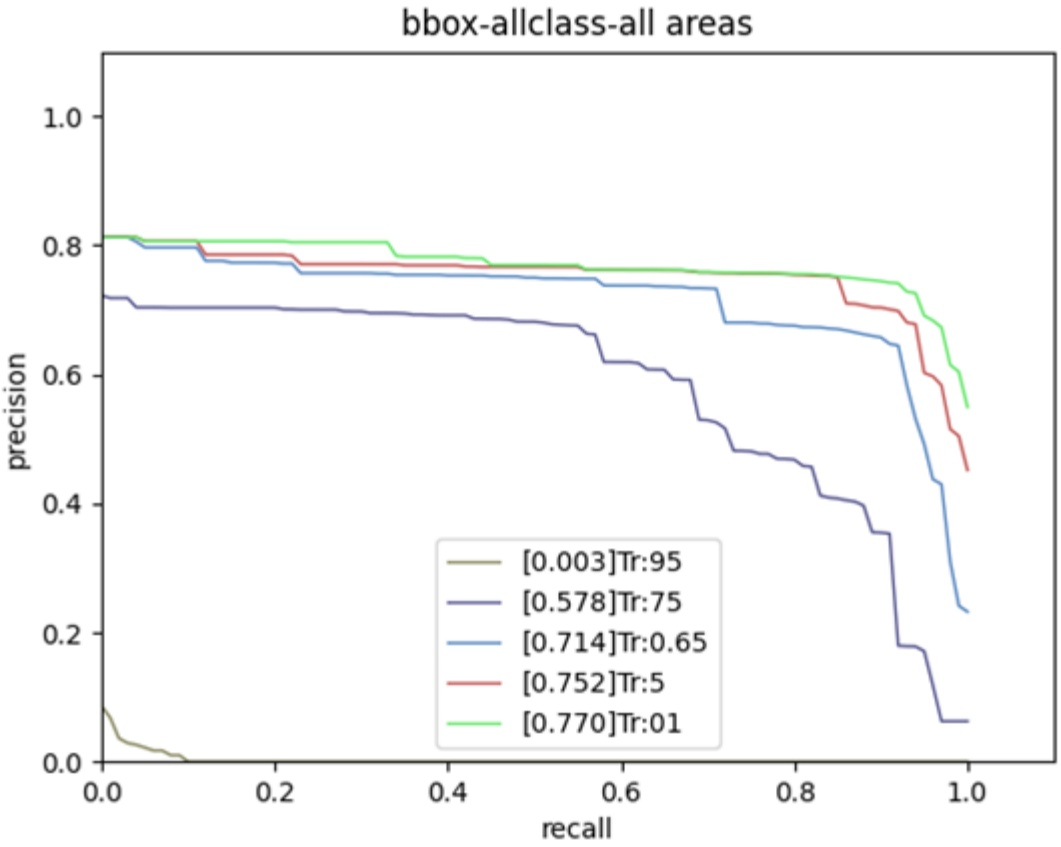

Figure 3.28 - Precision-recall curve shows the tradeoff between precision and recall for different thresholds.The best result is achieved using a threshold of 0.77.

With regards to the classification of the recognized species with respect to their size from moving underwater images generated by the depth camera (Figure 3.24) and GOPRO cameras in stereo setup (Figure 3.23) installed on ROV, the prototype still shows a low accuracy, hence it was not possible to utilize the data for the analysis. Also in this case a further optimization is still in progress.

3.5.2. Data analysis

SDs collected data according to size and abundance categories, as shown in Table 3.II.

Table 3.II - Fish assemblage categories for size and abundance.

Class	Minimum size (TL; cm)	Maximum size (TL; cm)	Minimum abundance (N. specimens)	Maximum abundance (N. specimens)
A	1	5	1	1
B	6	10	2	5
C	11	20	6	10
D	21	30	11	20
E	31	40	21	50
F	41	50	51	100
G	51	100	101	200

Since the recognition software was not yet completely developed, the footage recorded by ROV were manually inspected to collect data within the same abundance categories. Post-analysis of the recorded videos was carried out on a 24“screen, using standard software that enables pausing, slow-motion viewing and zooming of the images. Discrete observations were derived from categorical data by the mean of bootstrap resampling, based on the following steps:

1. size (only for SD) and abundance classes were transformed into continuous normal distributions, built on the *rnorm* function. The *rnorm* function requires as parameters the mean and the standard error of the distribution that the user needs to simulate. For this purpose, the mean was the mean of the reference class and the standard error was calculated on the series comprising the minimum value and the maximum value of the class, with unitary increments.
2. Punctual observations for abundance and size (only for SD) were randomly drawn from the normal distributions.
3. Size data were transformed into weight data (only for SD) by applying the length-weight relationship W (g)=a*L^b , with a and b parameters derived from FishBase (Froese and Pauly, 2019).
4. Weight data were multiplied by the sampled abundance (only for SD).
5. Steps 2-4 were bootstrapped 999 times to permit uncertainty quantification.

Abundance and biomass data were standardized by the volume of water inspected, calculated for each structure by reworking the methodology already proposed by Bombace *et al.* (1995) (Figure 3.29). In particular, the volume of the transect line connecting the structure was taken to be a cylinder, with a radius of 1.5m and a length equal to the length of the transect minus 3 meters, because the edges were included within the volume of the structure. The pyramid volume was calculated as follows: first, were drawn circumferences of radius 1.5m at each corner of the blocks forming the pyramid, recording the intersections between circumferences. Then, two rectangular parallelepipeds were drawn, having a basis equal to the horizontal line joining the most distant point touched by the circumferences, and height equal to the line joining the intersections. The sampled volume was therefore equal to the sum of the volume of the parallelepipeds minus the bulk volume of the pyramid. The volume of the poles was calculated by summing a cylinder with radius 1.5m and height 1.5m (built on the top of the structure) and a hollow cylinder, having

the internal diameter equal to the pole diameter and the external diameter equal to the pole diameter plus 2 x 1.5m. The volume calculated is reported in Table 3.III.

The species list was aggregated in ecological categories (Bentonic, Nekto-Bentonic, Pelagic) following the categorisation provided in Bombace *et al.* (1994); such categorisation was used for the purpose of data exploration. Abundance data divided by volume inspected were aggregated by those categories, as well as by structure and month, and were plotted in different combinations to explore the fish assemblages encountered during the sampling period, providing useful information for divers. By the mean of these charts it will be possible to understand which species are frequently encountered or not, and which month may provide the better option for divers and/or fishers.

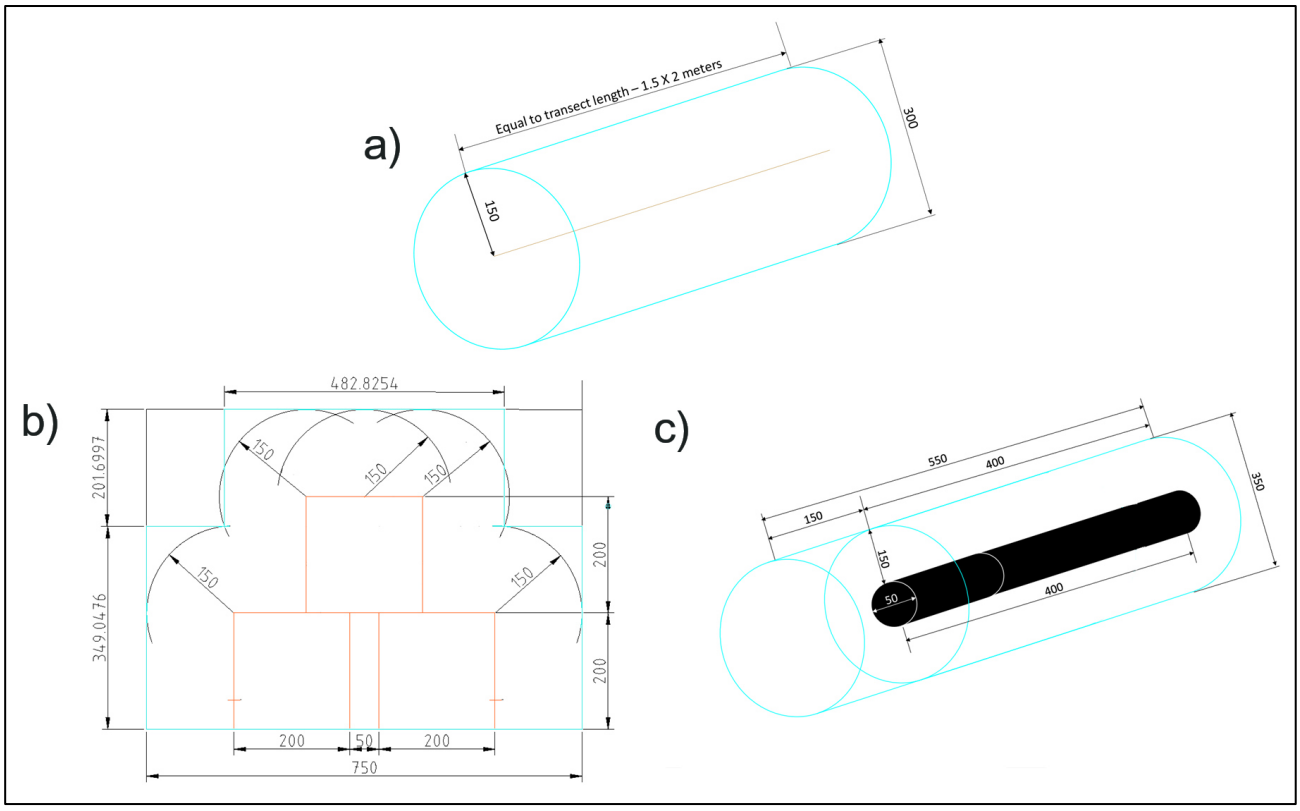

Figure 3.29 - Volume calculation. a: transect; b: pyramid; c: pole. Measures are in cm.

Table III - Structures details.

Structure	Total vol (m^3)	Structure vol (m^3)	Inspected vol (m^3)
Pyramids	243.4	40	203.4
Poles	52.9	3.1	49.7
Transect A1 (35 m)	247.3	0	247.3
Transect A2 (50 m)	353.3	0	353.3
Transect A3 (45 m)	317.9	0	317.9
Transect B1 (24 m)	169.6	0	169.6
Transect B2 (29 m)	204.9	0	204.9
Transect B3 (42 m)	296.7	0	296.7
Transect C1 (33 m)	233.1	0	233.1
Transect C2 (25 m)	176.6	0	176.6
Transect C3 (65 m)	459.2	0	459.2

A set of indicators aimed to fulfil the task objectives were also derived from ROV and SD data:

1. Species Richness (Sr): represents a measure of the variety of species based simply on a count of the number of species in a particular sample. This index informs on the number of different species that are expected on the reef and may be useful for diving activities.
2. Shannon Index (H): used to measure the diversity of the population balancing species richness with the relative abundances of the species. H was calculated as

$$Hsh = -\sum_{i=1}^{S} pi * \log pi$$

where: S is the number of species in the assemblage and the $_i$th species relative abundance is p_i.

3. Biomass (B): can provide information on the reef productivity, and can also inform the user on the expected quantity of fish observed on the artificial reef. B calculation relies on size data; therefore, it was calculated only for SD observations.
4. Species detection probability (SDP): is a measure used to quantify the probability that both observers would see all species along a paired transect (Bernard *et al.*, 2013) and was defined as

$$Dp = \frac{B}{O1 + O2 + R}$$

where: B is the number of species recorded by both observers, O1 is the number of species recorded only by observer 1 and O2 is the number of species recorded only from observer 2.

The first analysis was a comparison between data collected by ROV and SDs. This analysis may serve to understand if the indicators derived from the two sampling techniques may be merged, to obtain a longer

time series. Data to test for differences was collected during May 2021, when the observations were conducted in parallel. Sr, H and N indicators were fitted, first, into a three-way permutational univariate analysis of variance (permutational ANOVA) considering Area, Structure and Method as factors. This univariate analysis was used to detect significant differences between the mean values of indicators recorded by both methods. Indicators that were not affected by the method, and only for pyramid observations, were further evaluated with Generalized linear mixed models (GLMMs), where the sampling method was the fixed factor and the area was treated as a random term. Based on preliminary observation, there was a high number of zeros on transects and poles, so it was decided to conduct this comparison only for the pyramids. The choice of the model was driven by the distribution of the data, which were close to a gamma distribution with heteroscedasticity, and by our hypothesis to test just for differences between the methods, and not on the areas. GLMMs are particularly suited for this purpose because they combine the properties of two statistical frameworks that are widely used in ecology and evolution, linear mixed models that incorporate random effects (which is what we need to test our hypothesis), and generalized linear models (which handle non normal data by using link functions and exponential family) (Bolker *et al.*, 2009).

Based on the analysis result, it will be decided if possible to merge the data time-series. In the contrary case, data collected by the two methodologies will be analysed separately. We are interested to test for differences on the indices proposed in the section above due to three factors: areas, structure and season. In this case, since we were no longer dealing with random effects, the methodology was based on the analysis of variance. Data were tested for normality and heteroscedasticity to decide whether to use a parametric test or not.

In addition, species assemblages as collected by ROV and SDs were compared with multivariate statistical techniques using the functions provided in the R library “vegan” (Oksanen *et al.*, 2016). To evaluate the fish assemblages, a pair of community assemblage lists, one for ROV and one for SDs, were calculated for each structure inspected as the number of individuals by species divided by the volume of water inspected. Then, abundance data were transformed to log (x + 1) to reduce the influence of high values in the following analysis (Quinn and Keough, 2002). Transformed community assemblage data were used as input to calculate a matrix of compositional dissimilarities between samples based on Bray-Curtis distance, which is well suited to species abundance data (Quinn and Keough, 2002). Bray-Curtis Matrix obtained were used as input to conduct a set of multivariate analysis with different purposes:

1. Non-metric Multidimensional Scaling (NMDS), a robust unconstrained ordination method in community ecology (Minchin, 1987) suited to graphically represent relationships and differences between objects in multidimensional space.
2. Analysis of Similarities (ANOSIM), a hypothesis testing procedure based on the difference between the average of all the rank dissimilarities between objects between groups. ANOSIM aims to test if the average of the rank dissimilarities between all possible pairs of objects in different groups is the same as the average of the rank dissimilarities between pairs of objects in the same groups. This analysis was conducted twice to test both structure and species as grouping factors.

3. Similarity percentage (SIMPER), a procedure for determining which variables are contributing most to the dissimilarity between groups of objects. This analysis was conducted only on variables resulting in a significant effect in the ANOSIM analysis.

3.6. 3D reconstruction model

3.6.1. Data collection

As explained in the Chapter 3.4.1.1, it was not possible to use the underwater photogrammetry to estimate the biomass of mussels settled on the AR structures.

However, we decided to dedicate the last part of the project to experiment a new methodology for documenting the environment point by point and merging the entire area by means of a large acoustic map. Unfortunately, due to numerous factors including the Covid-19 pandemic, it was not possible to apply the digital monitoring to the whole AR. Within the above framework, the project team planned to survey a pyramid at various depths and to explore advanced methods and techniques of data acquisition through SD, compensating the visibility problems.

3.6.1.1 Camera Calibration

Camera calibration in multimedia photogrammetry has been a problem identified for almost 50 years (Mccurdy, 1944; Bass, 1973). The problem has no obvious solution, since the light beam refraction through the different media (water, glass, air) introduces a refraction error which is impossible to express as a function of the image plane coordinates alone (Murase, 2008). Therefore, the deviation due to refraction is close to that produced by radial distortion even if radial distortion and refraction are two physical phenomena of different nature. For this reason, the approach described by Kwon (Maas, 1995) has been adopted, consisting in the use of standard photogrammetric calibration software to perform the calibration of the set housing + digital camera step by step from air to water with a linear panel. This approach can indeed correct in a large part the refraction perturbation; however, it is strongly dependent on the optical characteristics of the water/glass interface of the housing. In order to minimize the refraction error due to this last interface, a housing with a hemispherical glass has been selected for the divers-operated camera. A custom calibration panel (Figure 3.30) and a software have been tuned for the adopted optical system.

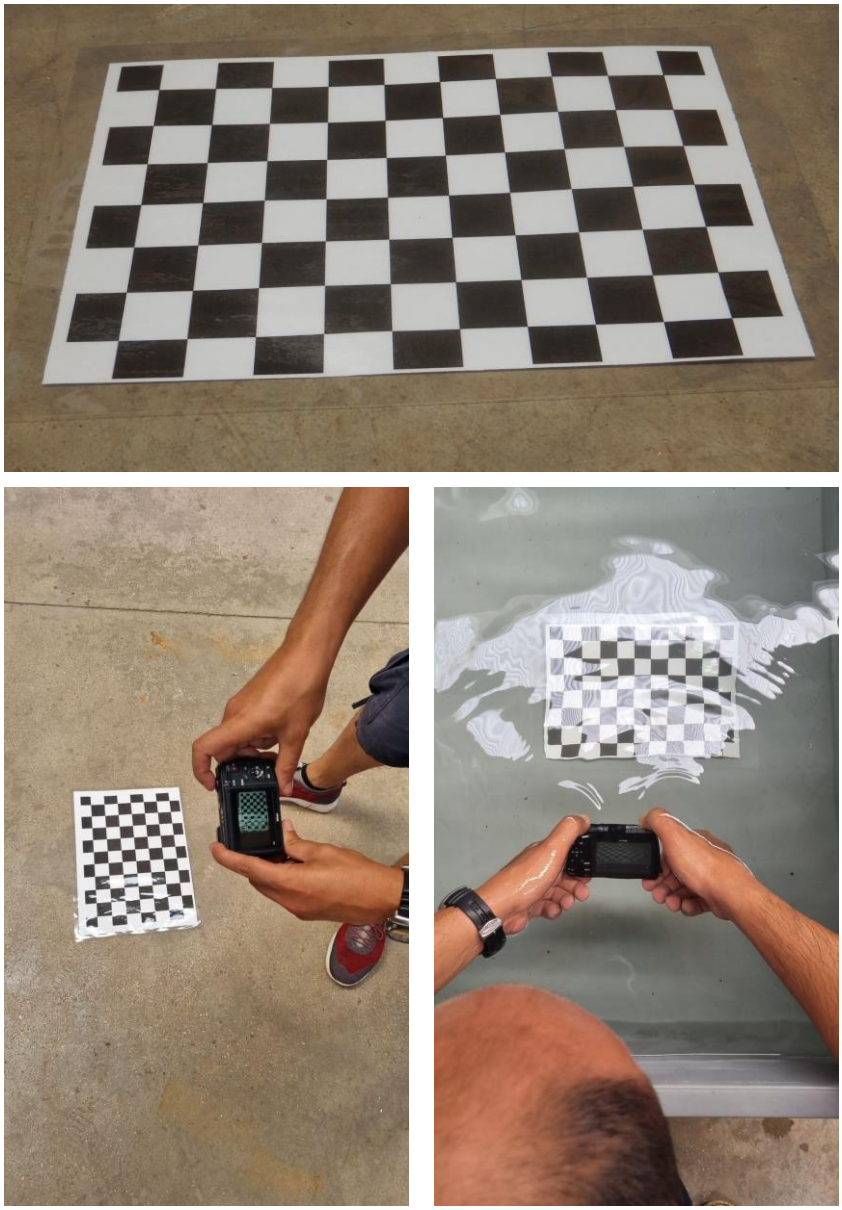

Figure 3.30 - Calibration panel and procedure in air and in water.

3.6.1.2 Environment preparation and data collection

The photogrammetric survey of the pyramid was planned to obtain a sequence of photographs over a linear strip, surface by surface of each pyramid block, with an appropriate forward overlap (60%) between two

subsequent photographs. Once a strip was completed, an adjacent strip was surveyed, with 20% lateral overlap with respect to the previous strip. The procedure, as well as the geometry, is very similar to the technique used in aerial photogrammetry; the main differences are the distance to the seabed and presence of the water. The bathymetric variation could also be in general an important difference, but not considering one side of the cube at a time, as the working area is flat. As reported, each image is not so focused due to the poor visibility, and very similar to the consecutive ones. To facilitate the algorithm, a white rope was added and the name of the file was considered by the algorithm as a movement guidance.

The working area (single cube face) was delimited by SDs, who also deployed 3 ropes (0.5m each) to define a grid for photograph guidance (Figure 3.31).

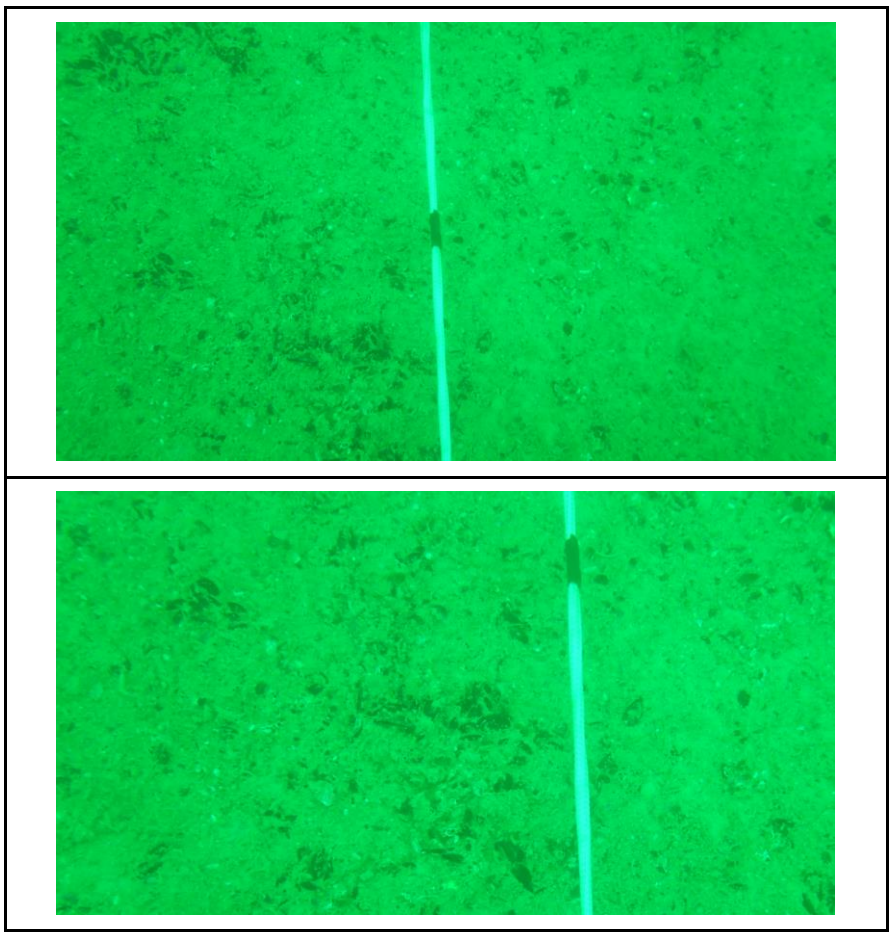

Figure 3.31 - Two consecutive photos with the white rope used as mathematical reference in the *reconstruction algorithm.*

In order to perform photogrammetric reconstruction a single cube, face by face, has been surveyed. Each face needed about 10 stripes from 50 photos considering faults. Each face survey required about 1 hour of underwater work.

3.6.2. Data analysis and cube reconstruction

A set of observations of homologous points on photographs were measured manually to orient all the photographs in a local reference system. Then we used the camera position given by navigation data estimated since the previewed movement was introduced in the process. In Figures 3.32 and 3.33 an example is given of the final result: a 3D model of the horizontal up face is obtained, over which oriented photographs are superimposed.

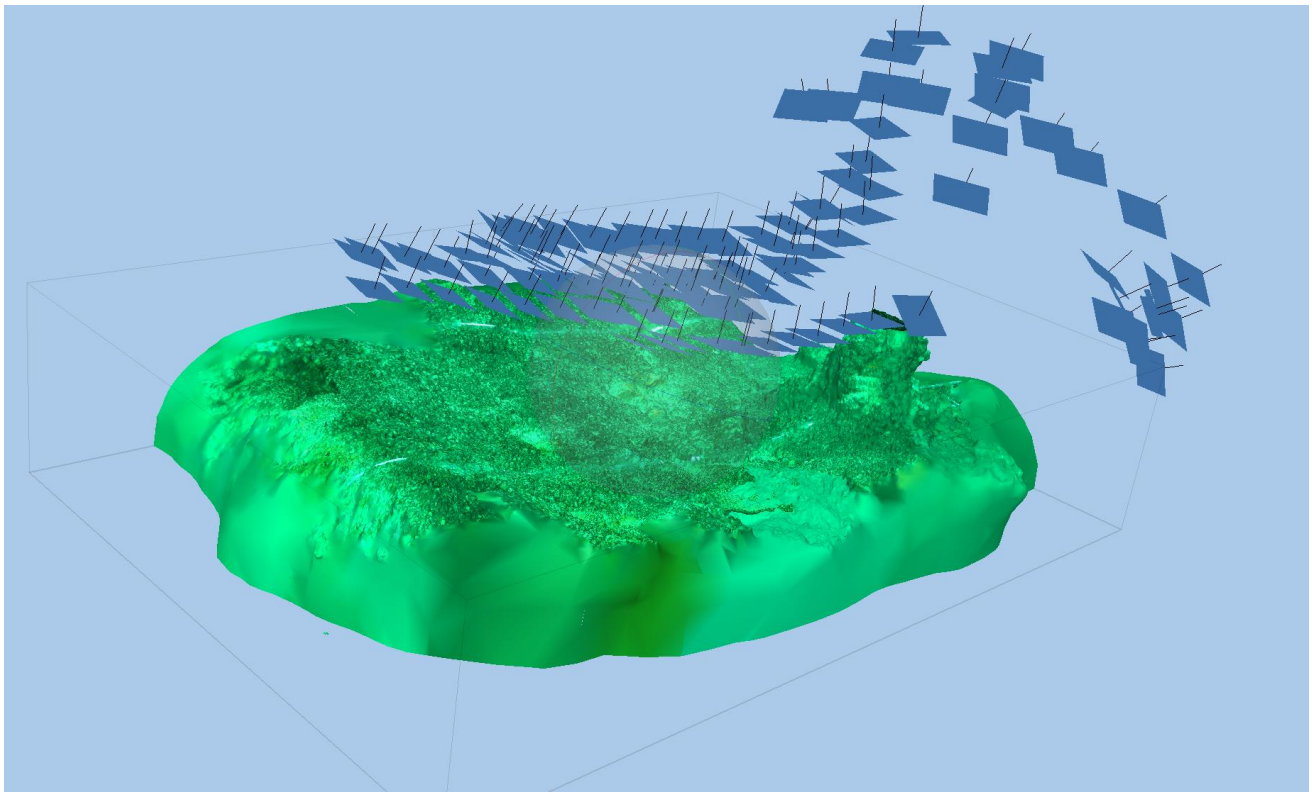

Figure 3.32 - The horizontal face of the up cube in the pyramid (see the 1:100 model in https://univpm-my.sharepoint.com/:f:/g/personal/p004291_staff_univpm_it/EiykKTyinZtNoi-1O5KjqsQBUC_EtZJ34kG1eDu61RXsmw?e=VYs7fw).

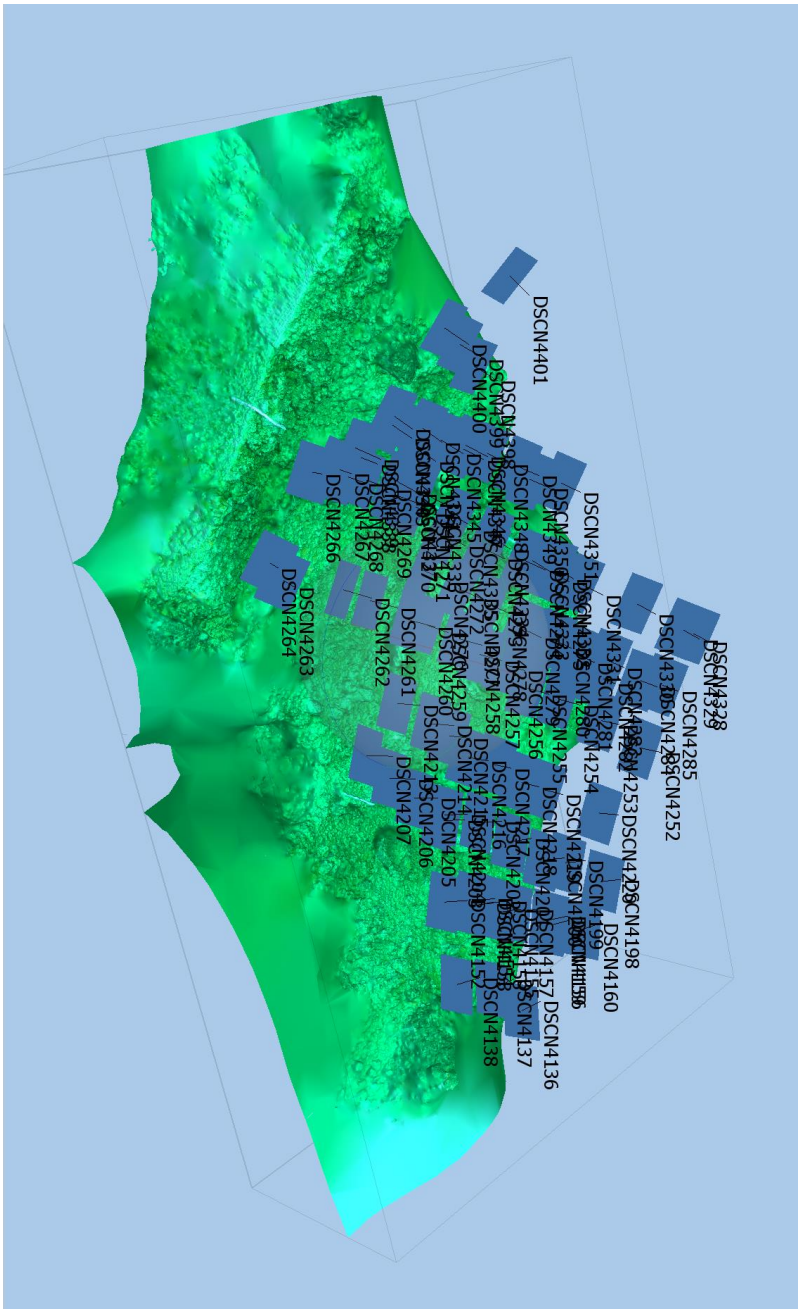

Figure 3.33 - The northern vertical face of the up cube in the pyramid (see the 1:2 model in https://univpm-my.sharepoint.com/:f:/g/personal/p004291_staff_univpm_it/EiykKTyinZtNoi-1O5KjqsQBUC_EtZJ34kG1eDu61RXsmw?e=VYs7fw).

4. RESULTS AND DISCUSSION

4.1. Speed and direction of water currents

The cyclonic circulation (anticlockwise) typical of the Adriatic basin is linked to the prevailing winds (Bora and Scirocco-Levante). In particular, the masses of water transported by the WAC (West Adriatic Current) move along the Italian side (Figure 4.1, red lines) from the North-West to the South-East, while on the Croatian side the masses of water transported by the EAC (East Adriatic Current) move towards the North-West (Artegiani *et al*., 1997a and 1997b). In the northern Adriatic, dense waters (cold and salty waters) can also form during the winter months, which slide to the bottom and constitute one of the engines of the thermohaline circulation of the Mediterranean, thus allowing its mixing (oxygenation, enrichment of organic substance, etc.) between surface and bottom waters (Figure 4.1, green lines).

Along the Marche coast there is therefore a coastal current, the WAC, mainly composed of cold and not very salty waters coming essentially from the Po river, which pushes the waters of the Adriatic towards the Ionian Sea.

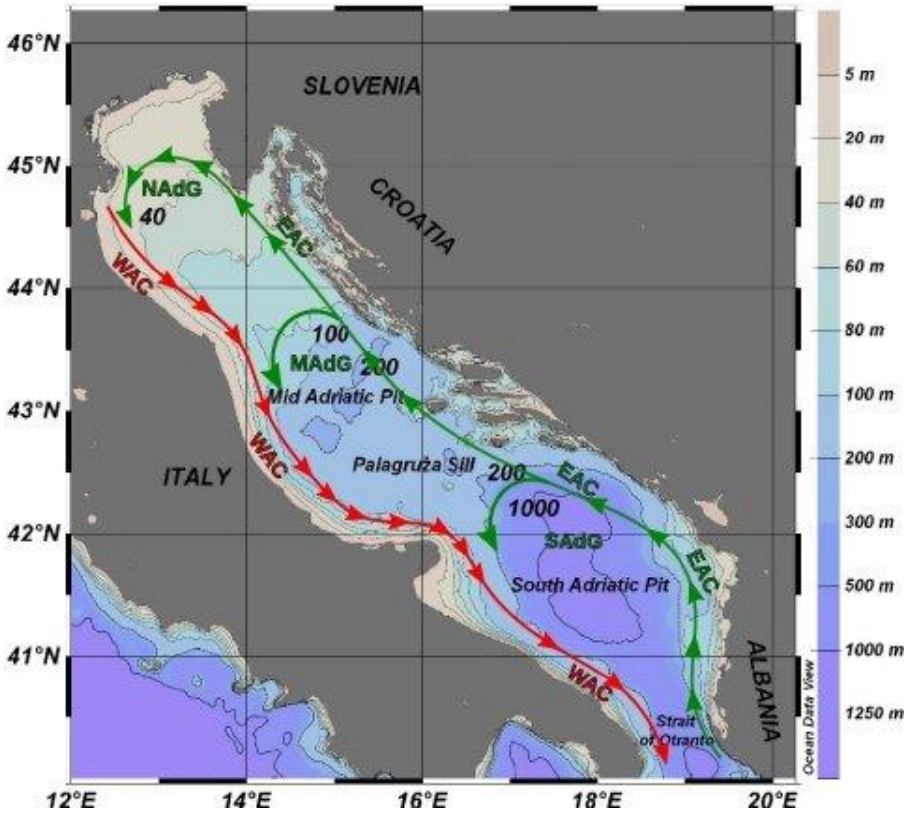

Figure 4.1 - Surface circulation model in the Adriatic sea. Picture from Lipizer *et al*.,2014.

The presence of the WAC is confirmed by the measurements of the ADCP currentmeter. In Figure 4.2 the XY components are shown in a scatter plot where the direction parallel to the coast of the current is evident, mainly oriented towards South-East with an inclination of about 135 North degrees. The graph also shows the presence of a current having opposite direction to the WAC (North-West). Such current is generated by the balancing of the sea level and by local anticyclonic gyres generated by the wider passage of the WAC. Indeed, the Conero Promontory tends to push the WAC towards offshore and this generates an inshore current with an opposite direction.

data from July, 2 2020 to October, 22 2020	data from May, 26 2021 to July, 25 2021
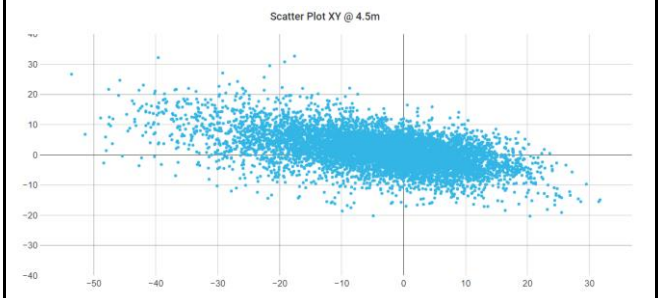	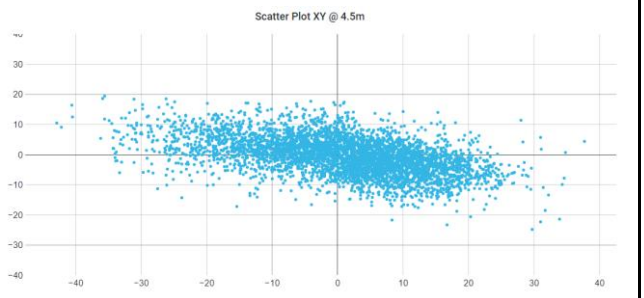
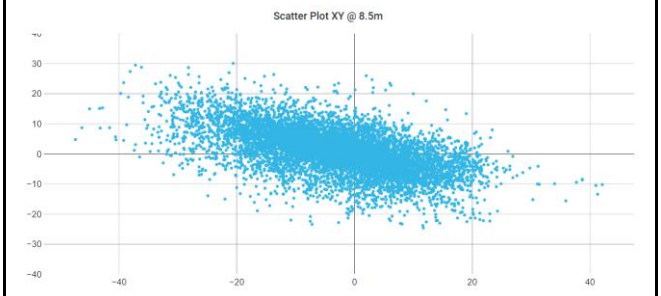	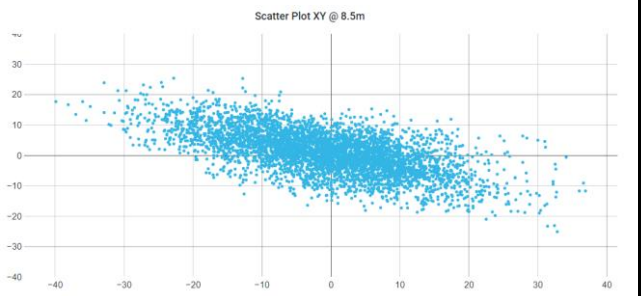
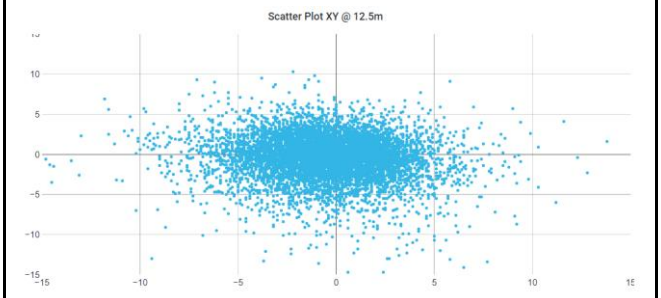	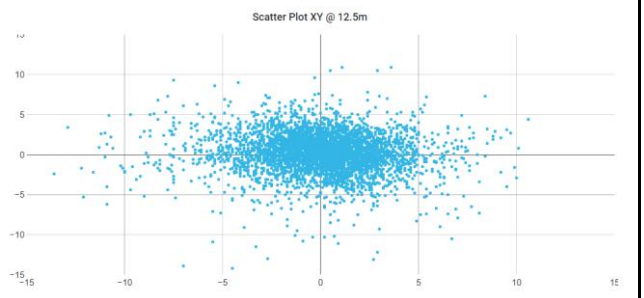

Figure 4.2 - Currents measured by the ADCP currentometer at 4.5, 8.5 and 12.5 m (top to bottom) from the surface over the time periods July, 2 2020 - October, 22 2020 and May, 26 2021 - July, 25 2021.

On average, the intensity of the current during the investigated periods was about 20 cm s^{-1} with some peaks towards the South-East that exceeded 50 cm s^{-1}. The current was also affected, to a lesser extent, by the action of the tide, as shown by the points in the graph in the South-West and North-East quadrants.

Figures 4.3 and 4.4 show the temporal trend of the eastward components (positive values: surface current going to the East; negative values: surface current going to the West) and the northward ones (positive values: surface current going to the North; negative values: surface current going to the South).

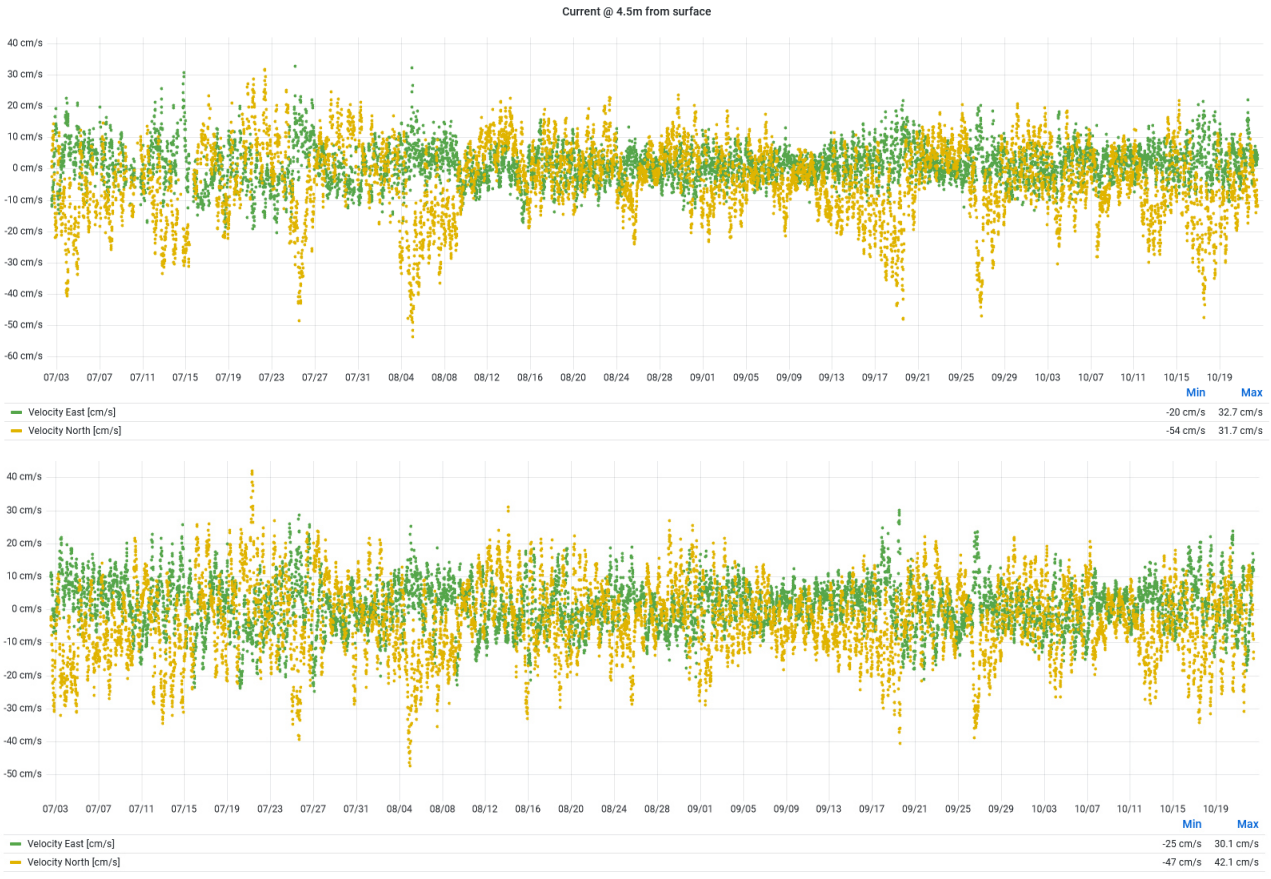

Figure 4.3 - Time series of eastward and northward currents measured at 4.5 - 8.5 - 12.5 m from the surface. Data were recorded every 20 minutes. Time period: July, 2 2020 - October, 22 2020.

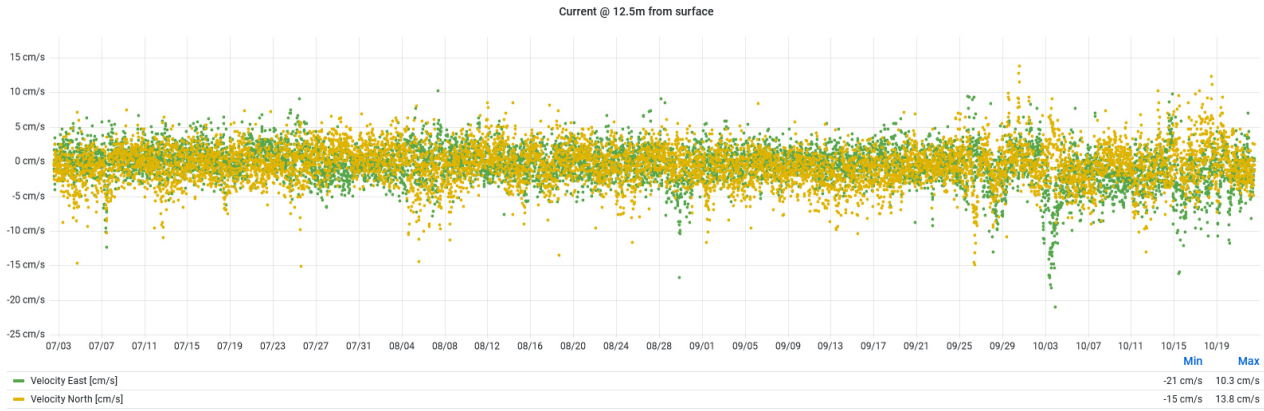

Figure 4.3 - Continue.

As confirmed by the occurrence graph (Figure 4.5) and the numerical values (Table 4.I), it can be concluded that the surface current (4.5m from the surface) measured by the ADCP, on average, has an intensity lower than 20cm s^{-1} and a direction along the NNW-SSE axis. At 8.5 m from the surface, the water current decreases in intensity by about 20% to fade near the bottom where only in some events (18) it exceeded the speed of 15cm s^{-1} due to the friction caused by the seabed.

In conclusion, the results indicate that in the investigated periods it was possible to carry out underwater activities in a comfortable way (surface current <20 cm s^{-1}). Only in the occasion of particular sea and weather events the superficial current exceeded the value of 50 cm s^{-1}. This appears however rather infrequent (7 events during 2020) and has a relatively low duration, lasting on average from 12 to 24 hours. In those conditions the divers would have a bit of difficulty as well as the small-scale fishers for the positioning of the set gears at sea. These activities could benefit from the transmission of data in real time which would allow them to know the oceanographic status before starting their activity.

Figure 4.4 - Time series of eastward and northward currents measured at 4.5 - 8.5 - 12.5 m from the surface. Data were recorded every 20 minutes. Time period: May, 26 2021 - July, 25 2021.

July, 2 2020 - October, 22 2020	May, 26 2021 - July, 25 2021
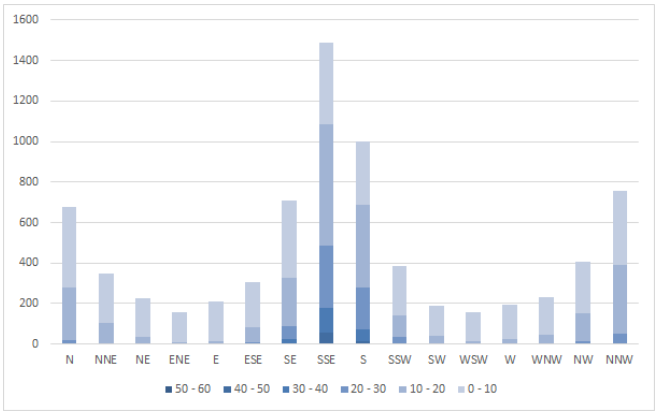	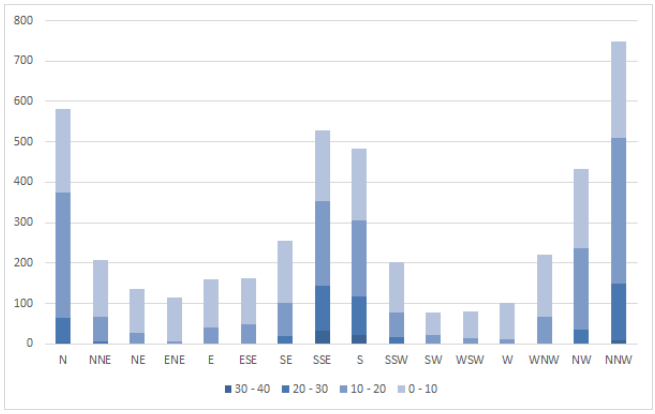
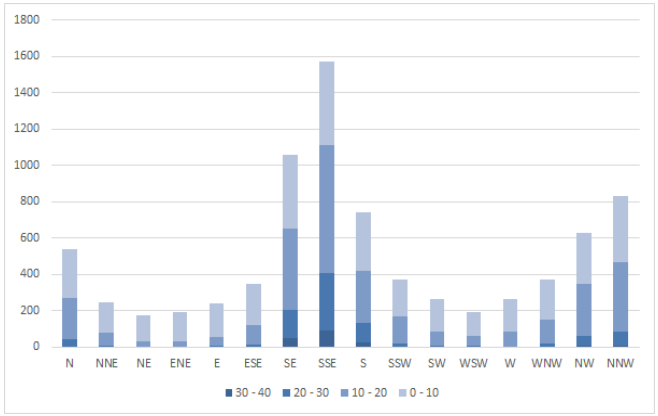	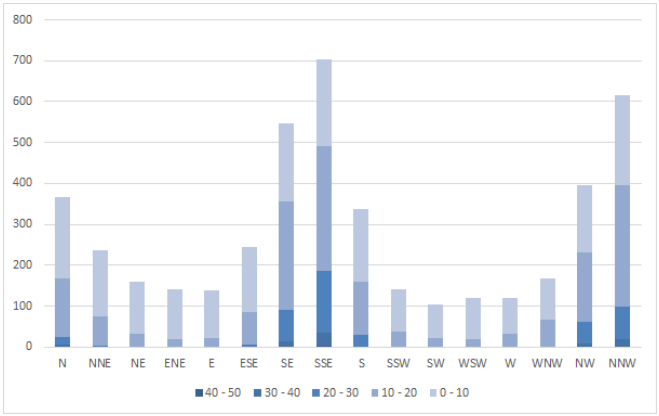
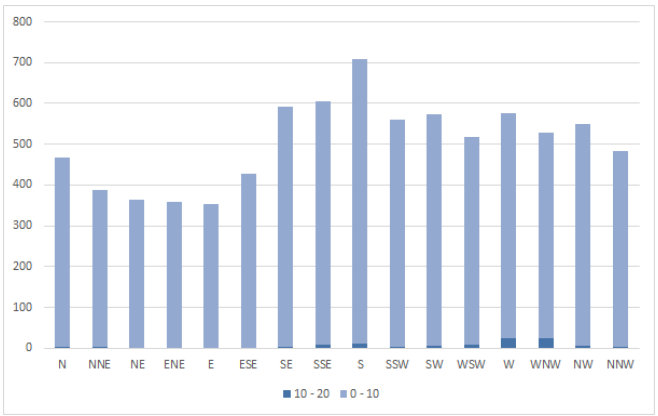	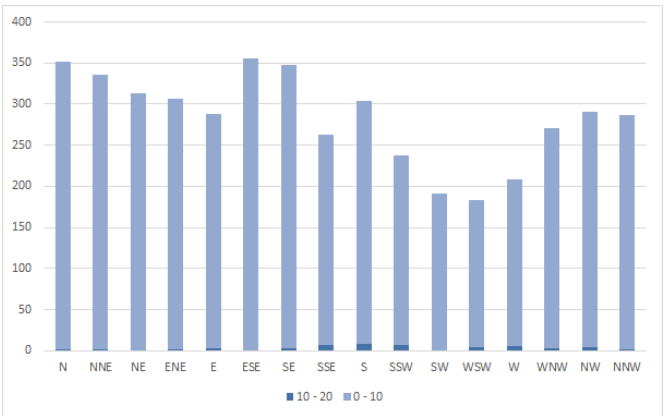

Figure 4.5 - Occurrences of the water current intensities [cm/s] measured by the ADCP currentometer at 4.5, 8.5 and 12.5m from the surface. The first line indicates the reference period.

Table 4.I - Numerical values of occurrences of the water current intensities [%] measured by the ADCP currentometer at 4.5, 8.5 and 12.5m from the surface. The statistical result is obtained by using all the dataset (years 2020 and 2021).

Depth [m]	Speed [cm/s]	Total	%	N	NNE	NE	ENE	E	ESE	SE	SSE	S	SSW	SW	WSW	W	WNW	NW	NNW
4.5	50 - 60	7	0%	0%	0%	0%	0%	0%	0%	14%	71%	14%	0%	0%	0%	0%	0%	0%	0%
	40 - 50	74	1%	0%	0%	0%	0%	0%	0%	0%	77%	22%	0%	0%	0%	0%	0%	0%	1%
	30 - 40	283	2%	1%	0%	0%	0%	0%	1%	9%	55%	27%	1%	0%	0%	0%	0%	1%	5%
	20 - 30	1185	10%	7%	1%	0%	0%	0%	0%	7%	35%	26%	4%	0%	0%	0%	0%	4%	16%
	10 - 20	4162	35%	14%	4%	1%	0%	1%	3%	8%	19%	14%	4%	1%	1%	1%	3%	8%	17%
	0 - 10	6216	52%	10%	6%	5%	4%	5%	5%	9%	9%	8%	6%	3%	3%	4%	5%	7%	10%
8.5	50 - 60	0	-	-	-	-	-	-	-	-	-	-	-	-	-	-	-	-	-
	40 - 50	28	0%	0%	0%	0%	0%	0%	0%	29%	39%	18%	0%	0%	0%	0%	0%	4%	11%
	30 - 40	262	2%	3%	0%	0%	0%	0%	0%	24%	47%	10%	0%	0%	0%	0%	0%	5%	11%
	20 - 30	1273	10%	4%	1%	0%	0%	1%	2%	18%	37%	11%	2%	1%	0%	0%	2%	9%	12%
	10 - 20	4810	38%	8%	3%	1%	1%	1%	4%	15%	21%	9%	4%	2%	2%	2%	4%	9%	14%
	0 - 10	6210	49%	8%	5%	4%	5%	5%	6%	10%	11%	8%	5%	4%	4%	4%	5%	7%	10%
Near Seabed	50 - 60	0	-	-	-	-	-	-	-	-	-	-	-	-	-	-	-	-	-
	40 - 50	0	-	-	-	-	-	-	-	-	-	-	-	-	-	-	-	-	-
	30 - 40	0	-	-	-	-	-	-	-	-	-	-	-	-	-	-	-	-	-
	20 - 30	1	0%	0%	0%	0%	0%	0%	0%	0%	0%	0%	0%	0%	0%	100%	0%	0%	0%
	10 - 20	171	1%	4%	4%	1%	2%	2%	2%	4%	10%	12%	6%	4%	8%	18%	17%	5%	3%
	0 - 10	12406	99%	7%	6%	5%	5%	5%	6%	8%	7%	8%	6%	6%	6%	6%	6%	7%	6%

4.2. Water column parameters

The data of temperature, salinity, oxygen and turbidity recorded continuously by the sensors installed on the oceanographic buoy are shown in Figures 4.6 - 4.8.

During the two time periods the typical cooling of the water column from August 2020 to October 2020 and warming from May 2021 to July 2021 were observed. Temperature values ranged between 17.5°C and 28.5°C (Figure 4.6).

The salinity showed variable values in the first period (Figure 4.7). The presence of less salty water masses of river origin was recorded in several periods when a sharp decrease in salinity occurred. Furthermore, the decreases in salinity were linked to increases in oxygen likely due to oxygenated water of river origin. The salinity values ranged from 33.4 to 37.9. During the second period, instead, the salinity is not reported as the sensor needed calibration. The values will be recalculated following a check and calibration carried out by the manufacturer after the recovery of the oceanographic weather buoy.

The oxygen values recorded in the two periods showed well oxygenated waters (Figure 4.8). The values appeared higher in autumn and spring, seasons characterized by greater mixing of the water column. The weak summer season showed lowest values. Oxygen values ranged from 4.35 to 6.75 ml/l.

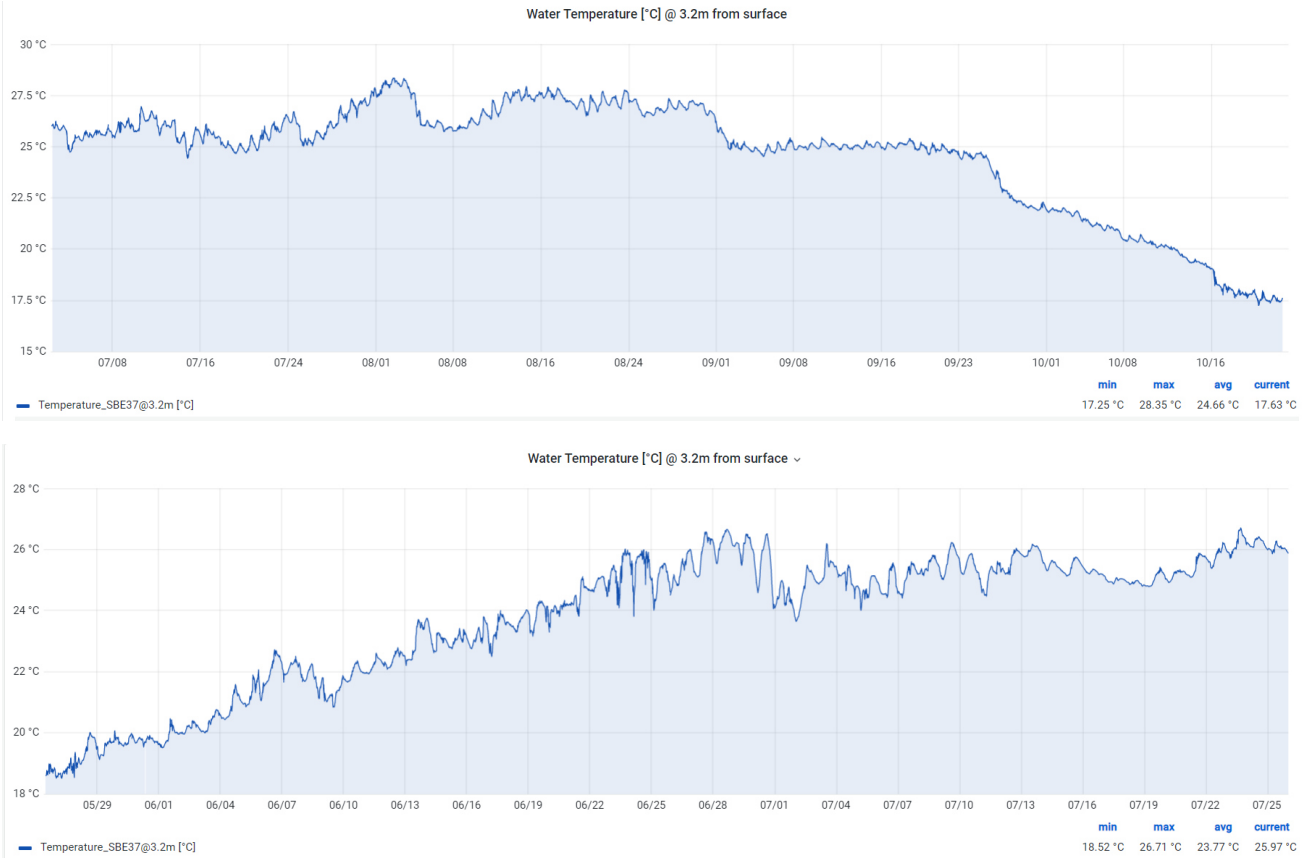

Figure 4.6 - Water temperature [°C] measured at 3.2m from the surface. Periods: July, 2 2020 - October, 22 2020 (top); May, 26 2021 - July, 25 2021 (bottom).

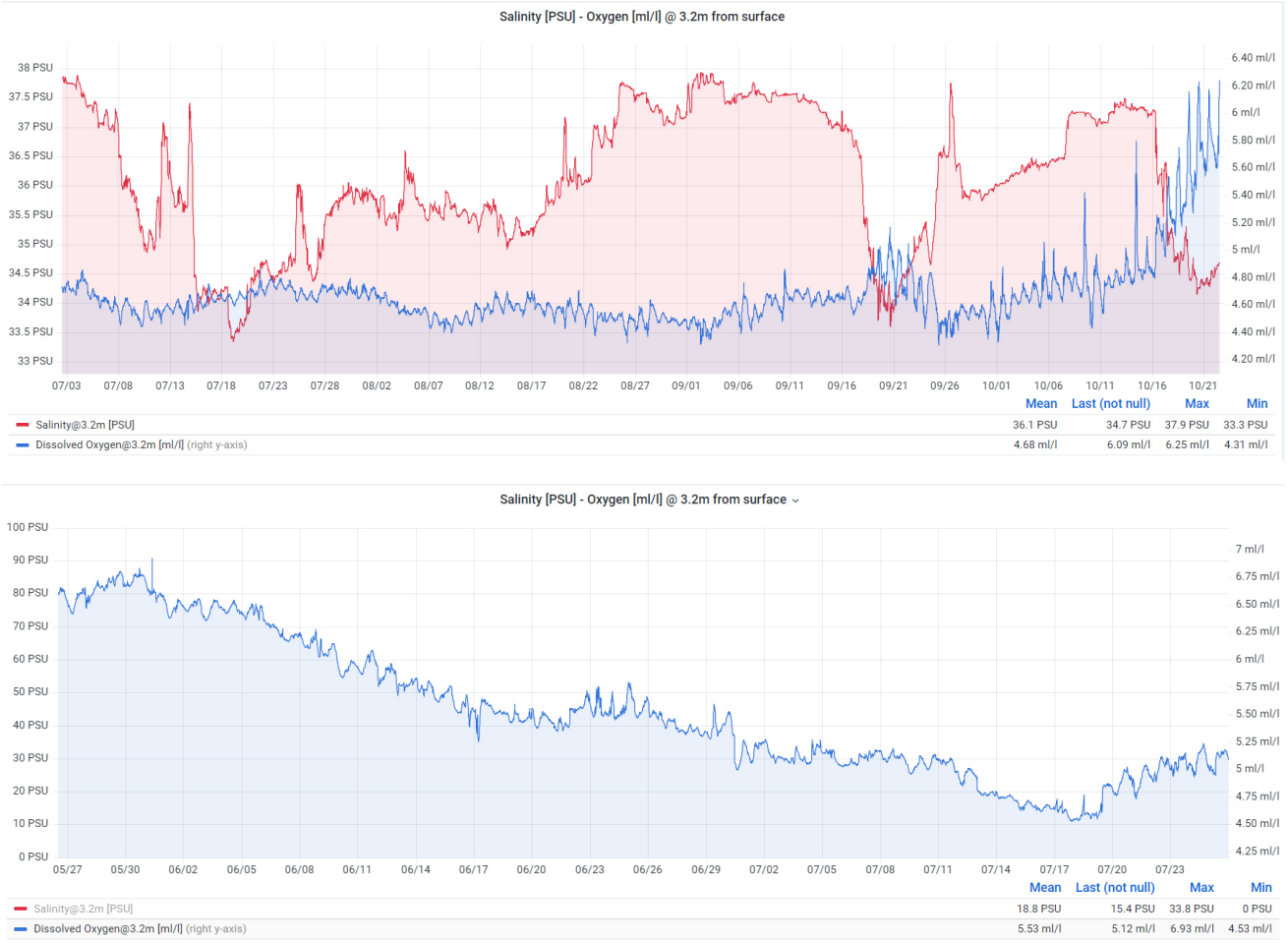

Figure 4.7 - Salinity [PSU] (red line) and Oxygen concentration [ml/l](blue line) measured at 3.2m from the surface in the period July, 2 2020 - October, 22 2020 (top) and Oxygen concentration recorded at 3.2m from the surface in the period May, 26 2021 - July, 25 2021 (bottom).

Regarding the turbidity (Figure 4.8), in 2020 the sensor worked correctly until August 12 and then it was completely enveloped by the biofouling which prevented its correct functioning. From July 2 to August 12 the average turbidity was around 2 NTU at 3.2m from the surface which allows good visibility to divers.

In the period from May 26, 2021 to date, the sensor has worked correctly even though the values show some spykes titles of the parameter. Turbidity considerably increased from 17 to 21 July 2021 due to local resuspension and river sediment transport after a few days of heavy rain.

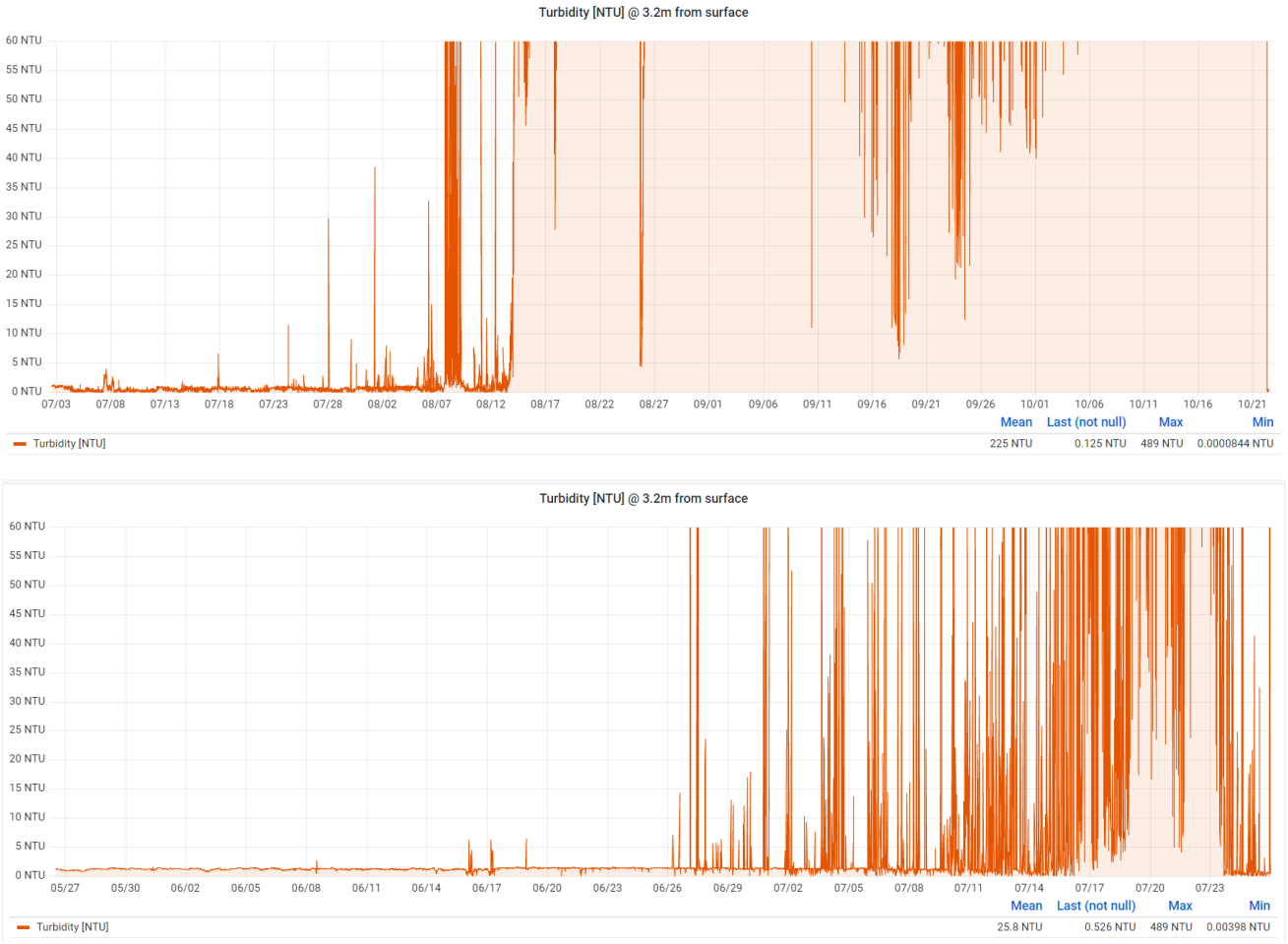

Figure 4.8 - Turbidity [NTU] measured at 3.2m from the surface.Periods: data from July, 2 2020 to October, 22 2020 (top) and data from May, 26 2021 to July, 25 2021 (bottom)

The physical (temperature, salinity, turbidity) and bio-chemical (chlorophyll, oxygen, nutrients) parameters monitored in the AR area throughout oceanographic cruises were very variable between October 2020 and June 2021 (Figures 4.9 - 4.14). However, in the overall, they agreed with the values recorded in continuous by the sensors mounted on the buoy.

In fact, also in this case the natural winter cooling of seawater followed by spring-summer heating was observed during the survey period (Figures 4.9 - 4.12). The temperature values ranged between about 9.5°C, detected in January 2021, and 25.5°C in June 2021.

The area appeared to be influenced by the presence of the Musone river mouth located slightly further North. In particular, less salty surface waters were observed in January and May 2021 throughout the area and only in some surface stations in June 2021 (Figures 4.9 - 4.12). The salinity ranged between about 31 in January 2021 and about 38.5 in June 2021, when a typical summer stratification of the water column was observed (Artegiani *et al*., 1997a and 1997b).

The turbidity distribution (Figures 4.9 - 4.12) showed ever higher values near the bottom where mixing processes were active. Furthermore, high surface turbidity values in correspondence with less salty waters of riverine origin were found. The turbidity values ranged between 0.5 and 8 NTU.

The whole water column appeared well oxygenated throughout the monitoring period (Figures 4.9 - 4.12). The oxygen saturation values ranged between 85-90% and 100-105%. The investigated area has never been subjected to hypoxia phenomena.

Chlorophyll showed strong variations over the investigation period (Figures 4.9 - 4.12). The highest concentrations were observed in January 2021 (9-12 µg/l), likely due to phytoplankton winter blooms as observed in Adriatic coastal areas by Totti *et al*. (2019). The lowest values over the entire water column (0.5-1.5 µg/l) were instead recorded in June 2021.

The temporal evolution of the distribution of dissolved nutrients showed some differences between the surface and the bottom (Figures 4.13 and 4.14).

In October 2020 and January 2021 the distribution of nitrites reached higher values on the surface, gradually decreasing towards the summer period while lower and fairly uniform values were observed at the bottom throughout the sampling period. The concentrations ranged between 0.02 and 1.117 µM.

Nitrates showed similar distributions between the surface and the bottom. The concentrations increased from October 2020 to January 2021 and then decreased throughout June 2021, when they reached the lowest values. Nitrate concentrations ranged between 0.02 and 15.473 µM.

Low values of Ammonium were recorded throughout the area with few exceptions. In particular, higher concentrations were observed in June 2021 close to the bottom of stations A1 and A7, where high values of nitrates were also observed. This could be due to mineralization processes at the bottom. The values of Ammonium ranged from 0.02 to 11.527 µM.

The concentrations of orthosilicates showed a quite similar range between surface and bottom, varying from 2.09 to 10.32 µM (surface) and from 1.43 to 13.00 µM (bottom). On the bottom, an increase was observed from October 2020 to June 2021. This increase was not so evident on the surface that showed more variable values. The concentrations ranged between 1.429 and 13.003 µM.

Finally, the values of the orthophosphates were low during the overall investigated area both at the surface and on the bottom. The concentrations ranged from 0.03 to 0.482 µM. Relatively higher values were observed at the bottom of some stations in January 2021.

In the overall, the seasonal trends of physical and bio-chemical parameters recorded in the investigation area were comparable to those commonly observed in the coastal areas of the western Adriatic Sea (Zavatarelli *et al.*, 1998; Grilli *et al.*, 2020).

The data obtained by the monitoring show suitable temperatures for diving from the end of May until the first half of October (T≥20°C). However, the frequent high turbidity close to the seabed could represent a limitation for this recreational activity. On the other hand, all the physical and bio-chemical parameters, especially the absence of hypoxia phenomena, highlight suitable conditions for the occurrence of an abundant and diversified fish population that could be attractive either for divers and for recreational or professional fishers.

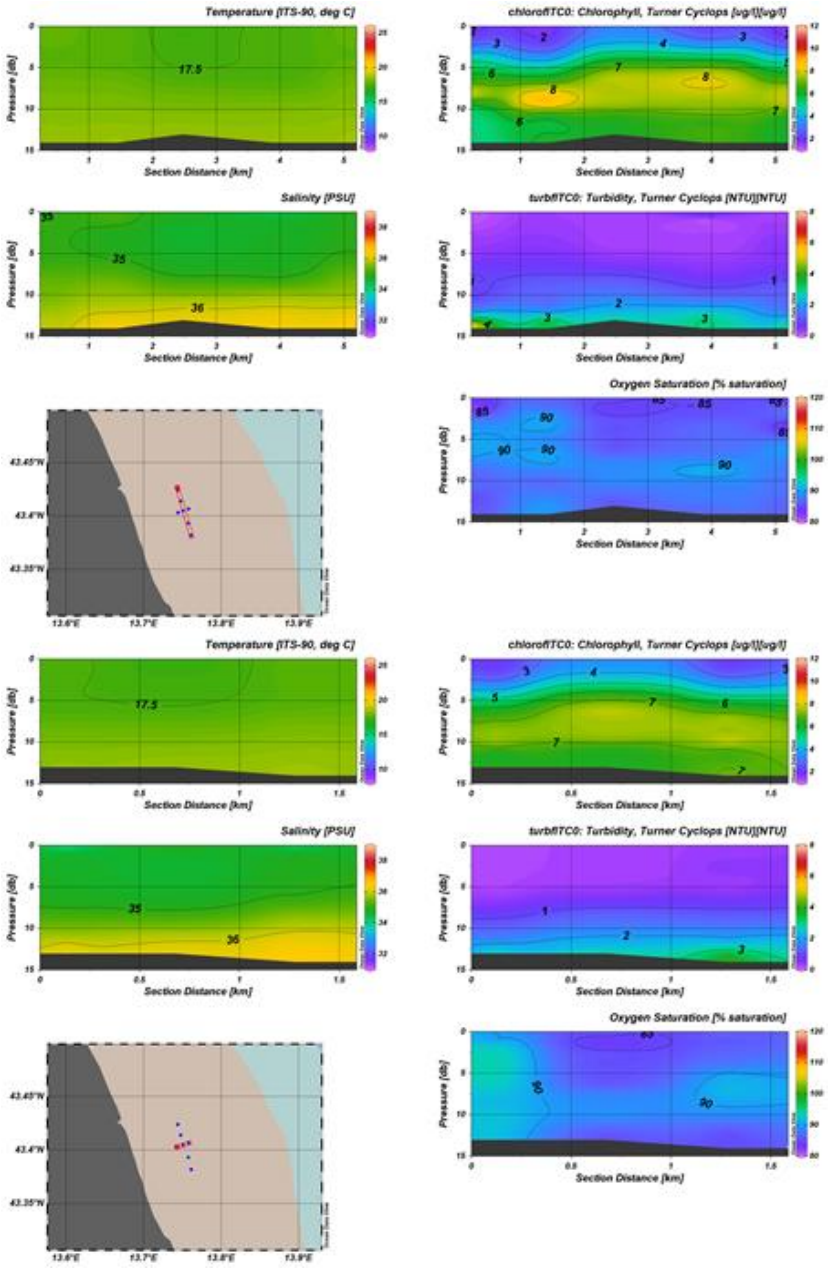

Figure 4.9 - A1-A5 and A6-A7 sections of temperature, salinity, chlorophyll (fluorescence), turbidity and oxygen saturation. Cruise of October 22, 2020.

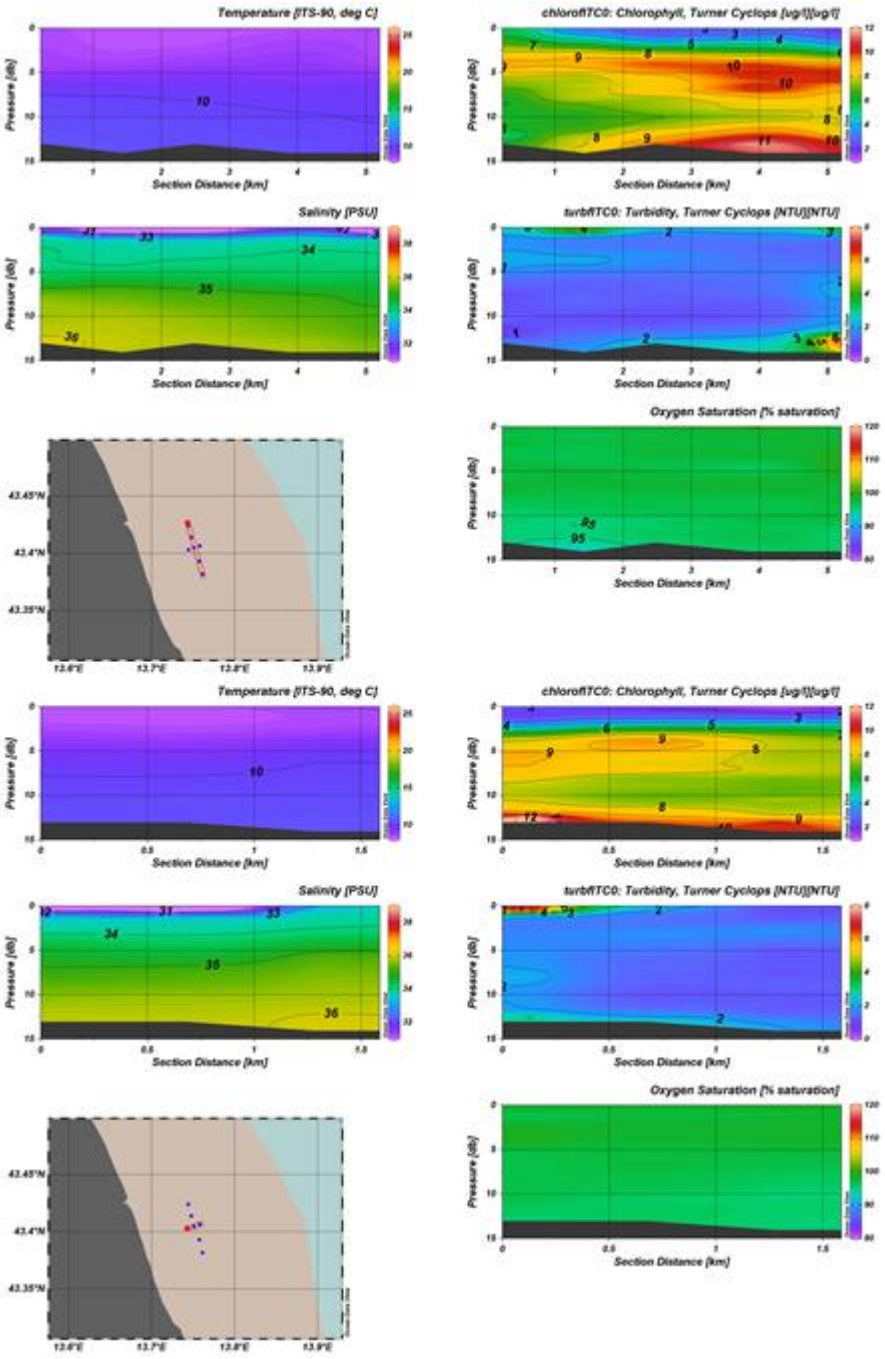

Figure 4.10 - A1-A5 and A6-A7 sections of temperature, salinity, chlorophyll (fluorescence), turbidity and oxygen saturation. Cruise of January 20, 2021.

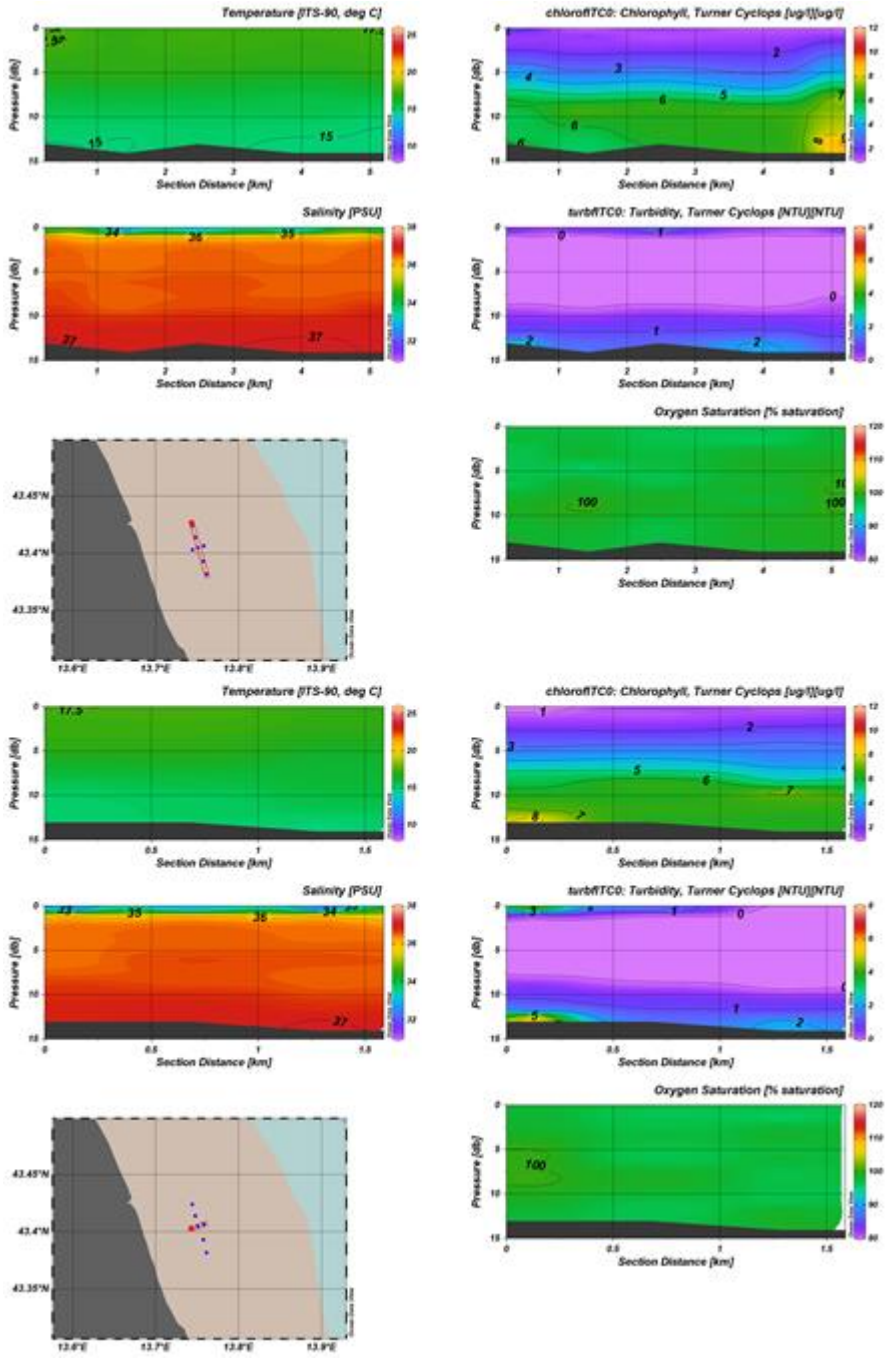

Figure 4.11 - A1-A5 and A6-A7 sections of temperature, salinity, chlorophyll (fluorescence), turbidity and oxygen saturation. Cruise of May 11, 2021.

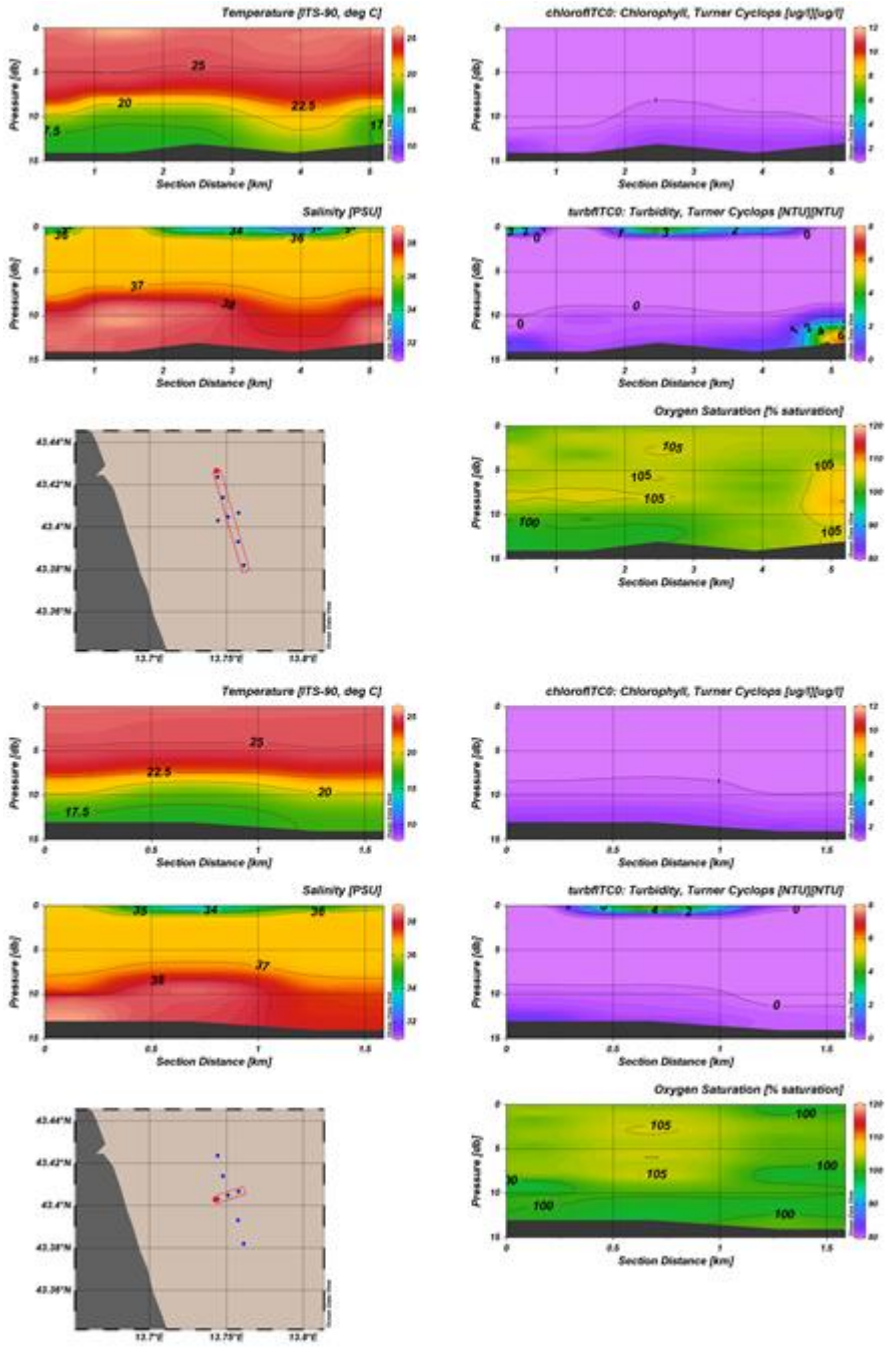

Figure 4.12 - A1-A5 and A6-A7 sections of temperature, salinity, chlorophyll (fluorescence), turbidity and oxygen saturation. Cruise of June 22, 2021.

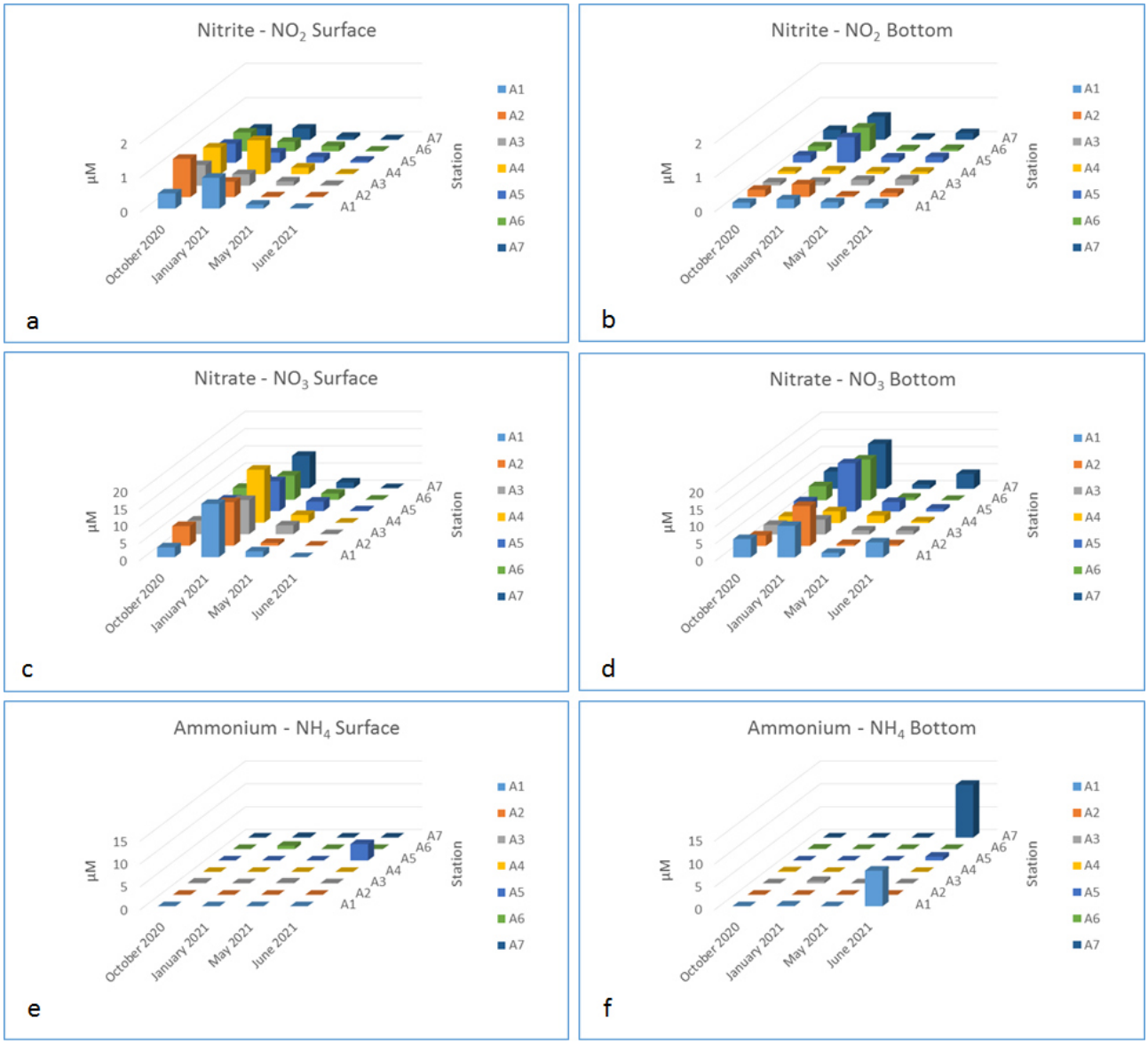

Figure 4.13 - Surface and bottom values of nitrite (a, b), nitrate (c, d) and ammonium (e, f) at A1-A7 stations in the four periods of sampling - October 2020, January 2021, May 2021, and June 2021.

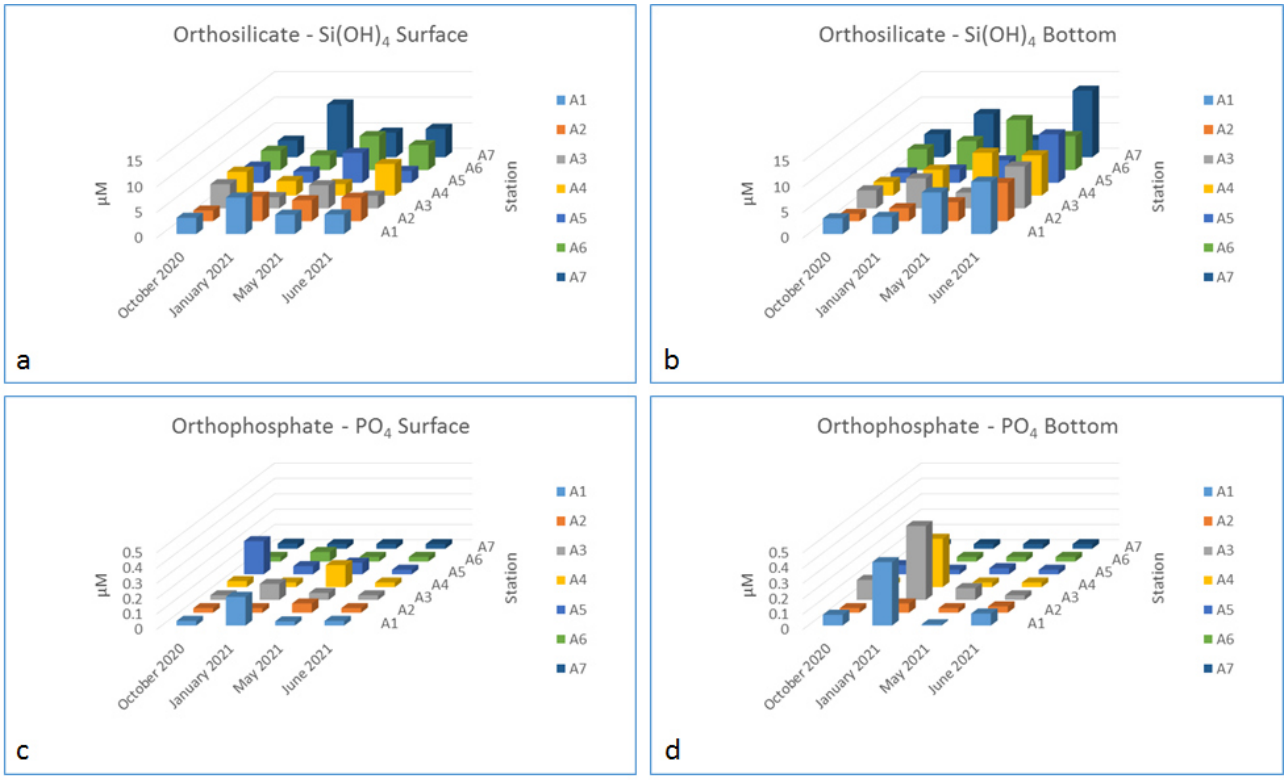

Figure 4.14 - Surface and bottom values of orthosilicate (a, b) and orthophosphate (c, d) at A1-A7 stations in the four sampling periods: October 2020, January 2021, May 2021, and June 2021.

4.3. Benthic community settled on the artificial reef

In total, 32 taxa were found during the whole sampling period and in overall sampling sub-areas (Table 4.II). Fiftysix percent of the taxa were colonials and 34% solitaries (Figure 4.15). Bryozoa and Porifera represented the most numerous taxonomic groups, each contributing to 19% of the total number of taxa, followed by Anthozoa (16%), Crustacea (9%), Gastropoda (6%), Bivalvia (6%), Polychaeta (6%), Ascidiacea (3%), Hydrozoa (3%), Echinodermata (3%) and other taxa (each < 1%).

Table 4.II - List of taxa observed during the overall sampling period.

Total taxon list	
1 Actiniaria nd. (Cereus sp. type)	17 M. galloprovincialis
2 Actiniaria nd.	18 Nudibranchia (Flabellina sp.)
3 Actiniaria nd. (Actinia equina type)	19 Ophiothrix fragilis
4 Algae nd.	20 Ostrea edulis
5 Anthozoa nd.	21 Paguridae nd.
6 Ascidiacea nd.	22 Polychaeta (Sabellidae Type)
7 Balanidae nd.	23 Polychaeta (tube)
8 Bryozoa-Hydrozoa	24 Porifera nd. (black)
9 Bryozoa nd.	25 Porifera nd. (brownish)
10 Bryozoa nd. (Amathia-Bugula type)	26 Porifera nd. (gray)
11 Bryozoa nd. (white)	27 Porifera nd. (white)
12 Decapoda nd. (Brachyura)	28 Porifera nd. (yellow)
13 Demospongiae nd. (Tethya aurantium Type)	29 Schizoporelloidea nd. (brownish)
14 Epizoanthus sp.	30 Schizoporelloidea nd. (red)
15 Hexaplex Trunculus	31 Serpulidae nd. - Hydrozoa nd.
16 Hydrozoa nd.	32 Sipunculidae nd.

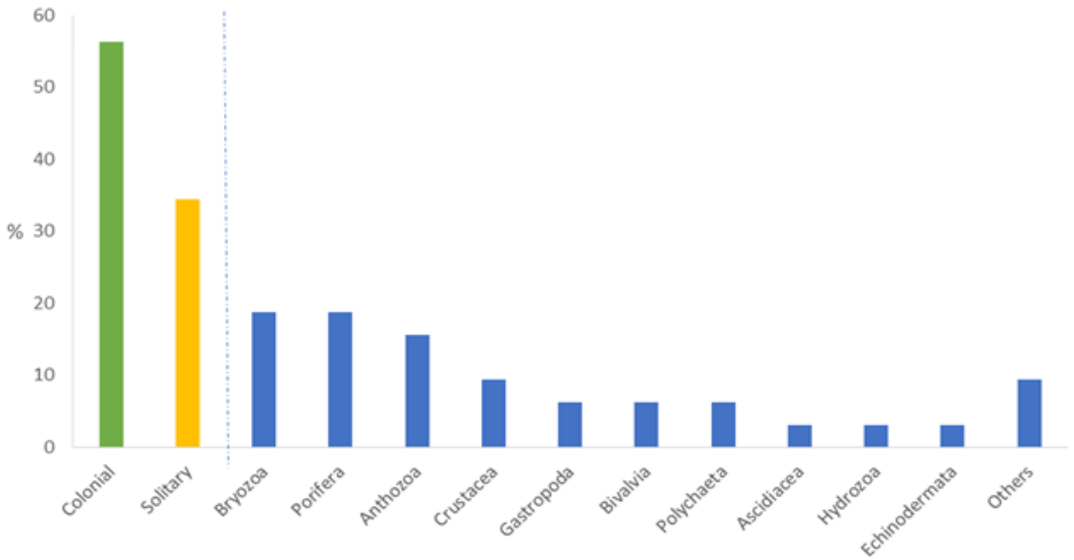

Figure 4.15 - Percentage of taxa per living habit (first 2 columns) and of the taxa (blue columns on the right) found in the overall sampling period.

Taking into consideration all the three sub-areas, the highest coverage percentage, with an average of 77% ($p<0.01$), was recorded in 2021, while similar values were recorded in 2019 (59%) and 2020 (57%) (Figure 4.16).

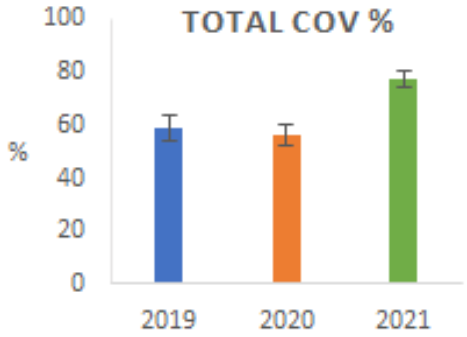

Figure 4.16 - Total coverage (%) with related standard errors by year.

The average coverage percentage on the overall sampling period was 67% in A area, followed by 66% and 60% in B and C areas respectively (Figure 4.17a). In 2019, the highest average coverage was recorded in C area (67%), while A area represented, on average, the most epiphyted one (67%) in 2020 and B area in 2021 (81%), even though no significant differences were found (Figure 4.17a).

The upper block was the most covered one considering either the overall sampling period (72%) and the years 2020 and 2021, when an average coverage of 68% and 88% respectively was found ($p<0.01$; Figure 4.17b). In 2019, instead, similar coverage values were observed on the base and upper blocks (59%; $p>0.05$).

Moreover, the coverage percentage on the vertical slopes was higher than on the horizontal ones considering either the entire sampling period (77%) and the years 2019 and 2021 ($p<0.05$), with a coverage of 83% and 86% respectively. In 2020, instead, no significant differences were found (Figure 4.17c).

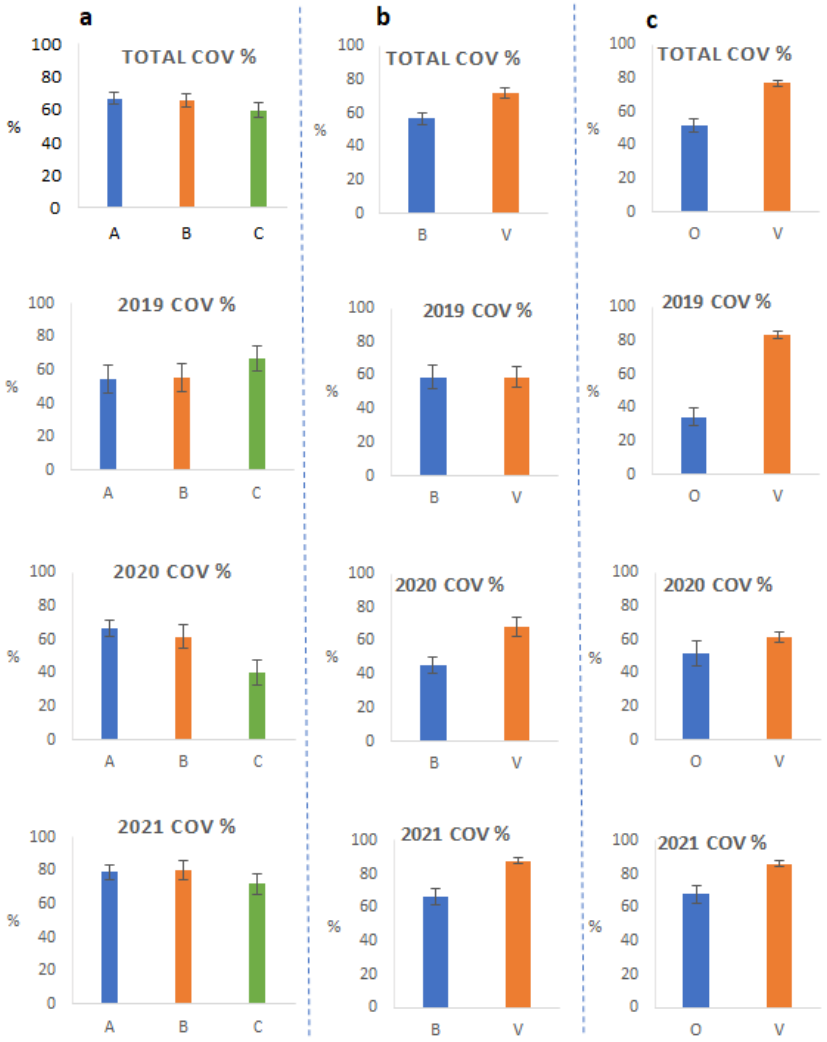

Figure 4.17 - Coverage percentage with related standard errors by area (a), depth (b), and slope (c) on the overall sampling period and in each year.

Considering the taxa composition of the benthic communities settled on the pyramids, the Shapiro-Wilk test performed on the years, and on the "area", "depth" and "slope" levels, showed no data with a normal distribution (Table 4.III).

The Wilcoxon signed-rank test, performed on the years, and on the "area", "depth" and "slope" levels showed dissimilarity in the biogenic structure between the years 2019 and 2020 and between the two levels "horizontal" and "vertical" of the "slope" factor ($p<0.05$; Table 4.III).

Table 4.III - Shapiro-Wilk test of normality and Paired Samples T-Test (Wilcoxon signed-rank test, 0.05≤p<0.01 = significant; p≤0.01 = highly significant) performed on the average coverage percentage of the years and the factors area, depth and slope. The significant results are highlighted in yellow.

Test of Normality (Shapiro-Wilk)				
Year			W	p
2019	-	2020	0.806	< .001
2019	-	2021	0.928	< .001
2020	-	2021	0.884	< .001
Area				
A	-	B	0.951	< .001
A	-	C	0.888	< .001
B	-	C	0.929	< .001
Depth				
B	-	V	0.954	< .001
Slope				
O	-	V	0.941	< .001

Note. Significant results suggest a deviation from normality.

Paired Samples T-Test				
Measure 1		Measure 2	W	p
2019	-	2020	1675	0.005
2019	-	2021	1672	0.805
2020	-	2021	1214	0.074
A	-	B	5438	0.999
A	-	C	4505	0.463
B	-	C	4782	0.292
B	-	V	6546	0.547
O	-	V	3824	< .001

Note. Wilcoxon signed-rank test.

SIMPER analysis, performed on the years 2019 and 2020, showed that *M. galloprovincialis* and *Epizoanthus* sp. were the major contributors to the dissimilarity (Table 4.IV). *M. galloprovincialis*, *Epizoanthus* sp., Schizoporelloidea nd. (red), and Hydrozoa nd. were more abundant in 2019, while *Porifera* nd. (yellow) and Algae nd. in 2020 (Figure 4.18).

The taxa that mostly contributed to the dissimilarity between the two "slope" levels, instead, were *Epizoanthus* sp. and *M. galloprovincialis* (Table 4.V). *M. galloprovincialis* and Algae nd., indeed, were the taxa that mostly contributed to the composition of the benthic population on the horizontal surfaces, while *Epizoanthus* sp., Hydrozoa nd. and Schizoporelloidea nd. (red) mostly populated the vertical ones (Figure 4.19).

Table 4.IV - SIMPER analysis performed between the years 2019 and 2020.

Taxon	Av. dissim	Contrib. %	Cumulative %	Taxon	Av. dissim	Contrib. %	Cumulative %
M. galloprovincialis	7.89	22.90	22.90	Actiniaria nd.	0.20	0.57	98.00
Epizoanthus sp.	6.84	19.85	42.75	Ophiothrix fragilis	0.19	0.54	98.53
Schizoporelloidea nd. (red)	2.78	8.06	50.81	Bryozoa nd. (Amathia-Bugula type)	0.10	0.30	98.84
Porifera nd. (yellow)	2.65	7.70	58.51	Demospongiae nd. (Tethya aurantium Type)	0.08	0.23	99.07
Algae nd.	2.61	7.58	66.09	Balanidae nd.	0.06	0.16	99.23
Hydrozoa nd.	2.57	7.46	73.55	Hexaplex Trunculus	0.05	0.15	99.38
Serp. sp. - Hydr. sp.	1.76	5.09	78.64	Nudibranchia (Flabellina sp.)	0.05	0.15	99.53
Ostrea edulis	1.23	3.56	82.20	Sipunculidae nd.	0.04	0.12	99.64
Bryo-Hydrozoa	1.17	3.39	85.59	Anthozoa nd.	0.03	0.09	99.73
Porifera nd. (brownish)	1.07	3.09	88.68	Actiniaria nd. (Actinia equina type)	0.02	0.07	99.80
Shell (empty)	0.83	2.41	91.09	Polychaeta (tube)	0.02	0.06	99.87
Porifera nd. (gray)	0.79	2.28	93.37	Actiniaria (Cereus sp. type)	0.02	0.06	99.92
Porifera nd. (white)	0.46	1.34	94.71	Decapoda nd. (Brachyura)	0.01	0.03	99.95
Bryozoa nd. (white)	0.28	0.80	95.51	Polychaeta (Sabellidae Type)	0.01	0.02	99.98
Schizoporelloidea nd. (brownish)	0.24	0.70	96.22	Ascidiacea nd.	0.00	0.01	99.99
Bryozoa nd.	0.22	0.63	96.84	Paguridae nd.	0.00	0.01	100.00
Porifera nd. (black)	0.20	0.58	97.43				

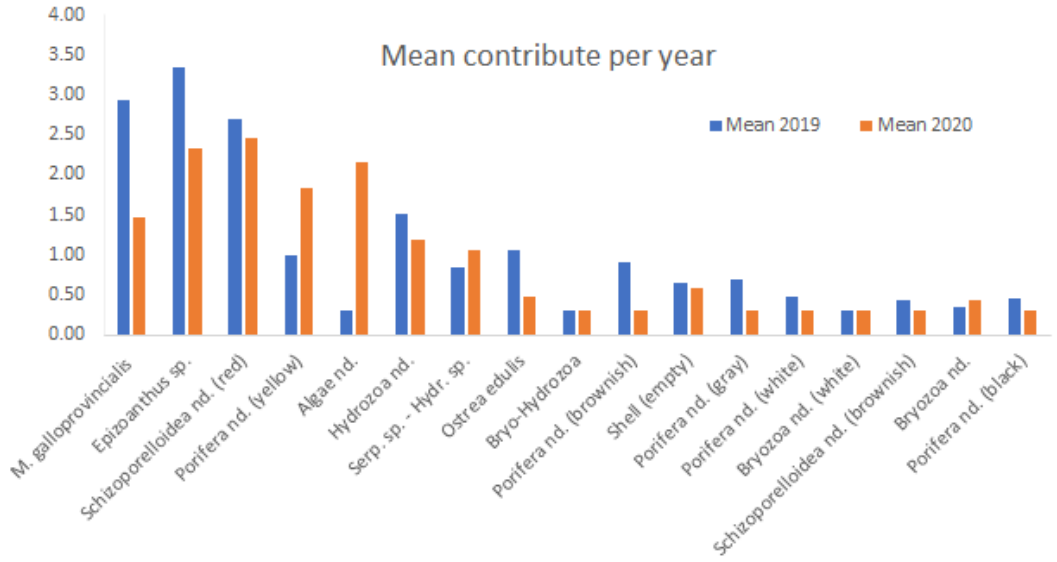

Figure 4.18 - Mean contribution of each taxon in 2019 and 2020. Values below 0.5% are not displayed.

Table 4.V - SIMPER analysis performed on the "slope" levels.

Taxon	Av. dissim	Contrib. %	Cumulative %	Taxon	Av. dissim	Contrib. %	Cumulative %
Epizoanthus sp.	11.62	29.66	29.66	Actiniaria nd.	0.21	0.53	98.17
M. galloprovincialis	7.40	18.88	48.54	Ophiothrix fragilis	0.19	0.50	98.67
Hydrozoa nd.	2.92	7.46	56.00	Bryozoa nd. (Amathia-Bugula type)	0.11	0.28	98.95
Schizoporelloidea nd. (red)	2.86	7.29	63.29	Demospongiae nd. (Tethya aurantium Type)	0.08	0.21	99.16
Porifera nd. (yellow)	2.68	6.84	70.13	Balanidae nd.	0.06	0.15	99.31
Algae nd.	2.40	6.14	76.27	Hexaplex Trunculus	0.06	0.15	99.46
Serp. sp. - Hydr. sp.	1.72	4.38	80.65	Nudibranchia (Flabellina sp.)	0.05	0.14	99.59
Ostrea edulis	1.26	3.22	83.87	Sipunculidae nd.	0.04	0.09	99.69
Bryo-Hydrozoa	1.23	3.13	87.00	Anthozoa nd.	0.03	0.07	99.76
Porifera nd. (brownish)	1.01	2.59	89.58	Actiniaria nd. (Actinia equina type)	0.03	0.07	99.83
Porifera nd. (gray)	0.87	2.23	91.81	Polychaeta (tube)	0.02	0.06	99.89
Shell (empty)	0.85	2.18	93.99	Actiniaria (Cereus sp. type)	0.02	0.05	99.93
Porifera nd. (white)	0.44	1.14	95.12	Decapoda nd. (Brachyura)	0.01	0.02	99.96
Bryozoa nd. (white)	0.29	0.74	95.86	Polychaeta (Sabellidae Type)	0.01	0.02	99.98
Schizoporelloidea nd. (brownish)	0.26	0.67	96.53	Paguridae nd.	0.00	0.01	99.99
Bryozoa nd.	0.23	0.58	97.11	Ascidiacea nd.	0.00	0.01	100.00
Porifera nd. (black)	0.21	0.54	97.64				

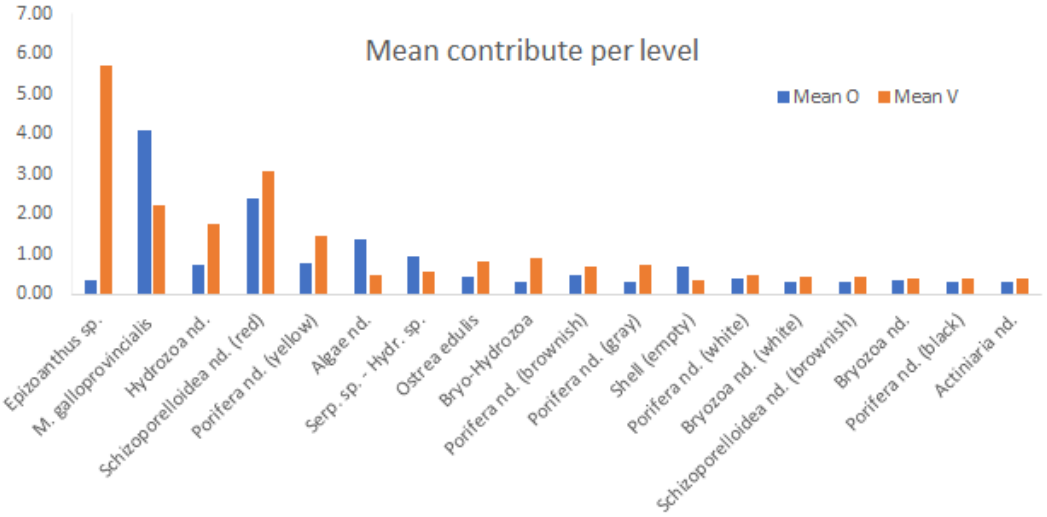

Figure 4.19 - Mean contribution of each taxon on the horizontal (O) and vertical (V) levels of the "slope" factor. Values below 0.5% are not displayed.

The Student's t-test test performed between the horizontal (O) and vertical (V) "slope" levels by year, area and depth level, showed significant differences in 2019 on the bottom block in A area and on the upper one in B area. Statistical differences were also observed almost everywhere with the exception of the bottom block of B area in 2020 and only on the bottom and upper blocks of C area in 2021 (Table 4.VI).

Table 4.VI - Shapiro-Wilk test of normality and Paired Samples T-Test (Wilcoxon signed-rank test, and Student's t-test, $p < 0.05$) performed on the coverage percentage of the slope variables per each year and per area and depth factors. Highlighted in yellow the significant results.

Test of Normality (Shapiro-Wilk) $p < 0.05$

Year	Area	Depth	*Slope*		*Slope*	W	p
2019	A	B	O	-	V	0.853	0.235
2019	A	V	O	-	V	0.916	0.517
2019	B	B	O	-	V	0.87	0.296
2019	B	V	O	-	V	0.875	0.317
2019	C	B	O	-	V	0.695	0.01
2019	C	V	O	-	V	0.667	0.005
2020	A	B	O	-	V	0.935	0.624
2020	A	V	O	-	V	0.909	0.479
2020	B	B	O	-	V	0.964	0.804
2020	B	V	O	-	V	0.827	0.16
2020	C	B	O	-	V	0.951	0.725
2020	C	V	O	-	V	0.947	0.699
2021	A	B	O	-	V	0.865	0.279
2021	A	V	O	-	V	0.872	0.304
2021	B	B	O	-	V	0.868	0.291
2021	B	V	O	-	V	0.949	0.712
2021	C	B	O	-	V	0.927	0.579
2021	C	V	O	-	V	0.977	0.884

Note. Significant results suggest a deviation from normality.

Paired Samples T-Test $(p < 0.05)$

Year	Area	Depth	*Slope*		*Slope*	Test	Statistic	df	p
2019	A	B	O	-	V	Student	-16.4	3	< .001
2019	A	V	O	-	V	Student	-2.35	3	0.1
2019	B	B	O	-	V	Student	-2.17	3	0.118
2019	B	V	O	-	V	Student	-8.57	3	0.003
2019	C	B	O	-	V	Wilcoxon	1		0.25
2019	C	V	O	-	V	Wilcoxon	0		0.125
2020	A	B	O	-	V	Student	3.378	3	0.043
2020	A	V	O	-	V	Student	7.965	3	0.004
2020	B	B	O	-	V	Student	-2.59	3	0.081
2020	B	V	O	-	V	Student	4.25	3	0.024
2020	C	B	O	-	V	Student	-13.1	3	< .001
2020	C	V	O	-	V	Student	-11.9	3	0.001
2021	A	B	O	-	V	Student	-1.73	3	0.183
2021	A	V	O	-	V	Student	1.72	3	0.184
2021	B	B	O	-	V	Student	-2.79	3	0.069
2021	B	V	O	-	V	Student	1.139	3	0.337
2021	C	B	O	-	V	Student	-4.51	3	0.02
2021	C	V	O	-	V	Student	-8.93	3	0.003

Taking in account the significant dissimilarities (Tab. 4.VI), the Flexplot showed higher coverage values on the vertical slope in respect to the horizontal one on the bottom block of A area in 2019, while in 2020 the horizontal slope was more covered in both blocks (Figure 4.20). A similar situation occurred on the upper block of B area in 2019 and 2020. Higher coverages were instead observed on the vertical slopes of the lower and upper blocks of the pyramids in the C area in 2020 and 2021.

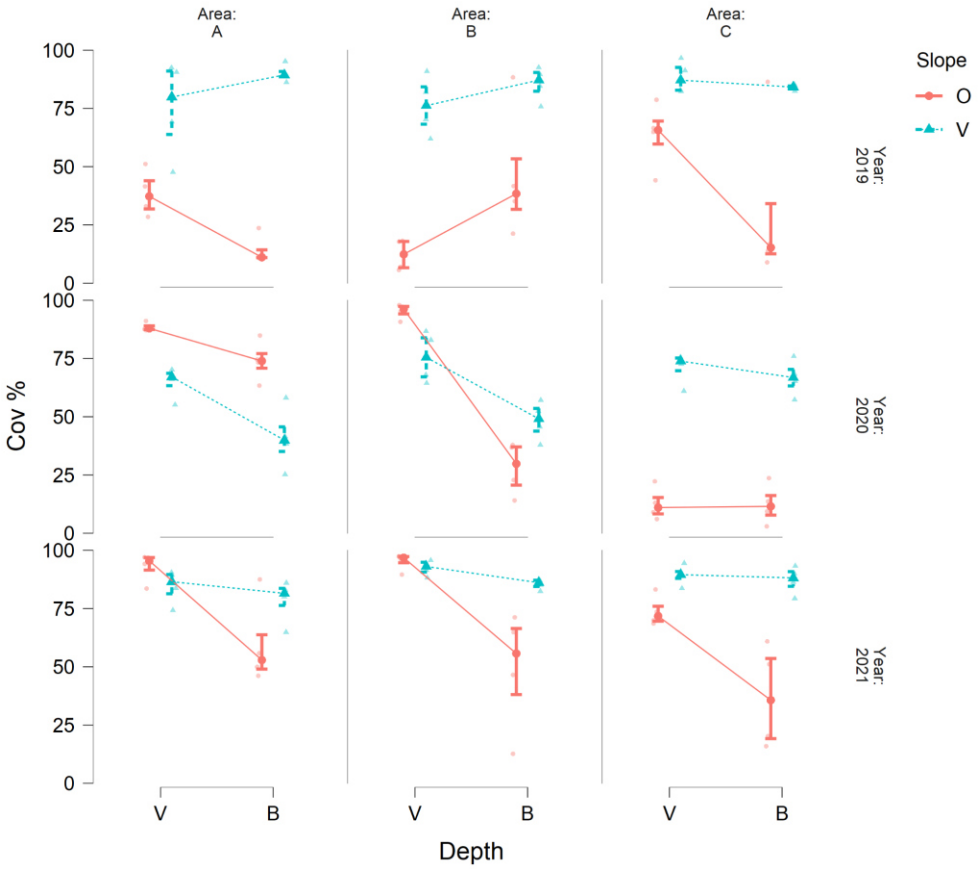

Figure 4.20 - Flexplot. Average coverage percentage with associated standard errors in each year displayed as slope levels per depth levels in each area.

Amongst the mobile taxa, it is noticeable the occurrence of several specimens of the nudibranch *Flabellina* sp. at the AR (Figure 4.21). This species, as most species belonging to the Flabellinidae family, feeds on the stinging polyps of hydroids to use the stinging cells for its defense. Due to its enchanting colours, *Flabellina* sp. is certainly one of the invertebrates at the top of the podium of amateur underwater photography.

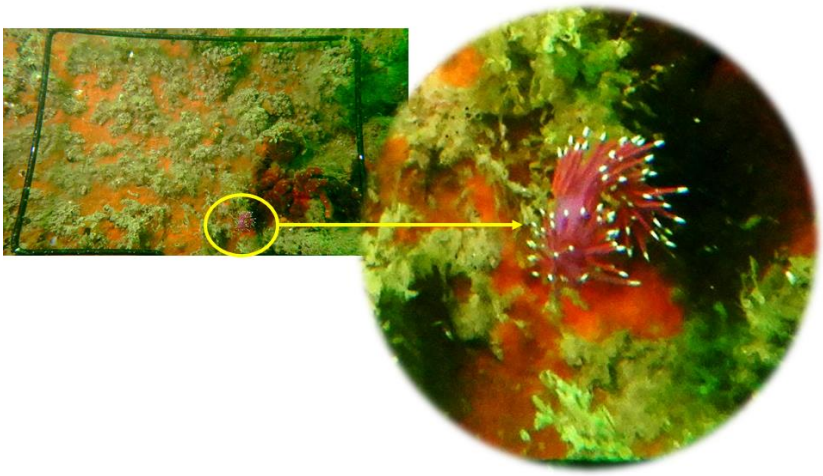

Figure 4.21 - Flabellina sp. on the artificial reef.

Another noteworthy species, appreciated by divers for its sinuosity and colors, is the brittle star *Ophiotrix fragilis*. Several individuals of this species were found in 2021 on the upper and bottom blocks of the A area (Figure 4.22).

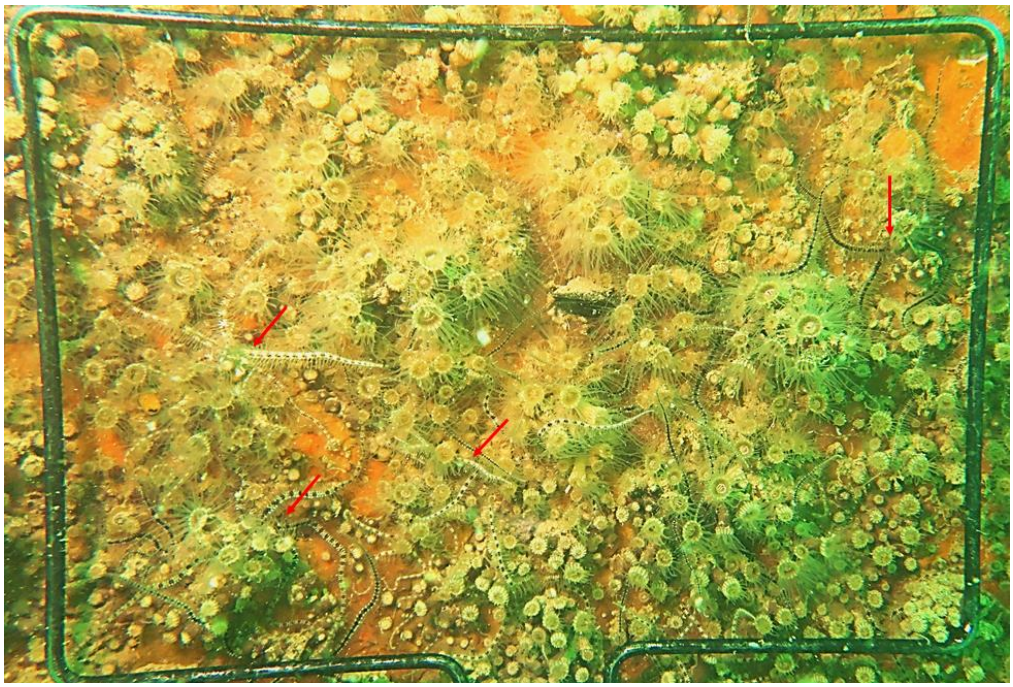

Figure 4.22 - Ophiothrix fragilis on the pyramids of the artificial reef.

In general, the coverage data show a good colonization of the AR structures by benthic taxa. The occurrence of a diversified community, similar to that settled on natural rocky bottoms, as well as the presence of species of interest make the artificial substrates attractive for scuba divers. The presence of a well developed benthic population also represents a feeding source for reef-dwelling fish with a consequent enrichment of the fish assemblage, which makes the area also suitable for the recreational and professional fisheries.

4.4. Mussel population

4.4.1. Population structure

The density of mussels collected in June 2021 from the 3 sub-areas ranged between 569 ind/m^2 and 20756 ind/m^2 with a size range between 0.5mm and 82.8mm SL.

Both on the pyramids and on poles the highest densities and biomasses were recorded at a distance >2m from the seafloor (Figure 4.23; Table VII), according to what reported in previous studies which evidenced how the settlement density decreases with increasing depth (Fabi *et al*., 1989).

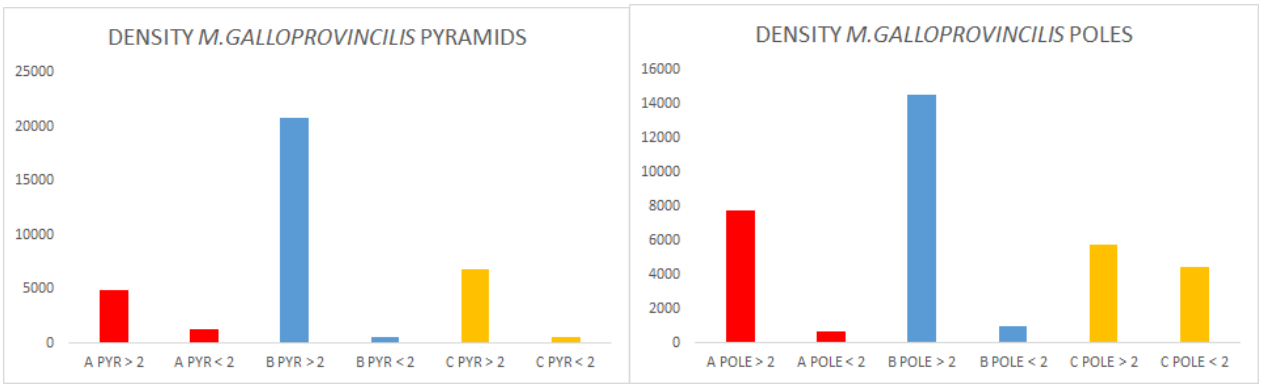

Figure 4.23 - Density of *M. galloprovincialis* (N. individuals / m^2) by structure typology, area and distance from the seafloor.

Table VII - Average size (SL) and weight of *M. galloprovincialis* with associated st. dev.; the data refer to the pyramids (a) and to the poles (b) at different distances from the seafloor in the different areas.

a)	**A PYR > 2m**	**A PYR < 2m**	**B PYR > 2m**	**B PYR < 2m**	**C PYR > 2m**	**C PYR < 2m**
AVERAGE SIZE (mm)	20.43±8.93	8.19±3.82	17.32±9.54	9.60±4.03	18.28±7.00	11.41±6.46
WEIGHT (Kg/m^2)	3.6	1.4	10.1	0.8	5.5	0.8
b)	**A POLE > 2**	**A POLE < 2**	**B POLE > 2**	**B POLE < 2**	**C POLE > 2**	**C POLE < 2**
AVERAGE SIZE (mm)	29.79±9.20	26.99±12.57	12.71±8.78	26.81±15.77	21.70±13.32	9.58±8.67
WEIGHT (Kg/m^2)	22.1	2.5	12.3	4.2	12.5	3.2

The distribution plots (Figures 4.24 and 4.25) show that the individuals with a commercial size (SL≥50mm) were completely absent on the pyramids, while on the poles they made up only 1.9% of the population. Given that these specimens were very abundant on the reef structures in 2019, it can be deduced that their absence was due to an indiscriminate harvesting by recreational and professional fishers between 2019 and 2020, hence the population found in June 2021 derived from a new settlement occurring between fall 2020 and late winter - spring 2021.

The average size of mussels settled on the substrates varied from 8.19±3.82cm (bottom block of the pyramids in A area) to 29.79±9.20cm (pole of A area, depth>2m) (Table VII). However, due to the high variability, a significant difference was only evidenced between the mussels settled on the bottom (depth>2m) and upper blocks (depth<2m) of the pyramids in A area (Tables 4.VIII and 4.IX).

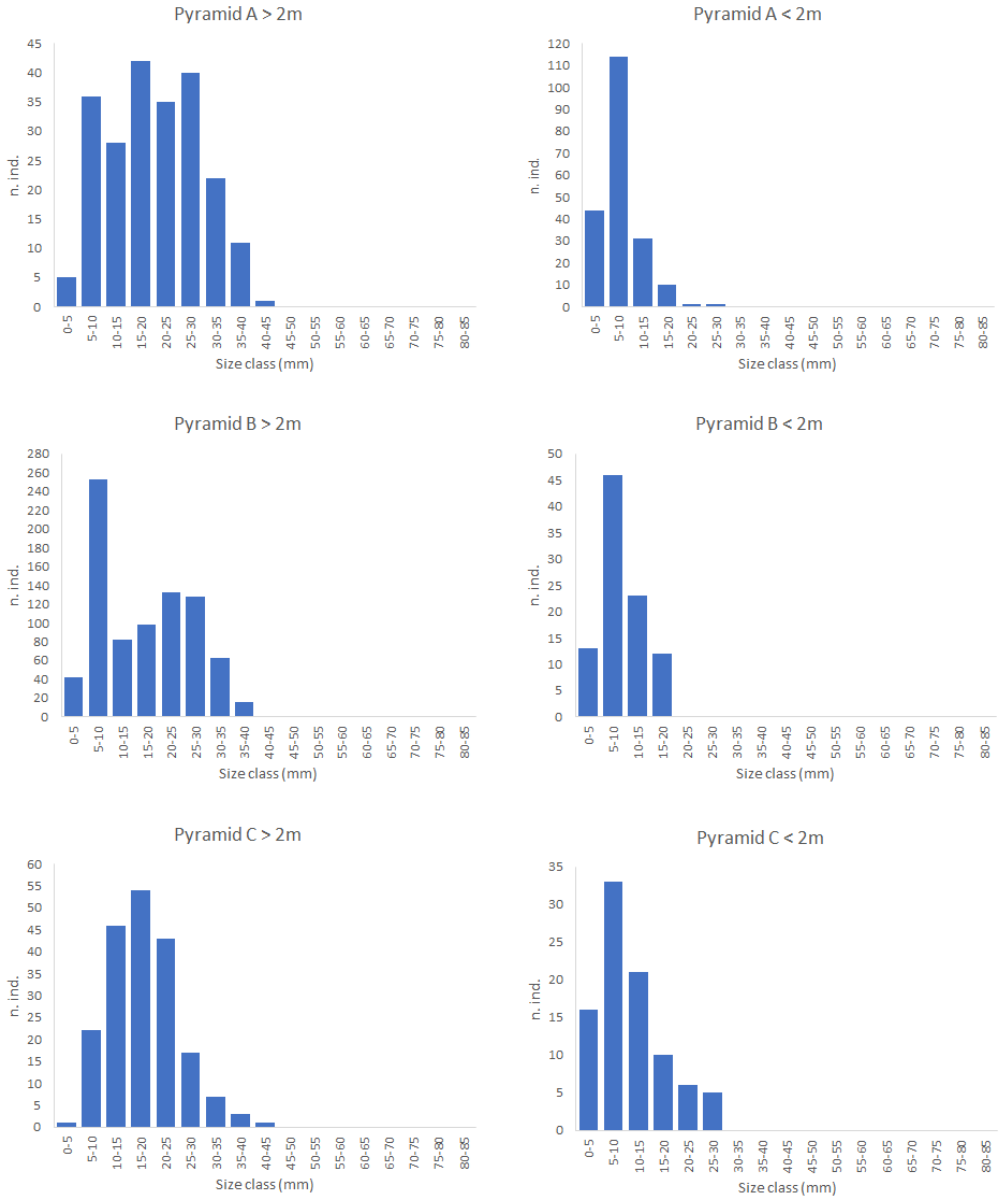

Figure 4.24 - Size-frequency distributions of *M. galloprovincialis* settled on the pyramids in the different areas and at different depths.

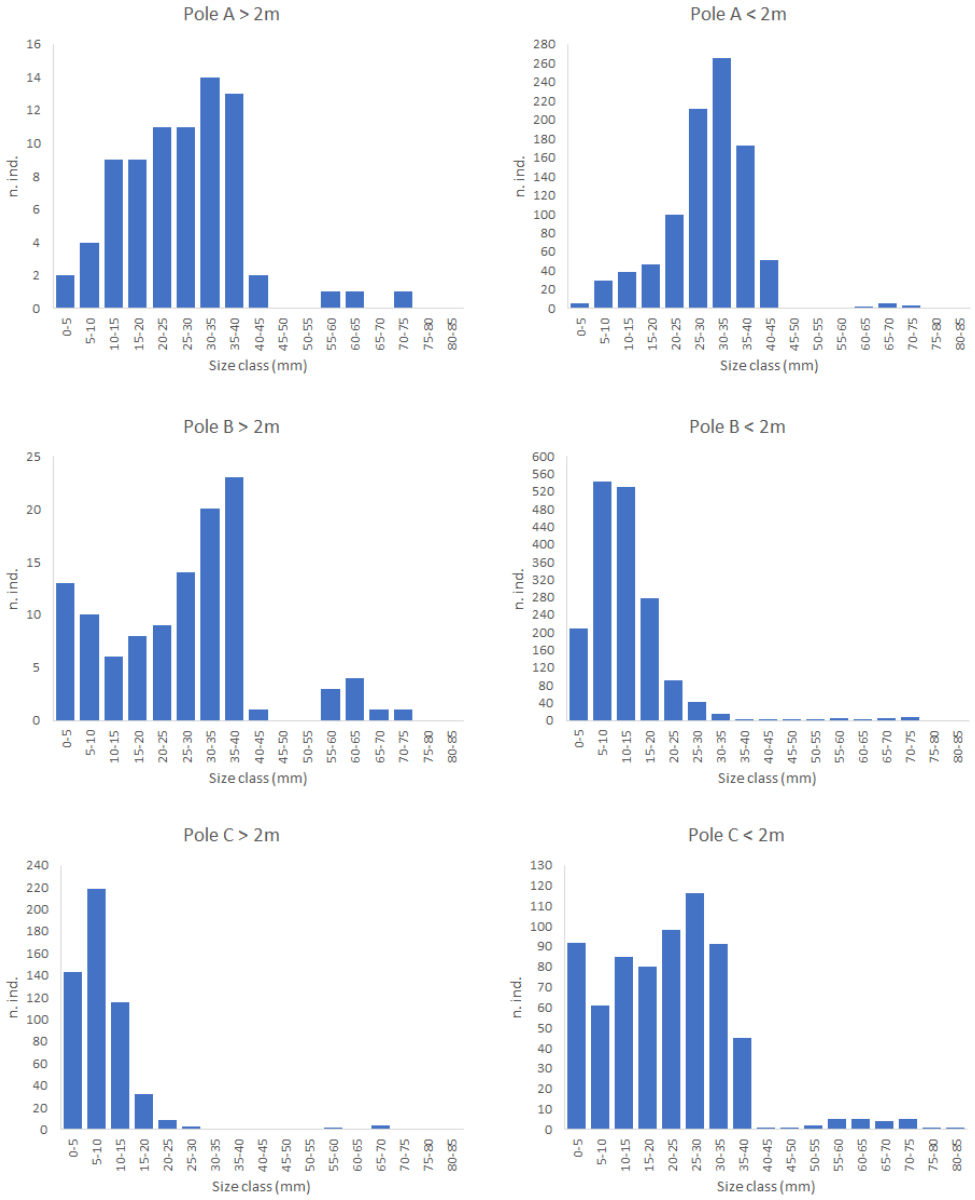

Figure 4.25 - Size-frequency distributions of *M. galloprovincialis* settled on the poles in the different areas and at different depths.

Table VIII - Statistical comparison (p.values) of the average size (SL) of mussels settled on the same structure at different depths in A,B, and C areas. Significant observations in bold

Depth	***Pyr A***	***Pyr B***	***Pyr C***
>2m*<2m	**0.003**	0.985	0.951
Depth	***Pole A***	***Pole B***	***Pole C***
>2m*<2m	0.993	0.988	0.984

Table IX - Statistical comparison (p.values) of the average size (SL) of mussels settled on the same typology of structure, at the same depth, in A, B, and C areas.

Area	***>2m***	***<2m***
*Pyr A *Pyr B*	*0.987*	*0.951*
*Pyr A *Pyr C*	*0.985*	*0.982*
*Pyr B *Pyr C*	*0.978*	*0.935*
*Pole A *Pole B*	*0.996*	*0.976*
*Pole A *Pole C*	*0.991*	*0.982*
*Pole B *Pole C*	*0.988*	*0.247*

With regards to the commercial production of the AR, based on the growth and mortality rates derived by previous studies (Fabi *et al*., 1989; Giulini and Maffei, 1994) it results that the mussels settled on the pyramids and poles will take around 8-9 months to reach the average size of 50mm SL with an estimated overall mortality of 50%, which leads to a final commercial biomass of 33.8 Kg/m^2 for the mussels settled on the pyramids and 33.0 Kg/m^2 on the poles.

4.4.2. Bioaccumulation of contaminants and harmful bacteria

In spring 2020 mussels showed only very low concentrations of heavy metals (Mercury, Arsenic, Cadmium and Lead) (Table 4.X). All the values appear below the legal limits.

In 2021, an increment of some contaminants was highlighted in respect to the previous year. In particular, the concentrations of Arsenic, Cadmium and Lead have doubled, even though only Lead, with 2.08±0.46 mg/kg d.s., has reached the legal limit reported in the EC Regulation 1881/06 (1.50 mg/kg) (Table 4.X). Some PCBs (i.e., PCB 028 + PCB 031, PCB 101, PCB 118, PCB 128, PCB 138, PCB 153, PCB 156, and PCB 180) have been also detected, but in low concentrations. In fact, the sum of PCBs (6.12±1.71 µg/Kg d.s.) remains much lower than the legal limit indicated in the EU Regulation 1259/11 (75 µg/Kg).

As in 2020, all the other chemical contaminants as well as the pathogenic micro-organisms appear not evaluable, indicating an excellent quality of the mussels settled on the artificial substrates in both years.

Table 4.X - Results of the analysis on chemical contaminants and pathogenic microorganisms in mussels carried out in 2020 and 2021. The legal limits have been also reported when available.

Parameter	Concentration 2020	Concentration 2021	Limit
Residual (105°C)	17.9±2.5%	3.1±0.1%	
Mercury	0.13±0.07 mg/Kg d.s.	0.11±0.06 mg/Kg d.s.	0.5 mg/Kg (1)
Arsenic	12.5±3.2 mg/Kg d.s.	22.5±5.7 mg/Kg d.s.	
Cadmium	0.50±0.31 mg/Kg d.s.	1.1±0.3 mg/Kg d.s.	1 mg/Kg (2)
Lead	1.06±0.24 mg/Kg d.s.	2.08±0.46 mg/Kg d.s.	1.50 mg/Kg (2)
PCB 028 + PCB 031	<0.1 µg/Kg d.s.	0.160±0.051 µg/Kg d.s.	
PCB 052	<0.1 µg/Kg d.s.	<0.1 µg/Kg d.s.	
PCB 077	<0.1 µg/Kg d.s.	<0.1 µg/Kg d.s.	
PCB 081	<0.1 µg/Kg d.s.	<0.1 µg/Kg d.s.	
PCB 101	<0.1 µg/Kg d.s.	0.872±0.209 µg/Kg d.s.	
PCB 118	<0.1 µg/Kg d.s.	0.575±0.098 µg/Kg d.s.	
PCB 126	<0.1 µg/Kg d.s.	<0.1 µg/Kg d.s.	
PCB 128	<0.1 µg/Kg d.s.	0.197±0.073 µg/Kg d.s.	
PCB 138	<0.1 µg/Kg d.s.	1.90±0.68 µg/Kg d.s.	
PCB 153	<0.1 µg/Kg d.s.	1.98±0.99 µg/Kg d.s.	
PCB 156	<0.1 µg/Kg d.s.	0.158±0.049 µg/Kg d.s.	
PCB 169	<0.1 µg/Kg d.s.	<0.1 µg/Kg d.s.	
PCB 180	<0.1 µg/Kg d.s.	0.2860.114 µg/Kg d.s.	
Sum of PCBs	<0.1 µg/Kg d.s.	6.12±1.71 µg/Kg d.s.	75 µg/Kg (3)
Acenaphthylene	<1 µg/Kg d.s.	<1 µg/Kg d.s.	
Benz(A)Anthracene	<1 µg/Kg d.s.	<1 µg/Kg d.s.	
Fluoranthene	<1 µg/Kg d.s.	<1 µg/Kg d.s.	
Naphthalene	<1 µg/Kg d.s.	<1 µg/Kg d.s.	
Anthracene	<1 µg/Kg d.s.	<1 µg/Kg d.s.	
Benzo(A)Pyrene	<1 µg/Kg d.s.	<1 µg/Kg d.s.	5.0 µg/Kg (2)
Benzo(B)Fluoranthene	<1 µg/Kg d.s.	<1 µg/Kg d.s.	
Benzo(K)Fluoranthene	<1 µg/Kg d.s.	<1 µg/Kg d.s.	
Benzo(G,H,I)Perylene	<1 µg/Kg d.s.	<1 µg/Kg d.s.	
Acenaphthene	<1 µg/Kg d.s.	<1 µg/Kg d.s.	
Fluorene	<1 µg/Kg d.s.	<1 µg/Kg d.s.	
Phenanthrene	<1 µg/Kg d.s.	<1 µg/Kg d.s.	
Pyrene	<1 µg/Kg d.s.	<1 µg/Kg d.s.	
Dibenz(A,H)Anthracene	<1 µg/Kg d.s.	<1 µg/Kg d.s.	
Chrysene	<1 µg/Kg d.s.	<1 µg/Kg d.s.	
Indeno(1,2,3-C,D)Pyrene	<1 µg/Kg d.s.	<1 µg/Kg d.s.	
Sum of PAH	<1 µg/Kg d.s.	<1 µg/Kg d.s.	30 µg/Kg (2)

Table 4.X - Continue.

Parameter	Concentration 2020	Concentration 2021	Limit
Amnesic Shellfish Poison (ASP)	<2 mg/Kg p.e.	<2 mg/Kg p.e.	20 mg/Kg (4)
Paralytic Shellfish Poison (PSP)	<200 µg STX Hleq/Kg	N.R.	800 µg/Kg (4)
Okadaic acid and total derivates	<60 µg OA eq./Kg	<20 µg OA eq./Kg	160 µg OA eq./Kg (4)
total Azaspiracids	<25 µg AZA eq./Kg	<8 µg AZA eq./Kg	160 µg AZA eq./Kg (4)
total Pectenotoxins	<40 µg PTX e.q./Kg		
total Yessotoxins	<0.20 mg YTX eq./Kg ed	<0.05 mg YTX eq./Kg ed	1 mg YTX eq./Kg ed (4)
Escherichia coli	0 CFU/100 gr	0 CFU/100 gr	1-10 CFU (5)
Intestinal Enterococci	0 CFU/100 gr	0 CFU/100 gr	

(1) EC Regulation 466/01
(2) EC Regulation 1881/06
(3) EU Regulation 1259/11 (The limit refers to the sum of PCB 28 + PCB 52 + PCB 101 + PCB 138 + PCB 153 + PCB 180)
(4) EC Regulation 853/04
(5) EC Regulation 2073/05

4.5. Fish assemblage

In total, 30 species were found during the whole sampling period and in overall sampling areas, among which 1 mollusc, 2 crustaceans and 27 fishes (Tab. 4.XI). Figure 4.26 shows the cumulative distribution of the mean species abundance by m^3, mediated over all the sampling area, season and sampling methodology. Eleven fish species accounted for 95% of the cumulative distribution, among which *Boops boops* (BOG) was by far the most abundant (65% of the cumulative distribution). Apart from BOG, other species falling in the 95% interval were *Trachurus trachurus* (HOM), Blenniidae (QAY, QAG, QAR , NUW), Sparidae (CTB, ANN, SBS, SBX) and *Serranus hepatus* (SRJ). Pelagic species had the largest variability, as suggested from the error bar, while the observation of other species remained more stable along the samplings.

It should be acknowledged that these data were obtained by merging ROV and SD observations, which comparability exploration was reported in the next section. Although our analysis highlights some differences between sampling methodologies, mostly for the number of individuals, the figures reported here are still useful to give insight on the study area assemblage dynamics over the study period. Evaluating the species distribution by type of structure and attraction code (Figure 4.27, as from Bombace *et al.*, 1994), permits to identify substantial differences between the species assemblages residing on poles, pyramids and transects. The pyramid hosts a large number of species (26), followed by poles (11) and transects (7). There were many species whose family was almost exclusively found on the pyramids, including the majority of Sparidae and species with hiding behavior such as Scorpaenidae and *Conger conger*.

Table 4.XI - List of the species encountered in the sampling area. Attraction code: AT=Attracted, P=Partially Attracted, NA=Not Attracted; Habitat: B=Benthic, NB=Nekto-Bentic, P=Pelagic.

#	Genus	Species	Family	Species code	Attraction code	Habitat	#	Genus	Species	Family	Species code	Attraction code	Habitat
1	*Maja*	*spp.*	Crustaceans	JCX	AT	B	16	*Oblada*	*melanura*	*Sparidae*	SBS	AT	NB
2	*Scyllarus*	*spp.*	Crustaceans	YLX	AT	B	17	*Sciaena*	*umbra*	*Sciaenidae*	CBM	AT	NB
3	*Sepia*	*officinalis*	*Sepidae*	CTC	NA	B	18	*Sparus*	*aurata*	*Sparidae*	SBG	AT	NB
4	*Blennius*	*spp.*	*Blennidae*	NUW	AT	B	19	*Spondyliosoma*	*cantharus*	*Sparidae*	BRB	AT	NB
5	*Conger*	*conger*	*Congridae*	COE	AT	B	20	*Symphodus*	*tinca*	*Labridae*	YFX	AT	NB
6	*Parablennius*	*gattoruggine*	*Blennidae*	QAG	AT	B	21	*Atherina*	*spp.*	*Atherinidae*	AVX	NA	NB
7	*Parablennius*	*tentacularis*	*Blennidae*	QAY	AT	B	22	*Diplodus*	*annularis*	*Sparidae*	ANN	PA	NB
8	*Parablennius*	*rouxii*	*Blennidae*	QAR	AT	B	23	*Lithognathus*	*mormyrus*	*Sparidae*	SSB	PA	NB
9	*Scorpaena*	*spp.*	*Scorpenidae*	RSE	AT	B	24	*Serranus*	*hepatus*	*Serranidae*	SRJ	PA	NB
10	*Chelidonichthys*	*lucerna*	*Triglidae*	GUU	NA	B	25	*Serranus*	*cabrilla*	*Serranidae*	CBR	PA	NB
11	*Mullus*	*barbatus*	*Mullidae*	MUT	NA	B	26	*Sparidae*	*spp.*	*Sparidae*	SBX	PA	NB
12	*Trachinus*	*spp.*	*Trachinidae*	WEX	NA	B	27	*Seriola*	*dumerili*	*Carangidae*	AMB	AT	P
13	*Gobius*	*niger*	*Gobidae*	GBN	PA	B	28	*Boops*	*boops*	*Small sparidae*	BOG	PA	P
14	*Diplodus*	*vulgaris*	*Sparidae*	CTB	AT	NB	29	*Spicara*	*spp.*	*Centracanthidae*	PIC	PA	P
15	*Diplodus*	*sargus*	*Sparidae*	SWA	AT	NB	30	*Trachurus*	*trachurus*	*Carangidae*	HOM	PA	P

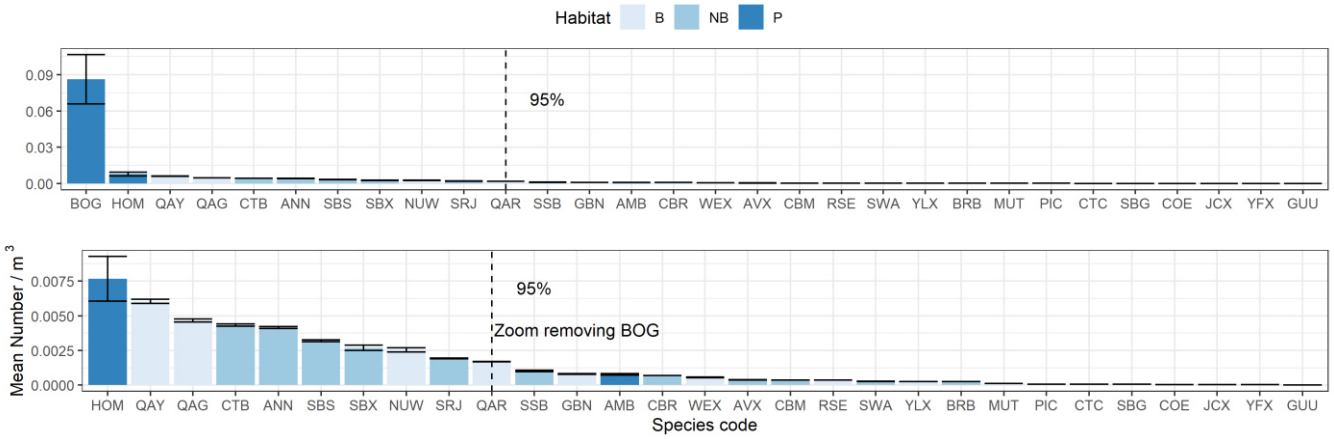

Figure 4.26 - Cumulative abundance by volume inspected of species encountered in the study area. In the lower panel is proposed the cumulative distribution removing BOG, the most abundant species. Colors represent habitat type: B = Benthic, NB = Nekto-Bentic, P = Pelagic.

On the contrary, strictly pelagic species, such as amberjack, were found exclusively around the poles. Blennidae were also more abundant on poles than on pyramids. Regarding attraction for hard structures, the large majority of observed individuals fell within the categories “Attracted” or “Partially attracted”, while the category “Non attracted” was found sporadically. Focusing on the scales, it is evident how low were occurrences on the transects.

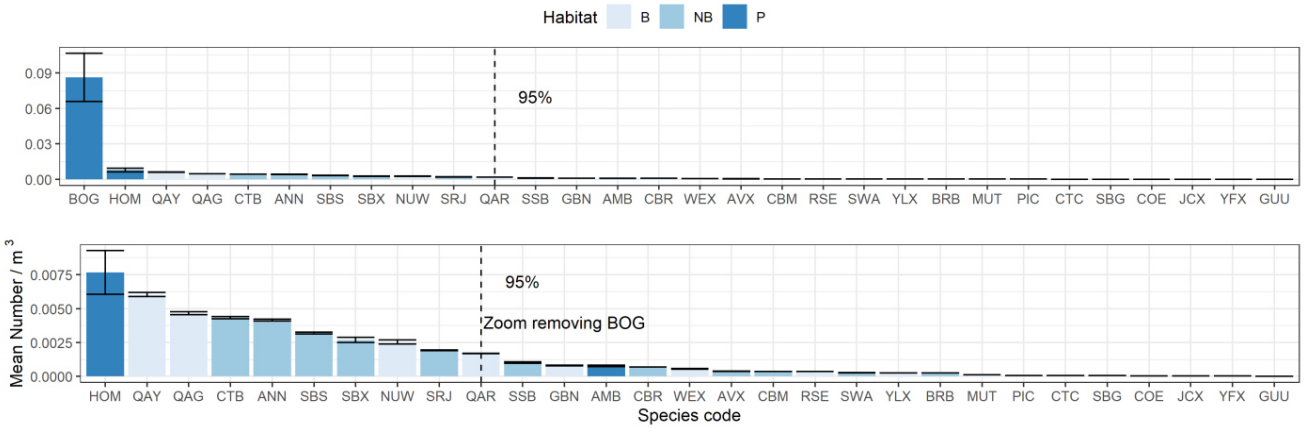

Figure 4.27 - Cumulative abundance by volume inspected (n. individuals/m3) of species encountered in the study area, divided by structure. Colors represent Attraction code: AT=Attracted, PA= Partially Attracted, NA=Not Attracted. PA = poles, PY = pyramids, TR = transects.

Figure 4.28 provides a further exploration of species distribution, with family abundance by month and structure. From this chart it is possible to understand that the population on pyramids was stable, and the majority of families were encountered, although in variable amounts, in almost every sampling. It is worth mentioning the Sparidae family, exclusively resident on pyramids and found during every sampling. On the contrary, poles were not hosting a stable population and they were empty during the colder months. A good example of pole dynamics is the family of small Sparidae (constituted by *B. boops*), which occurs in the reef seasonally, appearing in late spring and leaving in late fall. Blenniidae population was more stable, it was always encountered on pyramids and was present on poles from spring to late fall. Finally, the majority of sampling on transects registered 0 observations, confirming the findings of Figure 4.27 that the population encountered in the sampling area was mostly attracted by hard substrata.

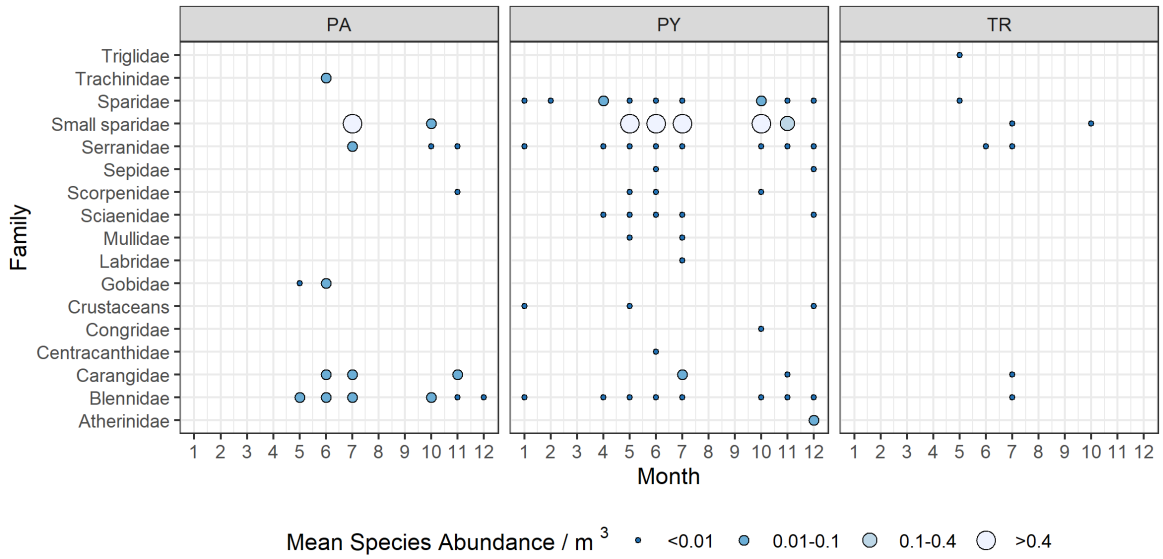

Figure 4.28 - Abundance by volume inspected (n. individuals/m3) of families encountered in the study area, divided by structure and month. Colors and size represent the abundance values. PA = poles, PY = pyramids, TR = transects.

Data collected during May 2021 permitted to compare the results obtained by the two methodologies. For this purpose, two sets of the indicators Sr, H and N were calculated for each area and structure (Figure 4.29) and statistically compared (Table 4.XII). A visual inspection showed that the factor structure was predominant in influencing each of the indicators. The two methodologies showed the largest differences in terms of number of individuals, with the SD recording largest numbers. On the contrary, for Sr the situation was more heterogeneous: the ROV detected in pyramids of each area a higher number of species, while on the poles this was not true. H indicator was a combination of Sr and N, therefore the observations on the pyramids were balanced by the errors of the two methods. The three way permutational-ANOVA highlighted different results for the indicators inspected, confirming some of our qualitative observations. Sr was the most homogeneous, and only the interaction between all the factors and the factor structure resulted in a significant effect on the indicator. H indicator was affected by all factors investigated except for the method, while N results were affected by each factor and combination of factors.

Based on these results, only Sr and H were selected for the GLMM modelling. In addition, the fact that structure resulted in affecting each of the indicators drove us to restrict the modelling on the pyramids, in order to reduce the number of variability sources in the analysis. For the H indicator it was selected as an inverse gaussian family for the GLMM. The model (Figure 4.30) indicated a slight significance for the fixed effect, the method, with a p.value of 0.034. Model diagnostics highlighted some pattern in the residuals distribution and a slight departure from normality. For the Sr indicator, the data distribution suggested adopting a normal distribution family for the modelling, therefore a linear mixed effect model (LME). LME

differs from GLMM for the distribution observed in the data. The model (Figure 4.31) highlighted a significant effect of the factor method, with a p.value <0.0001. Residual distribution did not show evident patterns, while the normality of the residual was not verified. This evidence discouraged us from merging indicators for statistical analysis. Further analysis is needed to identify the sources of differences.

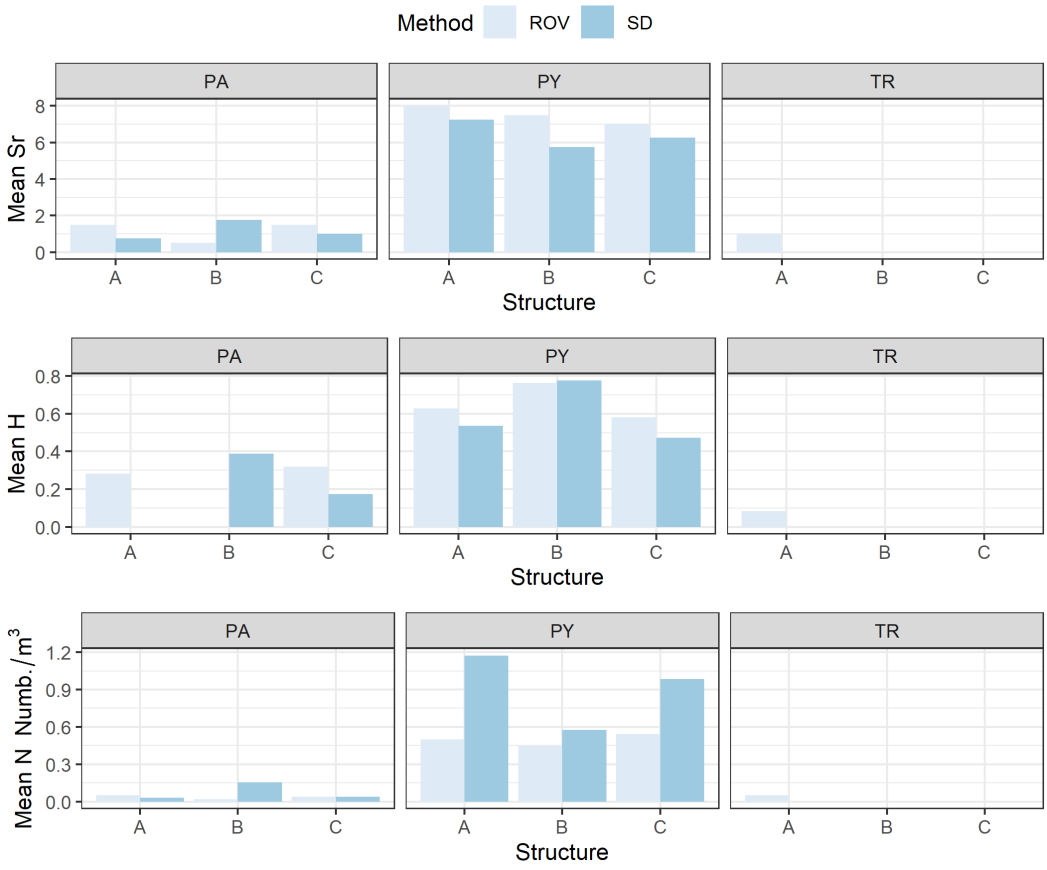

Figure 4.29 - Indicators calculated for the two sampling methods (ROV and SD) by structure and area. PY = pyramids, PA = poles, TR = transects.

Table 4.XII - Results of the three way permutational-ANOVA. Values are p.values, significant observations in bold.

Factor	*Sr*	*H*	*N*
Method	1	1	**<0.0001**
Structure	**<0.0001**	**<0.0001**	**<0.0001**
Area	1	**0.0004**	**<0.0001**
Method*Structure	1	**<0.0001**	**<0.0001**
Method*Area	1	**<0.0001**	**<0.0001**
Structure*Area	0.0566	**<0.0001**	**<0.0001**
Method*Structure*Area	**<0.0001**	**<0.0001**	**<0.0001**

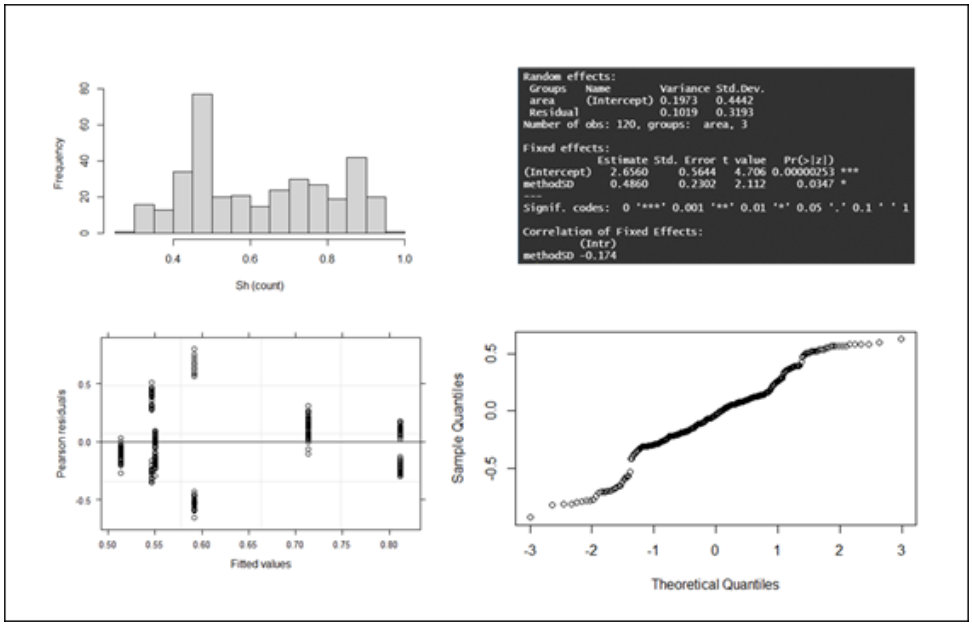

Figure 4.30 - GLMM model results for H indicator. Upper left: data distribution; upper right: model summary; lower left: residuals distribution; lower right: residuals qqplot for normality inspection.

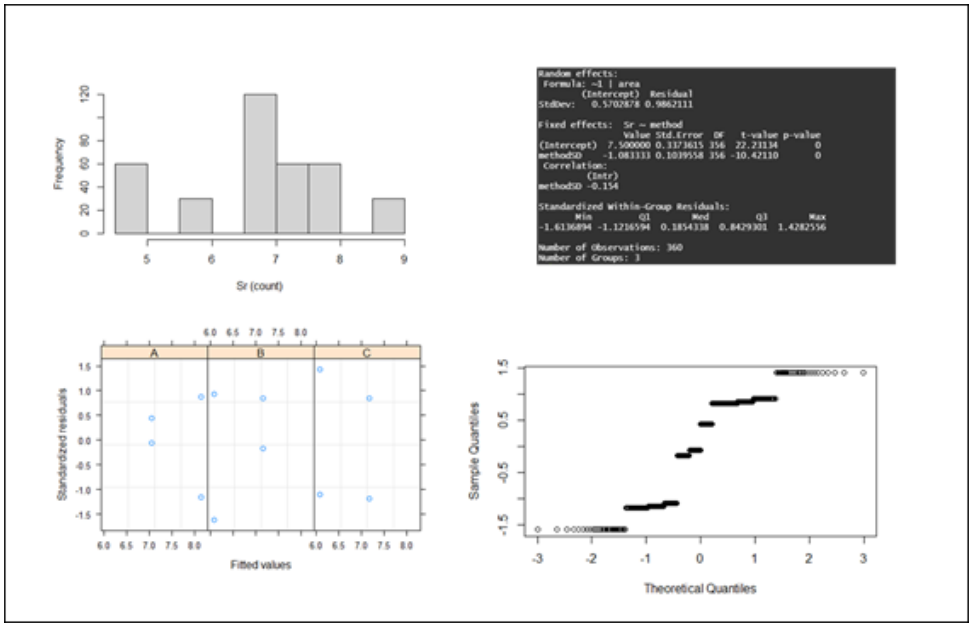

Figure 4.31 - LME model results for Sr indicator. Upper left: data distribution; upper right: model summary; lower left: residuals distribution; lower right: residuals qqplot for normality inspection.

Nevertheless, basing on the relatively low effect of the method on the H indicator, this was merged and plotted for a qualitative inspection (Figure 4.32). It resulted that, for pyramids, a peak is observed in spring and fall, counterbalanced by the poles having a single peak in the summer. The transect trend remained almost flat over the period. This dynamic may be, at least partially, explained by the observation of transient species such as *B. boops* and *T. trachurus*, which increased the diversity on the poles during the summer. On the contrary, the large number of *B. boops* on the pyramid had the effect of lowering the indicator value for this structure.

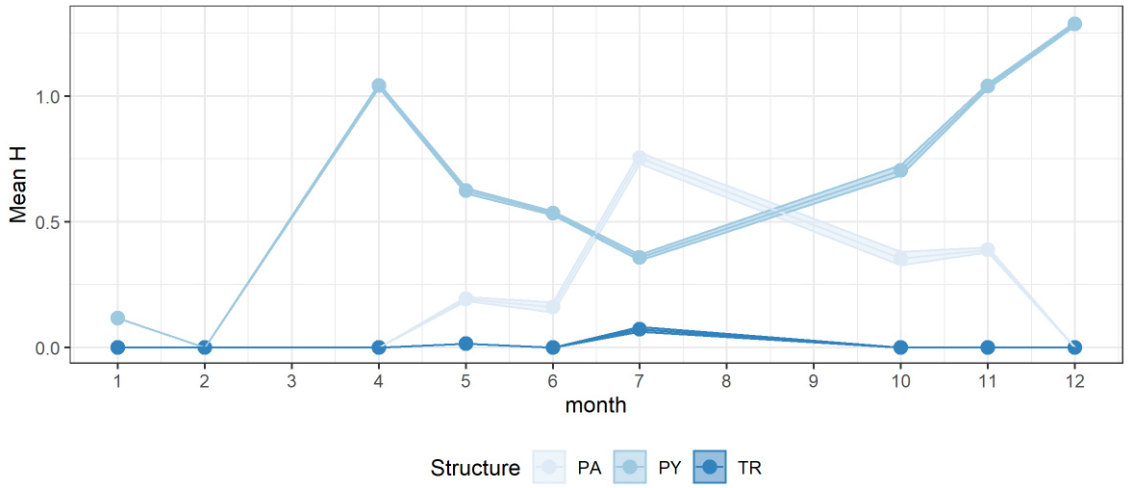

Figure 4.32 - H trend by month and structure based on the combined data from SD and ROV. Ribbons represent the standard error.

Following the evidence on the differences between samples retrieved with the two different methodologies, the statistical analysis on indicators was conducted separately. These statistics were based on permutational ANOVA, due to the absence of normality and heteroscedasticity in the data (data not shown). It was aimed to detect the effect of the season, of the area, and of the structure, which were used as factors.

Indicators calculated on SD data covered the warm part of the year, from spring to fall (Figure 4.33 and Table 4.XIII). The Sr remained stable on the pyramids during the seasons, while it peaked in summer for the poles. P.values confirmed this dynamic, highlighting a significant effect only for the Structure factor, and for the interaction between Structure and season. H indicator, as already indicated by Figure 4.32, was more oscillating and had opposite dynamics in poles and pyramids. In particular, in summer H peaked in the poles, while it had the lowest value on the pyramids. P.values confirmed this observation, highlighting significant effects for both season and structure factors, as well as for their interactions. The biomass in pyramids peaked in spring and then it declined steadily, while on the poles it peaked in summer. An exception was observed in area C, where in fall there was a school of amberjacks causing a very high value compared to other areas. Statistics highlighted significant effects for structure and season and their interactions. Lastly, DP calculated on the observations of the two divers was more stable along the seasons while it was heterogeneous for both structure and area, confirmed by the p.values that highlighted significant effects for all factors and their interactions, except for the season.

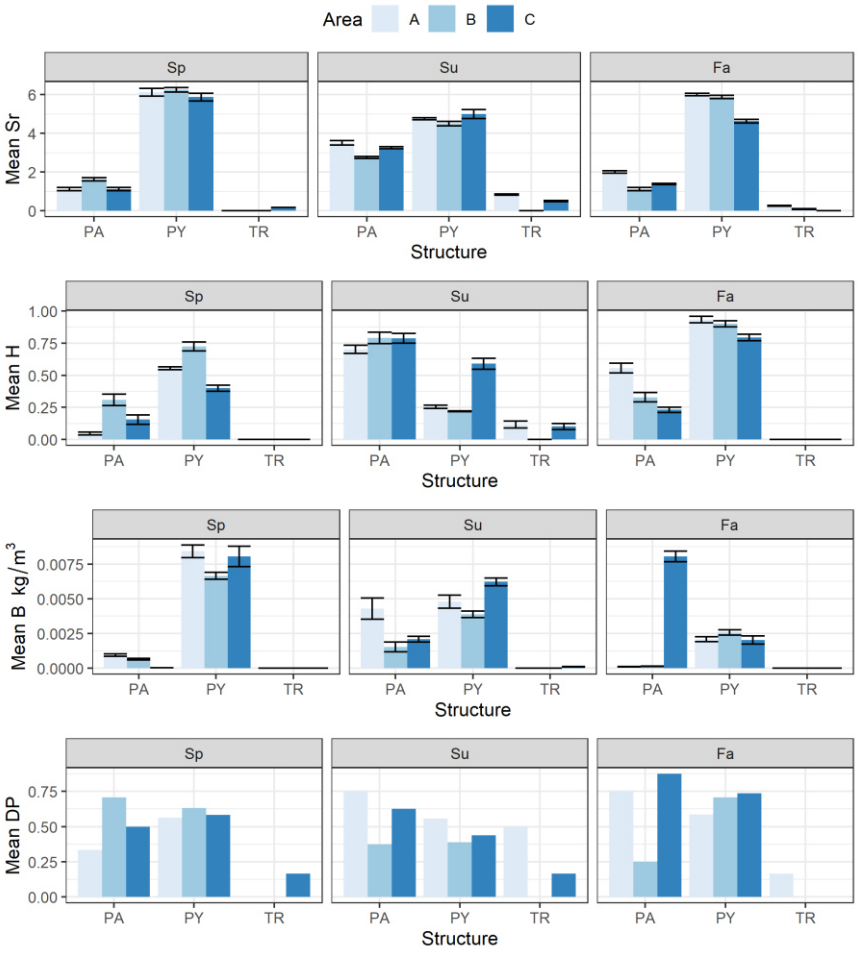

Figure 4.33 - Indicators from SD data. Sp = spring, Su = summer, Fa = fall, PA = pole, P Y= pyramid, TR = transect.

Table 4.XIII - Three-way permutational ANOVA p.values for Indicators from SD data. Significant observations in bold.

Factor	***Sr***	***H***	***B***	***Dp***
Season	0.0391	**< 0.0001**	**< 0.0001**	0.1502
Structure	**< 0.0001**	**< 0.0001**	**< 0.0001**	**< 0.0001**
Area	0.0423	1	0.0632	**0.0006**
Season*Structure	**< 0.0001**	**< 0.0001**	**< 0.0001**	**0.0001**
Season*Area	0.2189	**< 0.0001**	**0.0127**	**< 0.0001**
Structure*Area	0.9925	1	0.0969	**0.0001**
Season*Structure*Area	**0.1608**	**0.0004**	0.0318	**< 0.0001**

Indicators calculated on ROV data covered the colder part of the year, from fall to spring (Figure 4.34 and Table 4.XIV). The Sr remained stable on the pyramids in summer and fall, while it dropped in winter. For the poles it remained quite low along the seasons. P.values confirmed this dynamic, highlighting a significant effect for the Structure and the season factor, and for the interaction between Structure and season. H indicator, as already indicated by Figure 4.32, had high values on pyramids in spring and fall, while it dropped in winter. Similarly to Sr, also H remained always quite low on the poles. P.values confirmed this observation, for the Structure and the season factor, and for the interaction between Structure and season. The number of individuals in pyramids peaked in spring and then it declined steadily, while on the poles it never peaked. This observation is not surprising, since the ROV did not sample in summer, where it was observed from SD that poles registered a high number of *B. boops*. Statistics highlighted significant effects for structure and season and their interactions. Lastly, DP calculated on the observations of the two divers (combined and averaged) against the ROV was calculated only for the sampling of June 2021. The Detection probability was large on the pyramids, with values in line (or even higher) with the comparison between the two divers. On the contrary, DP was quite low for the poles, with the exception of one area. Although no statistic was conducted on this indicator, these results show that ROV and SD are quite comparable in terms of number of species detected on the pyramids, while one method (ROV, author observation) fails to sample poles properly.

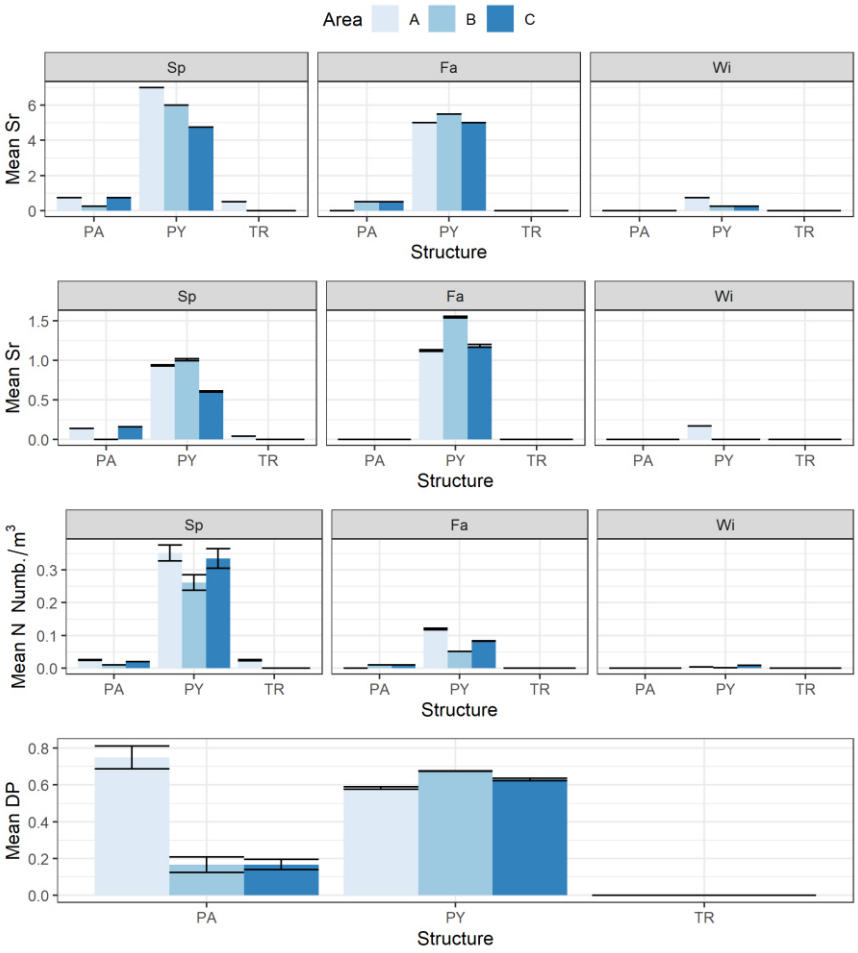

Figure 4.34 - Indicators from ROV data. Sp = spring, Su = summer, Fa = fall, PA = pole, P Y= pyramid, TR = transect.

Table 4.XIV -Three-way permutational ANOVA p.values for Indicators from ROV Significant observations in bold.

Factor	***Sr***	***H***	***B***
Season	**< 0.0001**	**< 0.0001**	**< 0.0001**
Structure	**< 0.0001**	**< 0.0001**	**< 0.0001**
Area	1	1	1
Season*Structure	**< 0.0001**	**< 0.0001**	**< 0.0001**
Season*Area	1	1	1
Structure*Area	1	1	1
Season*Structure*Area	1	1	1

The last analysis was the multivariate comparison of fish assemblages detected with the two sampling methods. The graphic inspection of the matrix of distances between the species assemblages (nMDS, Figure 4.35) added further elements to the hypothesis already emerged from the previous analysis. In particular, some of the observations mostly contributing to dissimilarity were the Blenniidae species on poles, which were very difficult to identify from ROV observations. Other observations were relative to the *B. boops* observations on pyramids, which mostly differed by the amount of individuals counted (author observation). A clear outlier was the observation of *Lythognathus mormyrus* on the transect, which was exclusively seen by the ROV. The anosim statistic (Table 4.XV) confirmed that both structure and species factors were statistically affecting the fish assemblage observations. The Simper analysis (only conducted on the factor species, Figure 4.36) also confirmed our speculation, individuating BOG (*B. boops*), QAY (*Parablennius tentacularis*) and SSB (*L. mormyrus*) as the three species most contributing to the dissimilarity (68%). All the other species included in the 95% of dissimilarities were Sparidae or Blenniidae.

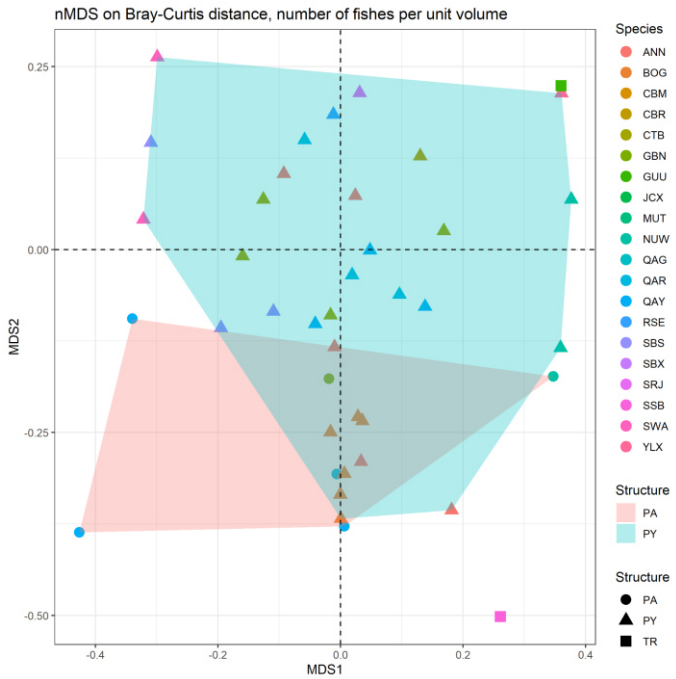

Figure 4.35 - nMDS calculated on Bray-Curtis matrix of dissimilarities between species assemblages from ROV and SD. PA=pole; PY=pyramid; TR=transect.

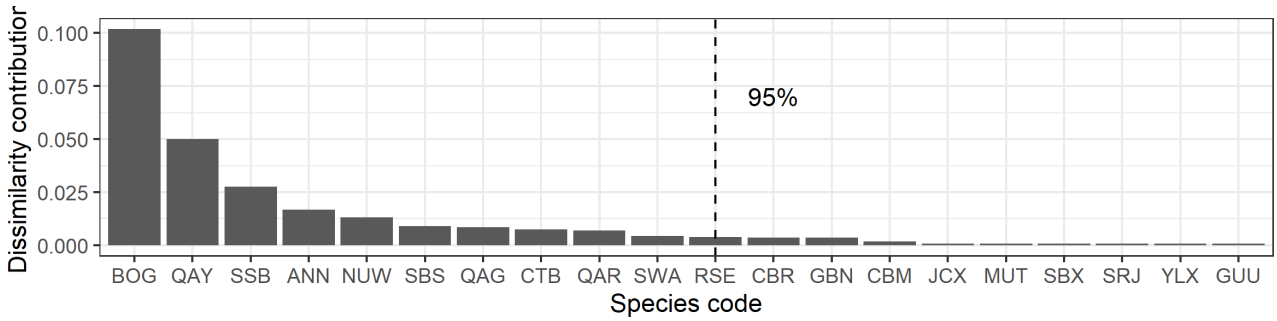

Figure 4.36 - Species contribution to dissimilarities, as from Simper analysis.

Table 4.XV - R statistic and p.values from anosim analysis.

Factor	***R***	***P-value***
Structure	0.233	**0.002**
Species	0.357	**0.001**

Results listed in the previous pages may be divided into two main arguments: the comparison between sampling methodology and the population dynamic in the study area along the sampling period. Regarding the comparison between the sampling methodology, it emerges that data collected were not strictly comparable because of different reasons: at one hand, the ROV showed to be less accurate on the poles, where it was not always able to detect all the species richness, while on the other hand the number of individuals of the same species, especially for schooling species, were not equally estimated. Speaking on the experience in the footage viewed, from ROV samples it was sometimes difficult to identify the Blenniidae species, which were most of the time called Blenniidae spp. thus reducing the number of species encountered. This observation was confirmed by the Simper analysis, where *P. tentacularis* was one of the species contributing most to the differences. On the pyramids the ROV was very accurate, and on average it permitted the identification of a higher number of species compared to SD. In particular, only the ROV enabled observation of some cryptic species (such as *Scyllarus* spp.; Figure 4.37). What resulted in contributing most to the differences on the pyramids was the number of individuals observed for those schooling species, such as *B. boops*. In this case, the ROV footage permitted to count quite accurately the number of individuals, resulting in a more accurate estimation and highlighting how SD observations were overestimated. To this evidence, it is possible to add that in videos not included in this analysis, where low visibility was encountered, it was difficult to distinguish between Sparidae species from the ROV videos. Summing up, the diversity of the pyramid was adequately sampled by both methodologies, and the sources of differences may be explained by some specific cases. On the contrary, the poles' diversity was more difficult to sample from the ROV, and this may be due to the shape of the structure and to the behaviour of

the species, which frequently hide between the mussels. Additional work is needed to extend the comparison here presented at species level, thus enabling the merging of the observations and to provide more insight on the annual dynamic of the study area.

Regarding the population dynamic of the study area, analysis has shown that on the pyramids there are some species (Sparidae, Blenniidae and Serranidae) whose population is stable throughout the year, stressing the importance of the habitat and ecosystem function provided by this kind of structure. The same dynamic was not observed on the poles, which in the colder months of the year were empty of fish. The amount of species, as well as their numerosity, rose ubiquitously in spring. Small pelagic and nekto-benthic species such as *B. boops* and *T. trachurus* were observed only in the warmer part of the year, especially *B. boops* that were sampled in large quantities during summer. Nevertheless, there were other species exclusively sampled during the warm season, such as Mullidae and Labridae. On the contrary, there were just a few species observed exclusively during the cold season: those were Atherinidae*, C. conger* and *Scyllarus* spp. For the two latter species, their cryptic behaviour may have caused some false negative samples. Especially for Scyllaridae, the SD were never able to sample this species. The increase of diversity observed during summer may be linked to the general ontogenetic migrations observed for Adriatic species (Vrgoč *et al.*, 2004), which typically reside in the deeper areas during winter and move coastward during summer. In addition to this dynamic, the hard substrata in the study area during the warm months get covered with mussels (see Chapter 4.4.1) and this potentially offers an additional attractivity for other trophic levels. Further analysis may be required to understand the link between mussels abundance and species abundance.

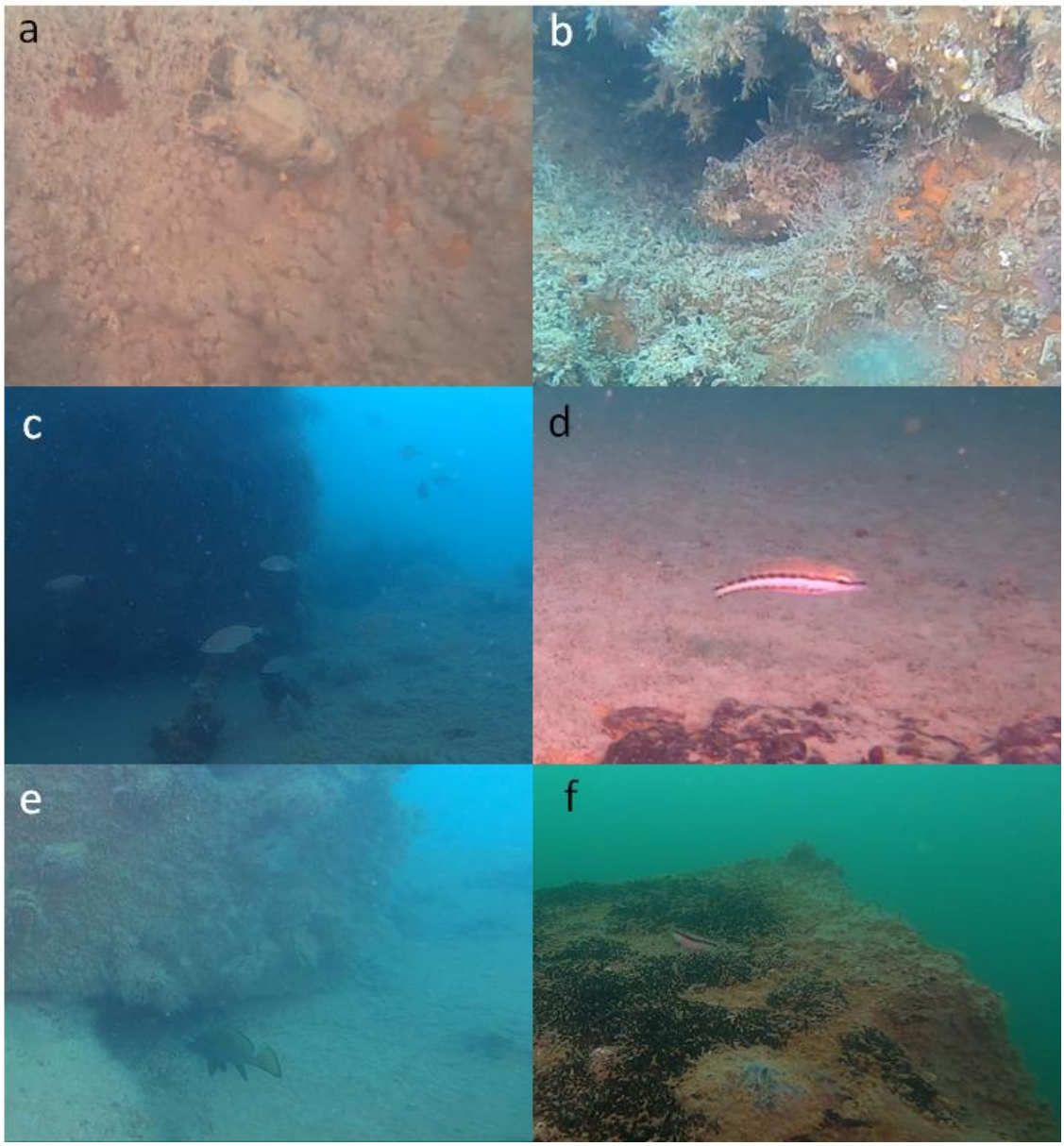

Figure 4.37a - Some photographs from ROV footage. a: *Scyllarus* spp., b: *Scorpaena spp.* c: Sparidae (*Diplodus annularis* and *Oblada melanura* in forefront), d: *Serranus cabrilla*; e: *Sciaena umbra*; f: *Parablennius rouxi.*

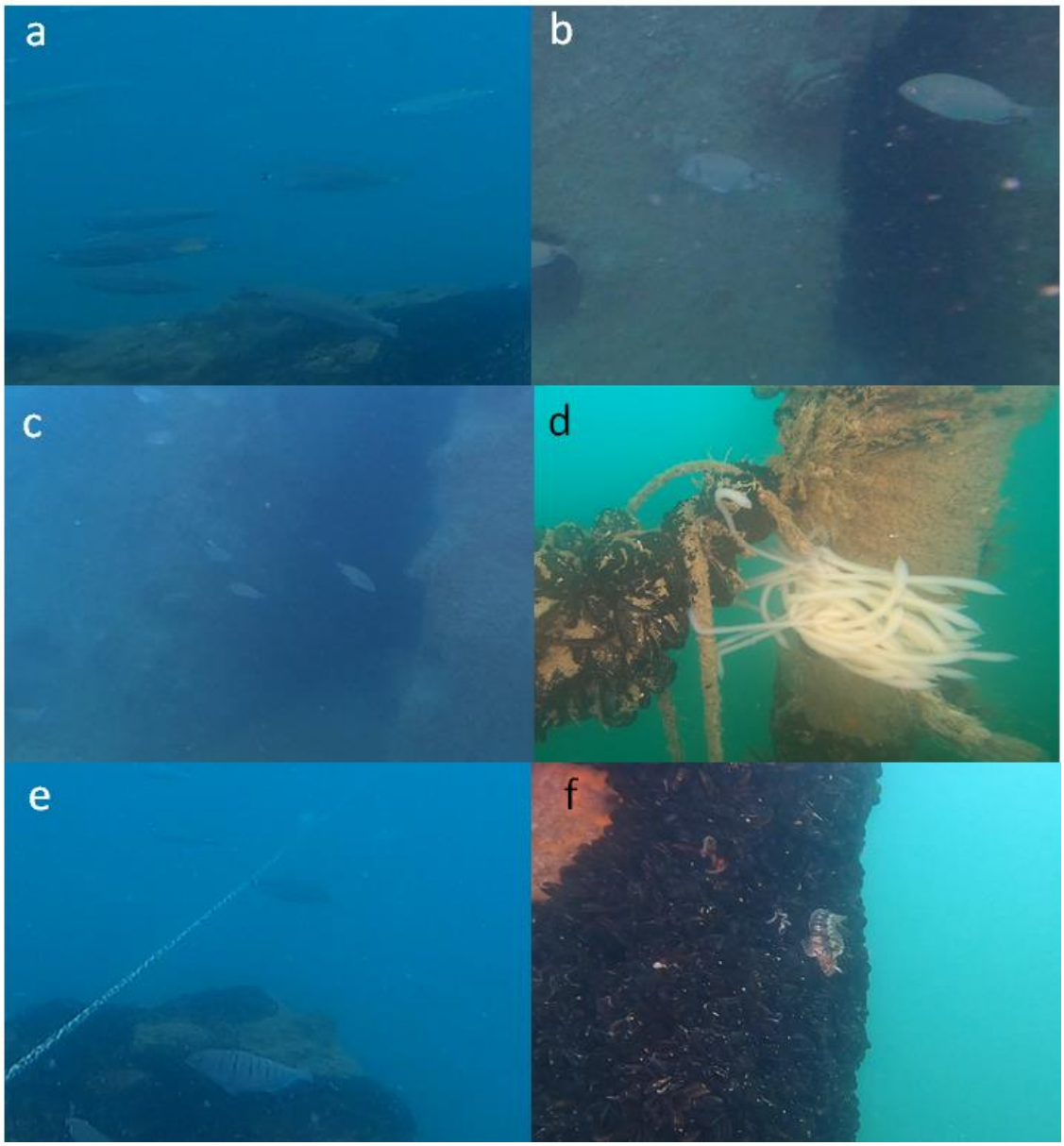

Figure 4.37b - Some photographs from ROV footage. a: *Boops boops*, b: Sparidae (*Diplodus annularis* and *Diplodus vulgaris*), c: Sparidae, d: eggs of Loliginidae *(*not reported in the data*)*, e: *Lythognathus mormyrus*, f: *Parablennius gattoruggine*

4.6. 3D reconstruction model

The availability of camera-added frame measurement and the rope imposed in the scene allowed for a comparison with the final 3D model obtained with the photogrammetric approach. It has to be mentioned, however, that the resolution of the rope is of the order of 1 sample every about 0.5m, over a large face area, while the resolution of the photogrammetric data is approximately 1 sample every 0.01m over a much smaller area. It was not possible to determine the discrepancy of the merged data in XY as the plane is flat in this zone. This will be estimated from the absolute accuracy of the measurement techniques in the future.

As the last step, using the knowledge of the pyramid mathematical configuration and measurement it was possible to add the 3D reconstructed model to the cube skeleton. Figure 4.38 reports an example of the possibilities of the algorithm simulating the final results and stitching some 3D faces on a synthetic cube. This aspect has to be improved in the future.

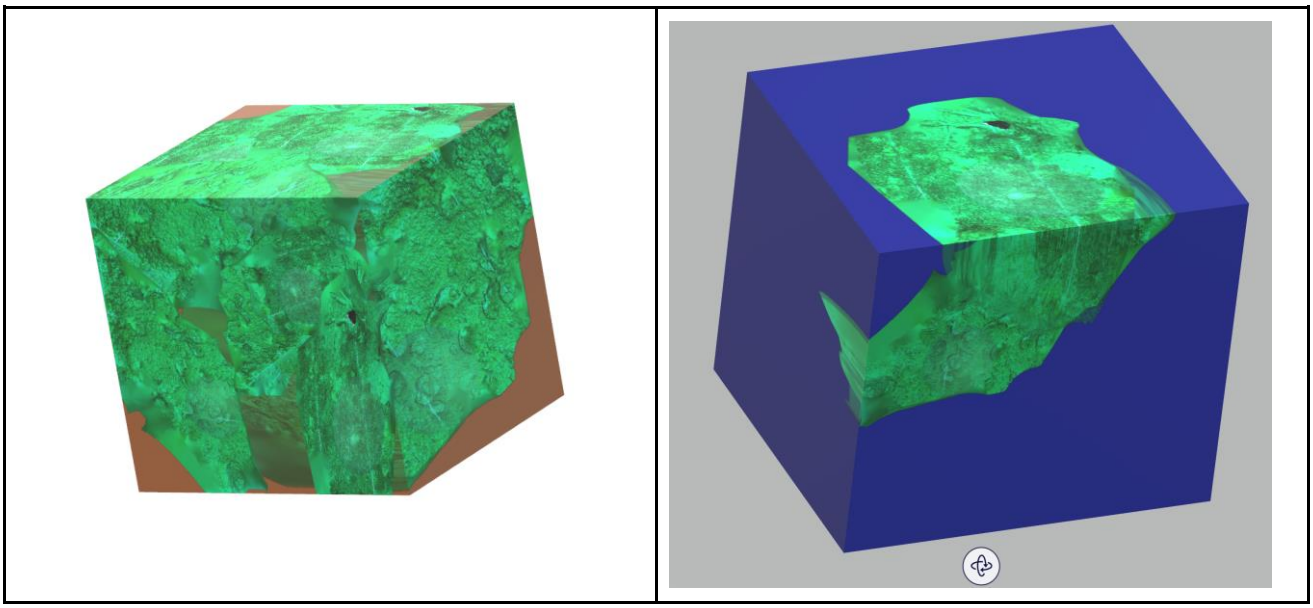

Figure 4.38 - Part of the 3D faces stitched into a virtual cube mathematically (https://univpm-my.sharepoint.com/:f:/g/personal/p004291_staff_univpm_it/EiykKTyinZtNoi-1O5KjqsQBUC_EtZJ34kG1eDu61RXsmw?e=VYs7fw).

5. CONCLUSION

The Porto Recanati - Porto Potenza Picena artificial reef, located in the coastal waters of the Marche region (central Adriatic Sea) approximately 10 km South of the Conero Promontory, at 13.5 m of depth, was chosen as a Case study within the Adrireef project as it can be considered as representative of the several artificial reefs deployed along the Italian coast of the central-northern Adriatic sea.

The reef, realized around 20 years ago with the aims of finfish repopulation and protection of the coastal grounds from illegal trawling, was monitored over five years after deployment, which allowed to study the first steps of the colonization processes by benthic and mobile organisms. Since its construction, the reef area has been interdicted to every human activity however, no measures or controls aimed at limiting access have been ever put in place and, as a matter of fact, it has been subjected to any kind of exploitation.

The multidisciplinary monitoring approach implemented within the Adrireef project has thus allowed to get an overview of the reef once it has reached its ecological equilibrium, to collect useful information for identifying the potential vocation of the area in terms of ecosystem functions and services, and to improve management policies. Obviously, further studies would be needed to better understand how sensitive, stable, or resilient the reef of Porto Recanati - Porto Potenza is, in order to optimize its usage by the potential stakeholders and accordingly adapt management measures.

The monitoring was conducted using innovative, non-invasive and integrated technologies some of which specifically developed or adapted with the goal of automatizing as much as possible the data collection to allow sampling all the overall year round and reduce field work both on vessels and underwater. Although restrictions and difficulties linked to the Covid pandemic did not allow to finalize some of them, the basic developments have been set up, making it possible to collect sufficient data for the scope of this work. Nevertheless, the work will continue for further optimization.

Specifically, the outcomes of the MBES surveys suggest how a multibeam echosounder, if foreseen in a systematic monitoring program, might be key in drawing post-reef deployment comparisons and gaining a mechanistic and predictive understanding of how the reef functions ecologically and physically during its life.

The set up of the oceanographic buoy system for the continuous monitoring of some relevant physical and chemical parameters along the water columns with the associated applications to transfer the data in real-time and make them easily accessible to the wide public has proved to be extremely useful either to get a full understanding of the hydrodynamics of the area, and to plan other monitoring activities such as UVC and photographic sampling of the benthic communities settled on the pyramids. The dissemination of the data through dedicated free-accessible dashboards has also allowed other users (e.g., divers, recreational and professional fishers, sailors) to adequately plan in advance their own activities. A further development could be the implementation of the system with supplementary sensors to measure, for example, the turbidity just close to the seafloor and the fundamental wave parameters.

Also the photographic sampling has proved to be an effective sampling method to study the benthic communities settled on the artificial substrates. In fact, even though the identification at species level was only possible for a few taxa, it provided a satisfactory quali-quantitative picture of the assemblage which colonizes the structures.

With regards to the UVC conducted with ROV, this technique was very accurate on the pyramids where it permitted the identification of a higher number of species compared to the scuba divers. In particular, only the ROV enabled observation of some cryptic species (e.g., *Scyllarus* spp.) and allowed a more accurate count of the individuals of pelagic schooling species such as *Boops boops*. On the contrary, the poles' diversity was more difficult to sample through the ROV, and this may be due to the shape of the structure and to the behaviour of the species, which frequently hide among the mussels. Additional work is however needed to optimize the data collection technique and software which would enable the automatic identification of the species and the estimation of specimens' size.

Finally, the assessment of the biomass of mussels settled on the artificial substrates was the only activity carried out through the traditional methodology of “scraping”, due to the impossibility of obtaining a sufficient photographic set of suitable quality to be used for the application of photogrammetry as initially planned. The difficulties were mainly due to frequent poor visibility close to the seafloor, which enables us to take a suitable number of pictures of the lower parts of the structures as well as to get wide overviews of the overall modules, and the relatively thin layer of mussels settled on the substrates which made it difficult to estimate the thickness of the mussel coverage. To overcome these problems, a cooperation has been initiated with the Università Politecnica delle Marche (Ancona, Italy) which has led to experiment a new methodology based on merging advanced methods and techniques of data acquisition through SD, to compensate the visibility problems and document the environment point by point and merging the entire area by means of a large acoustic map. The applied approach was thought to pursue the design of a general methodology that can be finalized in the future for this area and similar ones. A final model of the entire AR obtained with the adopted strategy, in future, can be made accessible online, both as an example of digital temporal evolution and for demonstrating new facilities of exploration in a safe, cost-effective and pedagogical environment. The virtual underwater AR can provide biologists with an improved insight into the data, the natural components, and the general public with simulated dives to the site.

With regards to results obtained from the monitoring activities implemented in the framework of the project, the MBES surveys enabled the characterization of the AR in terms of compliance with the original drawing and structural integrity. The displacement of structures was quite in line with the original plan that placed 252 2-layer pyramids following a 60 x 60 m grid and 506 poles among the pyramids to give a structural continuity and increase the ecological functionality of the reef. However, in 2018 most of the concrete poles were found to have collapsed, with only 24 of them still undamaged, showing how that type of structure is not sufficiently stable to be used for artificial reef construction. Conversely, the pyramids were mostly intact,

even though slight scour signatures occurred at the sides of their concrete bases followed by banks of removed substrate.

The mean depth of the ambient seafloor was 13.5 m, with a deepening of the whole AR area in the northern part, where the mean depth reached 14.00 m.

The comparison of the survey conducted in 2020 with the preliminary one carried out in 2018 showed barely visible areas of deposition and erosion processes between the two surveys, likely due to local resuspension and river sediment transport, and the collapse of two pyramids. No additional significant collapses were observed, while some smaller vertical/horizontal movements of the single units had kept on occurring and scour signatures had been depicted, according to the measures of the local currents.

The explorative MBES survey was also useful for planning subsequent investigations such as the continuous water monitoring, by identifying the best location for the oceanographic buoy and the UVC for the assessment of the fish assemblage, by selecting 3 suitable sub-areas, one in the North, one in the center, and the other one in the South of the AR, which were comparable in terms of structures involved (2 standing poles and 2 pyramids in each sub-area) and easy to be sampled by scuba divers.

The monitoring of the physico-chemical characteristics of the water column showed suitable conditions for diving from May to October with temperatures ≥20°C and surface currents having an intensity lower than 20 cm s^{-1} which tends to decrease at increasing depth. Only on very few occasions the superficial current exceeded the 50 cm s-1 for short time periods (12-24 h); in those conditions the divers would have a bit of difficulty as well as the small-scale fishers for the positioning of the set gears at sea. The transparency along the water column is generally greater in summer; however, the frequent low turbidity just close to the bottom could represent a limitation for diving, especially for inexperienced people. On the other hand, this apparently limiting factor, associated with the geometrical arrangement of the structures could make the reef a suitable site for advanced scuba diver training.

All the physical and bio-chemical parameters, especially the absence of hypoxia phenomena, showed good environmental conditions for the growth of marine organisms. This has been confirmed by the investigations on the benthic population settled on the substrates as well as those on the fish assemblage which have evidenced the occurrence of consistent and well diversified communities with species of interest either for divers and for recreational or professional fishers. Indeed, several studies demonstrated that, in suitable environmental conditions, an artificial reef installation has a significant impact on increasing fouling organisms, fish abundance, and species richness (Puspasari *et al.*, 2020). In the case of the Porto Recanati - Porto Potenza Picena AR, the structural complexity of the reef has favoured the settlement and proliferation of autogenous engineers, represented by bryozoans, anthozoans, sponges, bivalves and encrusting algae. The presence of biogenic structures increases habitat quality and affects habitat selection, abundance of economically valuable species, fish survival and settlement (Komyakova *et al.*, 2018; Seemann *et al.*, 2018; Soler-Hurtado *et al.*, 2018), positively influencing the area's ecosystem functions and services.

In this regard, the UVC carried out by scuba divers and ROV have highlighted the occurrence of a fish assemblage mainly composed of demersal reef-dwelling and partially reef-dwelling species such as, for example, sparids (e.g., *Diplodus vulgaris*, *Diplodus sargus*, *Oblada melanura*), *Scorpaena* spp., *Sciaena umbra*, and blennies (e.g., *Parablennius rouxi*, *P.arablennius tentacularis*, *Parablennius rouxi*). Some of these species, e.g. *Scorpaena* spp and sparids, seem to have established a resident population at the reef having been detected all the year round, while others, specially pelagics, are transient and aggregate at the reef site from late spring to fall (e.g., *Boops boops*, *Trachurus* spp., *Seriola dumerili*). The increase of diversity observed during summer months has been already reported at other artificial reefs deployed in the coastal areas of the central-northern Adriatic Sea (Fabi and Fiorentini, 1994; Bombace *et al*., 2000) and it is linked to the general ontogenetic migrations observed for most Adriatic species (Vrgoč *et al.*, 2004), which typically reside in the deeper and warmer waters during winter and move coastward when the water temperature increases.

Finally, the mussel population settled on the artificial structures of the reef in June 2021 was almost exclusively constituted by young individuals likely settled in fall 2020 and from early winter to spring 2021. The absence of specimens with shell length equal or greater than the minimum commercial size, which were very abundant on the reef structures in 2019, is certainly due to an indiscriminate harvesting by recreational and professional fishers between 2019 and 2020, confirming the free access to and the indiscriminate exploitation of the reef resources. However, based on the growth and mortality rates derived by previous studies (Fabi *et al*., 1989; Giulini and Maffei, 1994) it results that the mussels settled on the pyramids and poles will take around 8-9 months to reach the average size of 50mm SL with a final commercial biomass of 33.8 Kg/m^2 for the mussels settled on the pyramids and 33.0 Kg/m^2 on the poles. These values are in line with those already reported at other artificial reefs located in the central-northern Adriatic Sea (20-55 Kg/m^2; Bombace *et al*., 1994) as well as with the commercial biomass estimated for the natural rocky bottoms of the Conero Promontory (10-40 Kg/m^2; Fabi *et al*., 2013). The quality of mussels, in terms of contaminant levels, algal toxins and pathogens has resulted excellent over the two years of investigation (2020-2021). This aspect, associated with the abundance of mussels could constitute the premises for the possible development of recognizable quality brand.

The overall results indicate that the artificial reef of Porto Recanati - Porto Potenza Picena provides a range of ecosystem functions and services which could favour the development of new sustainable activities and/or the implementation of existing ones leading to an improvement of the local economy according to the principles of the Blue Growth. Considering the features of the reefs highlighted by the monitoring phase it results that the most suitable activities to be implemented in the area would be the professional small-scale fisheries with set gear, the collection of mussels settled on the man-made structures, the recreational fishing (e.g., fishing trips, fishing tourism) and diving. Obviously, the sustainable development of one or more of the above activities would necessarily require an adequate management aimed to avoid spatial conflicts and overexploitation of the reef resources.

6. REFERENCES

Andaloro F., Catriota L., Ferraro M., Romeo T., Sara G., Consoli P. 2011. Evaluating fish assemblages associated with gas platforms: Evidence from a visual census technique and experimental fishing surveys. *Ciencias Marinas*, 37: 1–9. http://www.scielo.org.mx/scielo.php?pid=S0185-38802011000100001&script=sci_abstract&tlng=en (Accessed 27 July 2021).

Artegiani, A., Bregant D., Paschini E., Pinardi N., Raicich F., Russo A. 1997a. The Adriatic Sea general circulation. Part I. Air-sea interactions and water mass structure. *J. Phys. Oceanogr.*, 27: 1492– 1514.

Artegiani, A., Bregant D., Paschini E., Pinardi N., Raicich F., Russo A. 1997b. The Adriatic Sea general circulation. Part II: Baroclinic Circulation Structure. *J. Phys. Oceanogr.*, 27: 1515- 1532.

Bernard A.T.F., Götz A., Kerwath S.E., Wilke C.G. 2013. Observer bias and detection probability in underwater visual census of fish assemblages measured with independent double-observers. *J. Experim. Mar. Biol. Ecol.*, 443: 75–84.

Blair R.C., Higgins James. J. 1980. A Comparison of the Power of Wilcoxon's Rank-Sum Statistic to That of Student's t Statistic Under Various Non-normal Distributions". *J. Educat. Stat.*, 5(4): 309–335.

Bolker B.M., Brooks M.E., Clark C.J., Geange S.W., Poulsen J.R., Stevens M.H.H., White J.S.S. 2009. *Generalized linear mixed models: a practical guide for ecology and evolution*. Elsevier.

Bombace G., Fabi G., Fiorentini L. 2000. Artificial reefs in the Adriatic Sea. Pages 31-63, *in* Jensen A.C. et al. (eds), Artificial reefs in the European Seas. Kluwier Academic Publishers, Dordrecht, The Netherlands.

Bombace G., Fabi G., Fiorentini L., Spagnolo A. 1995. Assessment of the ichthyofauna of an artificial reef through visual census and trammel net: comparison between the two sampling techniques. Pagg. 291-305, *in* Hawkins L.E., Hutchinson S. with Jensen A.C., Sheader M., Williams J.A. (eds.) The Responses of Marine Organisms to their Environments - Proceedings of the 30th European Marine Biological Symposium. University of Southampton, Southampton, UK.

Bombace G., Fabi G., Fiorentini L., Speranza S. 1994. Analysis of the efficiency of artificial reefs located in five different areas of the Adriatic Sea. *Bull. Mar. Sci.*, 55: 559–580.

Bortone S.A., Kimmel J.J. 1991. Environmental Assessment and Monitoring of Artificial Habitats. http://www.vliz.be/imisdocs/publications/ocrd/211813.pdf (Accessed 16 July 2021).

Fabi G., Fiorentini L. 1994. Comparison between an artificial reef and a control site in the Adriatic Sea: analysis of four years of monitoring. *Bull. Mar. Sci.*, 55(2-3): 538-558.

Fabi G., Fiorentini L., Giannini S. 1989. Experimental shellfish culture on an artificial reef in the Adriatic sea. *Bull. Mar. Sci.*, 44(2): 923-933.

Fabi G., Grati F., Gramolini R., Scarcella G., Spagnolo A. 2013. ARs as fisheries management tool the case of the northern Adriatic Sea. 1st Euro-Mediterranean conference on artificial reef management. 5-8 Feb. 2013, Marseille. Marseille City Council.

Fife D.A. 2019. Flexplot: graphically-based data analysis. *PsyArXiv*. doi: 10.31234/osf.io/kh9c3

Fife D.A. 2020. The Eight Steps of Data Analysis: A Graphical Framework to Promote Sound Statistical Analysis. *Perspectives on Psychological Science*. doi: https://doi.org/10.1177/1745691620917333

Froese R., Pauly D. 2019. *Fishbase*. World Wide Web electronic publication.

Giulini G., Maffei M. 1994. *Analisi di alcuni parametri di qualità in popolazioni di mitili (Mytilus galloprovinciais LAMK) provenienti da diverse condizioni di allevamento e da banco naturale. Valutazione comparativa*. Report for the Italian Mercantile Marine Ministry.

Grilli F. Accoroni S., Acri F., Bernardi Aubry F., Bergami C., Cabrini M., Campanelli A., Giani M., Guicciardi S., Marini M., Neri F., Penna A., Penna P., Pugnetti A., Ravaioli M., Riminucci F., Ricci F., Totti C., Viaroli P., Cozzi S. 2020. Seasonal and Interannual Trends of Oceanographic Parameters over 40 Years in the Northern Adriatic Sea in Relation to Nutrient Loadings Using the EMODnet *Chemistry Data Portal. Water*, 12(8): 2280.

Hammer Ø., Harper D.A.T., Ryan P.D. 2001. PAST: Paleontological statistics software package for education and data analysis. *Palaeontologia Electronica* 4(1): 9pp. http://palaeo-electronica.org/2001_1/past/issue1_01.htm

Komyakova V., Jones G., Munday P. 2018. Strong effects of coral species on the diversity and structure of reef fish communities: a multi-scale analysis. PLOS ONE 13. e0202206DOI 10.1371/journal.pone.0202206.

Konovalov D.A, Saleh A., Bradley M., Sankupellay M., Marini S., Sheaves M. 2019. Underwater fish detection with weak multi-domain supervision. International Joint Conference on Neural Networks (IJCNN) doi: 10.1109/IJCNN.2019.8851907

Komyakova V., Jones G., Munday P. 2018. Strong effects of coral species on the diversity and structure of reef fish communities: a multi-scale analysis. *PLOS ONE*, 13 : e0202206DOI 10.1371/journal.pone.0202206.

Lipizer M., Partescano E., Rabitti A., Giorgetti A., Crise A. 2014 Qualified temperature, salinity and dissolved oxygen climatologies in a changing Adriatic Sea. *Ocean Science*, 10: 771–797.

Luther W., Fiedler K. 2018. *Guida alla fauna marina costiera del Mediterraneo*. Roma: Muzio F. Editor. Hamburg/Berlin: Verlag Paul Parey. 224 pp.

Maas H.G. 1995. New developments in multimedia photogrammetry. *Optical 3D measurement techniques III*.

Mccurdy P.G., Woodward L.A., Davidson JL., Wilson R.M., Ask R. 1944. Manual of photogrammetry. *Manual of photogrammetry.*

Minchin, P. R. 1987. An evaluation of the relative robustness of techniques for ecological ordination. *Vegetatio*, 69: 89–107.

Murase T., Tanaka M., Tani T., Miyashita Y., Ohkawa N., Ishiguro S., Suzuki Y., Kayanne H., Yamano H. 2008. A photogrammetric correction procedure for light refraction effects at a two-medium boundary. *Photogrammetric engineering & remote sensing*, 74(9): 1129-1136.

Neyer F., Nocerino E., Gruen A. 2018. Monitoring coral growth the dichotomy between underwater photogrammetry and geodetic control network. *The International Archives of Photogrammetry, Remote Sensing and Spatial Information Sciences*, XLII-2: 759-766.

Nikiforos G. 2005. *Fauna del Mediterraneo, Guida Completa*. Firenze: Giunti Gruppo Editoriale. 366 pp.

Oksanen A.J., Blanchet F.G., Friendly M., Kindt R., Legendre P., Mcglinn D., Minchin P.R., *et al.* 2016. Vegan: Community Ecology Package. https://github.com/vegandevs/vegan.

Parsons T.R., Maita Y., Lalli C.M. 1985. *A manual of chemical and biological methods for seawater analysis*. Oxford Pergamon Press. 173 pp.

Puspasari R., Wiadnyana N.N., Hartati S.T., Rachmawati R., Yahya Y. 2020. The effectiveness of artificial reefs in improving ecosystem health to Increase coral reef resilience. *J. Segara*, 16-2: 115-126.

Quinn G.P., Keough M.J. 2002. *Experimental Design and Data Analysis for Biologist*. Cambridge University Press, New York, NY , USA, New York. 283 pp.

Riedl R. 1991. *Flora e fauna del Mediterraneo*. Muzio F. Eeditor. Hamburg/Berlin: Verlag Paul Parey. 777 pp.

Rilov G., Benayahu Y. 2000. Fish assemblage on natural versus vertical artificial reefs: The rehabilitation perspective. *Mar. Biol*., 136: 931–942.

Rinaldi A. 2017. *Atlante della fauna e flora marina dell'Adriatico nord-occidentale*. La Mandragora s.r.l. Editor. 718 pp.

Rossi P., Castagnetti C., Capra A. Brooks A.J., Mancini F. 2020. Detecting change in coral reef 3D structure using underwater photogrammetry: critical issues and performance metrics. *Appl. Geomat.,* 12: 3–17.

Salman A., Siddiqui S.A., Shafait F., Mian A., Shortis M.R., Khurshid K., Ulges A., Schwanecke U. 2020, Automatic fish detection in underwater videos by a deep neural network-based hybrid motion learning system. *ICES J. Mar. Sci*., 77(4): 1295-1307.

Seeman J., Yingst A., Stuart-Smith R., Edgar G., Altieri A. 2018. The importance of sponges and mangroves in supporting fish communities on degraded coral reefs in Caribbean Panama. *PeerJ*, 6: e4455 DOI 10.7717/peerj.4455.

Shapiro S.S., Bradbury W.M. 1965. An analysis of variance test for normality (complete samples). *Biometrika*, 52(3-4): 591-611.

Soler-Hurtado M., Megina C., López-González P. 2018. Structure of gorgonian epifaunal communities in Ecuador (eastern Pacific). Coral Reefs, 37: 723–736.

Totti C., Romagnoli T., Accoronci S., Coluccelli A., Pellegrini M., Campanelli A., Grilli F., Marini M. 2019. Phytoplankton communities in the northwestern Adriatic Sea: Interdecadal variability over a 30-years period (1988–2016) and relationships with meteoclimatic drivers. *J. Mar. Syst.*, 193: 137-153.

Trygonis V., Sini M. 2012. PhotoQuad: a dedicated seabed image processing software, and a comparative error analysis of four photoquadrat methods. *J. Exp. Mar. Biol. Ecol.*, 424–425: 99-108.

UNESCO 1988. T*he acquisition, calibration and analysis of CTD data. A report of SCOR WG 5*1. Technical papers in Marine Sciences, 54: 1-59.

Velasco D.W., Wilson W.D., Nylund S., Heitsenrether R. 2018. Enhancing the Accuracy of Current Profiles from Surface Buoy-Mounted Systems. *OCEANS - MTS/IEEE Kobe Techno-Oceans (OTO).* 6 pp. doi: 10.1109/OCEANSKOBE.2018.8559481

Vrgoč N., Arneri E., Jukić-Peladić S., Šifner S. 2004. Review of current knowledge on shared demersal stocks of the Adriatic Sea. *In* AdriaMed Technical Documents, Vol 12, p. 91. http://www.ismar.cnr.it/file/file-generali/pg/Adriamed 2004.pdf (Accessed 20 December 2019).

Wilcoxon F. 1945. Individual comparisons by ranking methods. *Biom. Bull.,* 1(6): 80–83.

WoRMS Editorial Board. 2020. *World Register of Marine Species*. Available from http://www.marinespecies.org at VLIZ. Accessed 2021-05-30. doi:https://doi.org/10.14284/170

Zavatarelli M., Raicich F., Bregant D., Russo A., Artegiani A., 1998. Climatological biogeochemical characteristics of the Adriatic Sea. *J. Mar. Syst*., 18: 227–263.

ANNEX I - Bathymetric maps

Annex I is attached separately in PDF format ("AnnexI_Bathymetric maps.pdf"). Given the extension of the reef, it is composed of 6 bathymetric charts (A3 size, scale 1: 40.000): 3 charts with contour lines (0.25 m intervals) and 3 charts with the hill-shaded surface (0.2 m resolution). Each page contains two custom inset maps that help the user maintain the geographical frame of reference. Maps are presented in geographic coordinates (datum WGS 84).

ANNEX II - Map for fishers

Annex II is attached separately in PDF format ("AnnexII_Map for fishers.pdf"). It is the multibeam bathymetry coverage (0.20m resolution) of the northern part of the reef, with imprinted explicit geographic coordinates (WGS 84, DD MM.MM format) and distances between some structures. It was distributed to fishers which are active in this part of the reef in order to encourage their involvement.

ANNEX III - List of equipment that make up the rea-time meteo-oceanographic monitoring buoy system

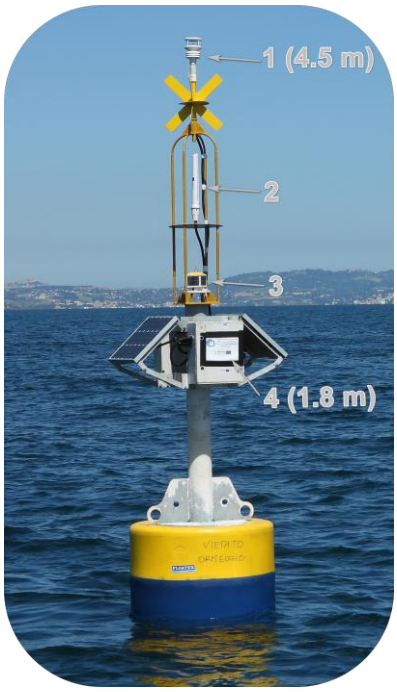

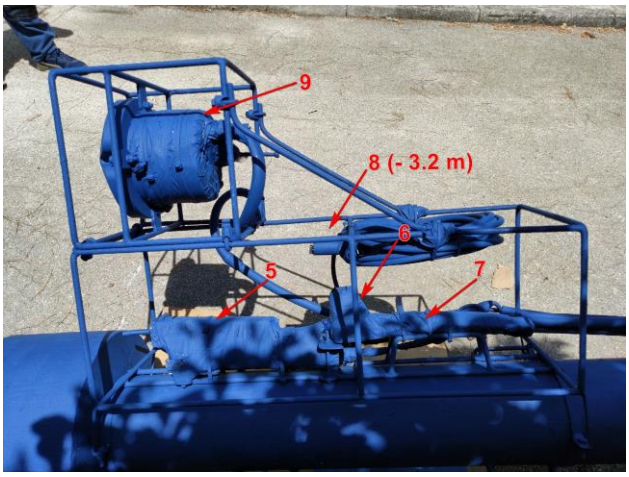

Adrireef meteo-oceanographic buoy system equipment.

The values in brackets indicate the height of the sensors above sea level. The numbers refer to the <Ref> column in the table below.

Ref	Image	Description
1		**Gill Maximet GMX500** s/n: 1957-0500-60-100 The MaxiMet GMX500 is a compact, robust and lightweight weather station. Parameters measured include temperature, relative humidity, barometric pressure, absolute humidity, air density, wet bulb temperature and inclinometer (Tilt coordinates X and Y in terms of degrees and Z in terms of orientation). In addition, a solid state ultrasonic sensor provides extremely accurate wind speed and direction measurements. An electronic compass comes as standard, which delivers apparent wind, WMO wind averages and gust data. Moreover, the addition of the GPS antenna receiver module allows to correct misalignments of the north marker (fundamental in a buoy that is free to rotate without particular constraints). The module is capable of receiving signals from up to 48 GPS satellites and transferring them into position and timing information. Position tracking is important to keep track of any unexpected buoy displacements.
2		**Poynting omnidirectional antenna OMNI-291** s/n: OMNI-291-V2-CH01230 The OMNI-291 is a high-performance marine antenna (robust and all-weather proof for harsh conditions at sea IP68, UV and saltwater protected). The ultra-wide frequency band covers all contemporary LTE operating frequencies with excellent balanced gain across all frequencies, including the LTE & CDMA 450 MHz bands which are common requirements for marine applications. The OMNI-291 guarantees signal reception almost everywhere along the coast. Thanks to an omnidirectional gain of 7dBi, it allows an excellent LTE coverage in the buoy deployment area (about 3 miles from the coast).

3		## Tideland SolaMax 65 The SolaMax-65 is a multi-purpose, self-contained solar-powered LED light. It features unique and proprietary optics which provide a 360° beam at 5°, 10°, 20° or 30° vertical divergence. It uses a specially designed lens to focus the light on the horizon. The light source consists of a string of 10 high intensity LEDs.
4		## Datalogger Campbell Scientific CR1000X s/n: 9932 The CR1000X is a low-powered device designed to measure sensors, drive direct communication and telecommunications, analyze data, control external devices, and store data and programs in on-board, non-volatile storage. The electronics are RF-shielded and glitch-protected by a unique sealed, stainless-steel canister. A battery-backed clock assures accurate timekeeping. The on-board, BASIC-like programming language—common to all Campbell Scientific data loggers—supports data processing and analysis routines. The CR1000X wiring panel includes two switchable 12 V terminals, analog grounds dispersed among 16 analog terminals, and unpluggable terminal blocks for quick deployment. ## Router Teltonika RUT240 s/n: 11117216233 RUT 240 is a compact industrial 4G (LTE) router equipped with 2x Ethernet ports, WiFi and RutOS software for advanced networking solutions. It supports 4G network up to 150mbps in download and 50mbps in upload with low latencies. This guarantees fast and reliable communication between the local datalogger and CNR server. Moreover, it has low power consumption and can be put into sleep mode. ## Solar charger and Battery pack

5		SEA-BIRD SBE 37-SI equipped with antifouling devices s/n: 37-21327 The SBE 37-SI MicroCAT is a high-accuracy sensor with non-volatile memory, which includes a standard RS-232 serial interface. The SBE 37-SI measures conductivity, temperature and salinity (calculated). The MicroCAT's internal-field conductivity cell is immune to proximity errors and unaffected by external fouling.
6		SEA-BIRD SBE 63 s/n: 63-2387 The SBE 63 is an individually calibrated, high-accuracy, optical oxygen sensor. It includes a standard RS-232 serial interface. Each sensor is calibrated individually in a temperature-controlled bath. Bath temperatures are varied at each of 4 oxygen values, providing a comprehensive 24-point calibration. Two reference sensors in each bath are standardized against Winkler titrations. Response time tests are conducted on each sensor, using gas. Salinity and pressure impacts on sensor response are each checked at two separate points.
7		SBE 5T pump s/n: 05-10088 The SBE 5T pump ensures the circulation of seawater between the sensors. The high reliability of the pump and the presence of antifouling devices allow to acquire valid data for long periods.

8		**Turner Turbidity Plus CYclop 7 2180 with wiper** s/n: TRB000268 Turbidity Plus is an accurate single-channel turbidity sensor including an integrated wiper which is triggered by the user. It delivers a voltage output proportional to the turbidity of the sample which can be correlated to nephelometric turbidity unit (NTU) values by calibrating with a standard of known concentration. The wiper, even if not very powerful, allows to keep the sensor clean for a long time.
9		**NORTEK Signature 500 ADCP** s/n: 101504 Nortek Signature 500 is a five-beam current profiling system that measures current profiles at up to 8 Hz sampling frequency. Signature500 sensor heads have five acoustic transducers, four slanted at 25 degrees from vertical, and a fifth vertical beam. It can also measure direct vertical velocity profiles, wave height and direction. Furthermore, it includes a magnetometer and accelerometer used to compensate for the effects of wave motion on the buoy.

ANNEX IV - Images and data transferred at land and visualized through different media to make them accessible to the wide public

Information on the Adrireef project is available on the Institutional web site of the Porto Recanati Municipality (http://turismo.comune.porto-recanati.mc.it/).

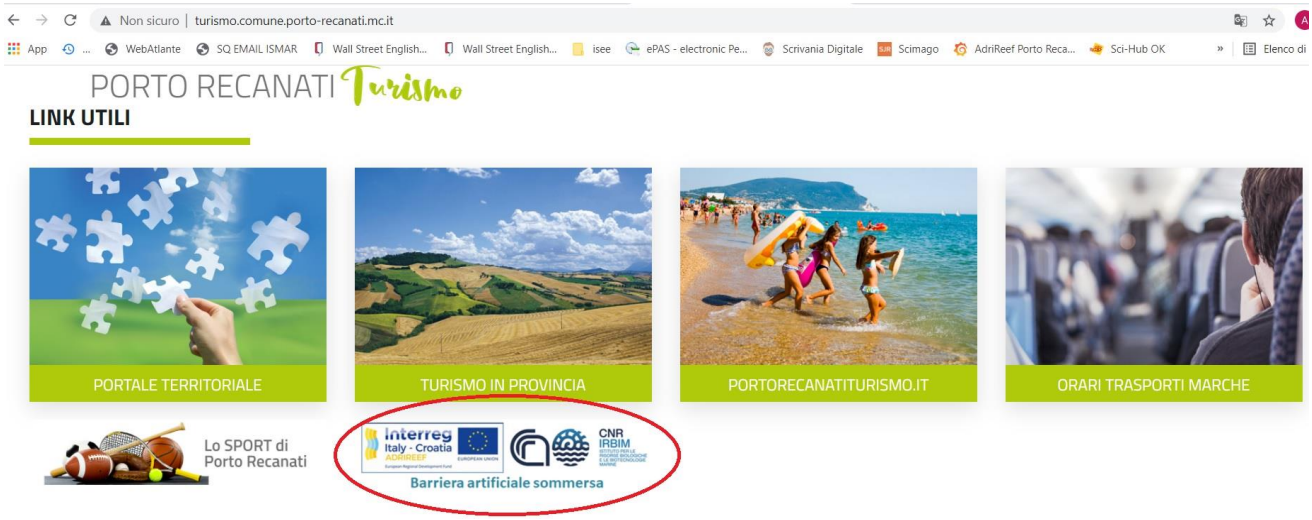

Just click the project logo to access the second page where the links to Adrireef project, to CNR-IRBIM homepage and to the oceanographic real time data are available. In this page (http://turismo.comune.porto-recanati.mc.it/barriera-artificiale-sommersa-porto-recanati/) a brief description of the artificial reef as well a video clip and some images of the fauna living inside the AR are available.

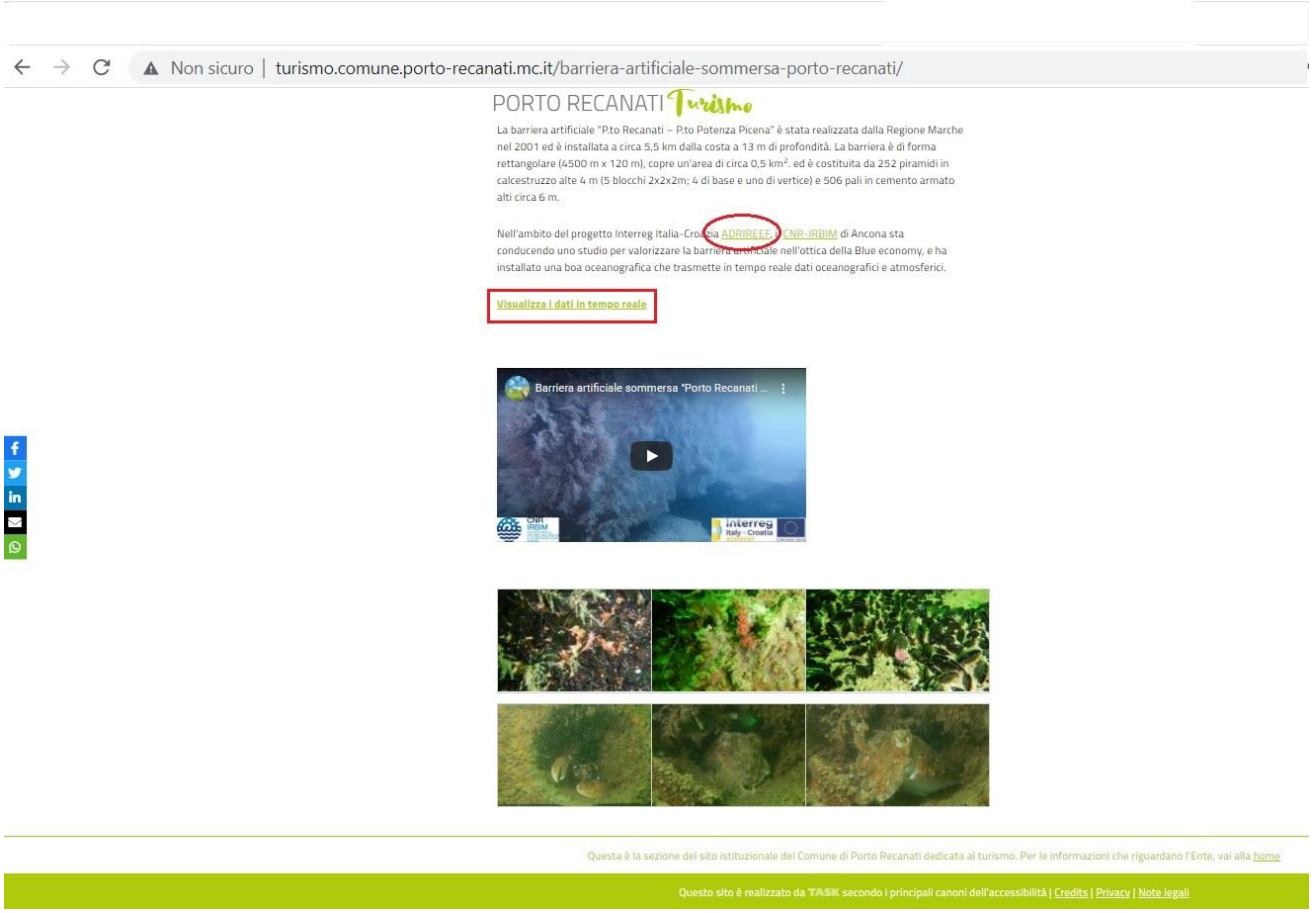

To visualize the data collected from the meteo oceanographic buoy, , a set of dashboards were implemented using a web solution provided by Grafana Labs. Grafana is open source visualization and analytics software. It allows you to query, visualize beautiful graphs, alert on, and explore time-series database (TSDB) data.

CNR staff has developed 3 dashboards /sites :

1. *AdriReef Porto Recanati* (https://gr.irbim.cnr.it/adrireef). A complete and detailed version with objects and graphs of all recorder weather and marine parameters.
2. *Progetto AdriReef: Barriera artificiale Porto Recanati - Porto Potenza Picena* (https://gr.irbim.cnr.it/adrireefpt) implemented for the Porto Recanati tourism site. This site was developed in cooperation with the municipality of Porto Recanati. The goal is to provide a simple and easy tool that can be viewed by all interested people even without a scientific background.

   These two sites are organized into the following sections:

- a header page showing some images and videos, a map with the real-time position of the buoy, and project and institutional logos.
- *Last observation* is a simplified and easily interpretable section that includes objects with weather information and most data related to measurements in water (Temperature, turbidity and currents).
- A series of graphs showing the trend of the main weather and marine parameters (air temperature, wind, humidity, pressure, water temperature, water turbidity, currents) against time.

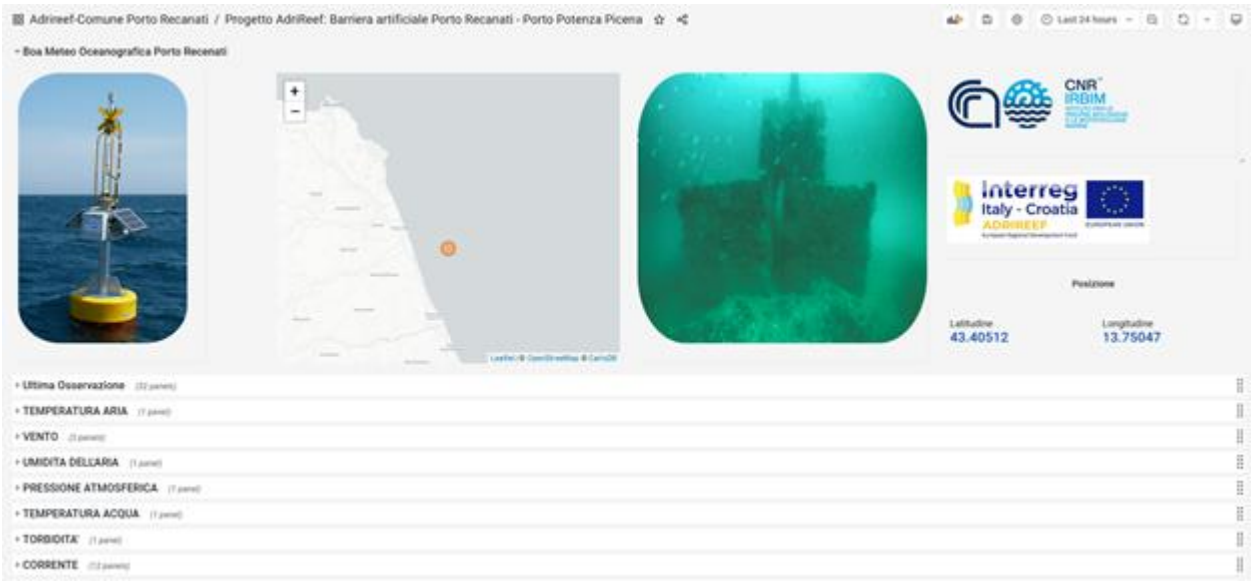

Visualization data website: header page.

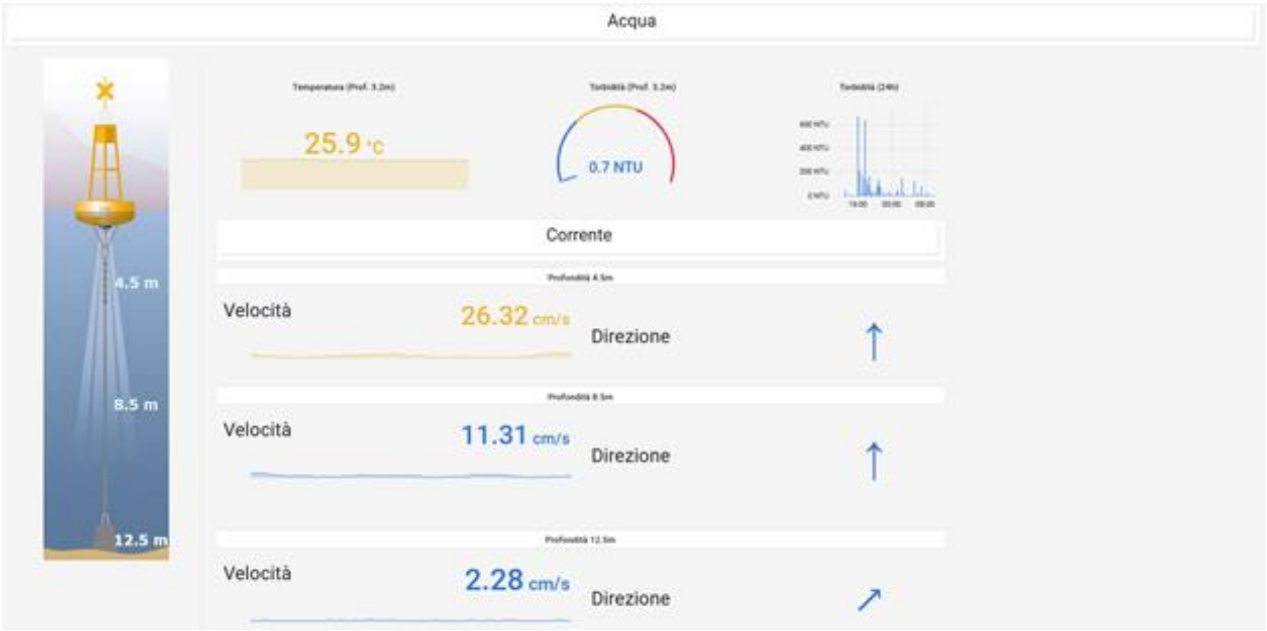

Visualization data website: last observation page reporting the real-time data collected (air temperature, wind, pressure, humidity, water temperature, water turbidity and currents).

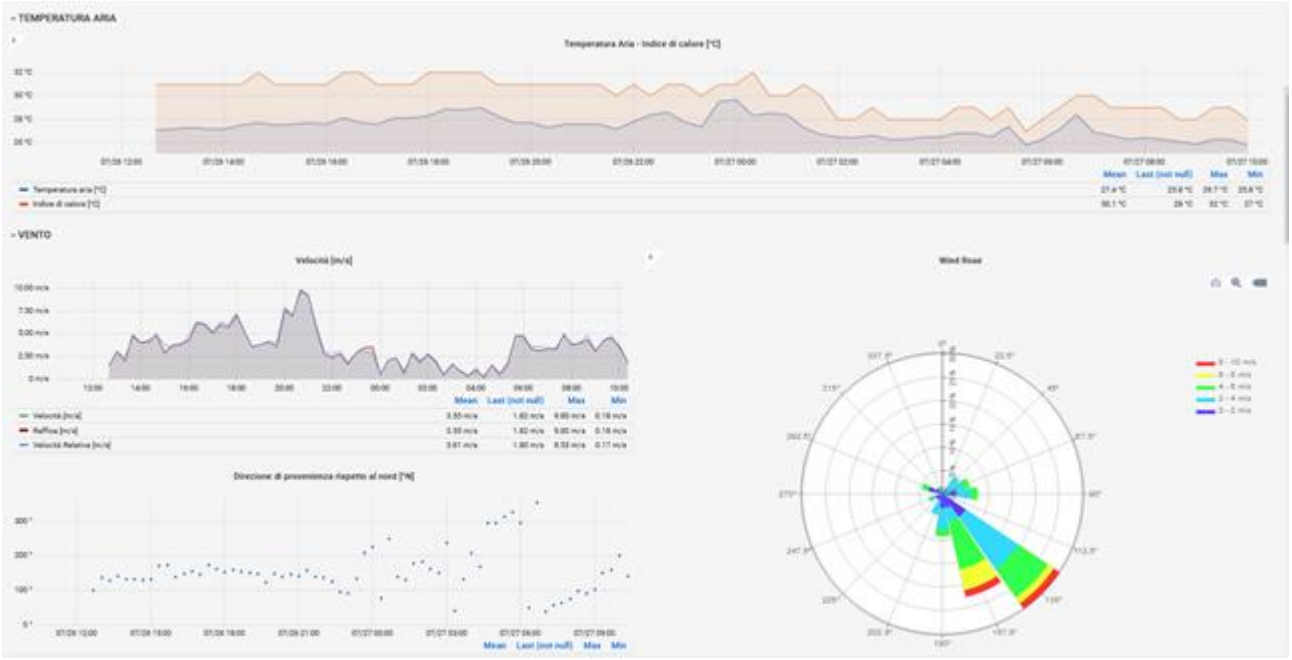

Visualization data website: panel with air temperature and wind graphs.

3. *Kiosk Version* (https://gr.irbim.cnr.it/adrkiosk/play/3?kiosk) with a dedicated format suitable for Totems . It includes 3 sections that cycle repeatedly: a header with a promotional video, the project logos and a map with the buoy position, a section with meteo parameters and another with water parameters and currents.

A totem installed along the main street of Porto Recanati. During the summer the city is very popular with tourists and therefore it was possible to reach a large audience.

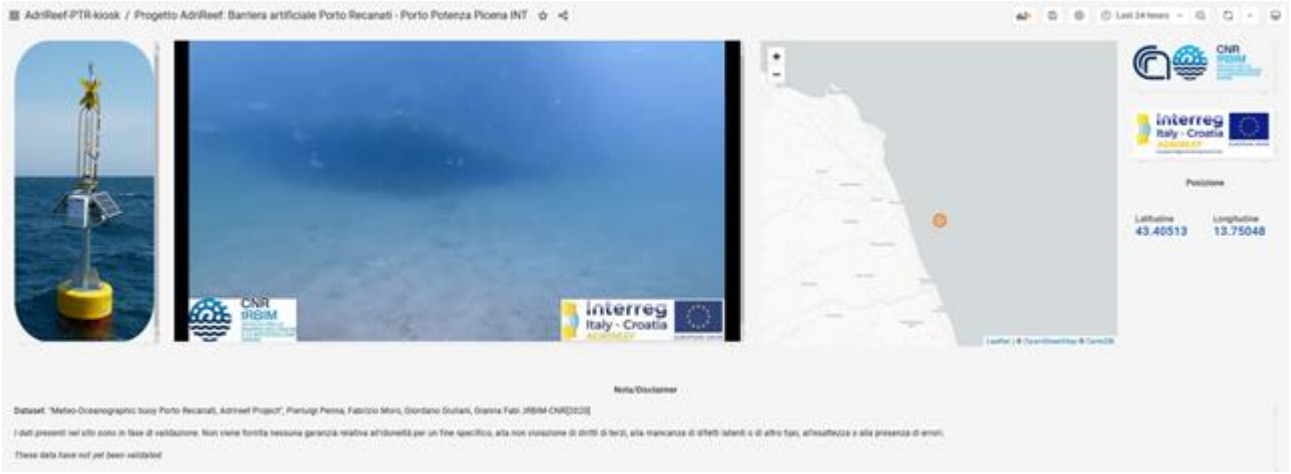

Kiosk site: header page.

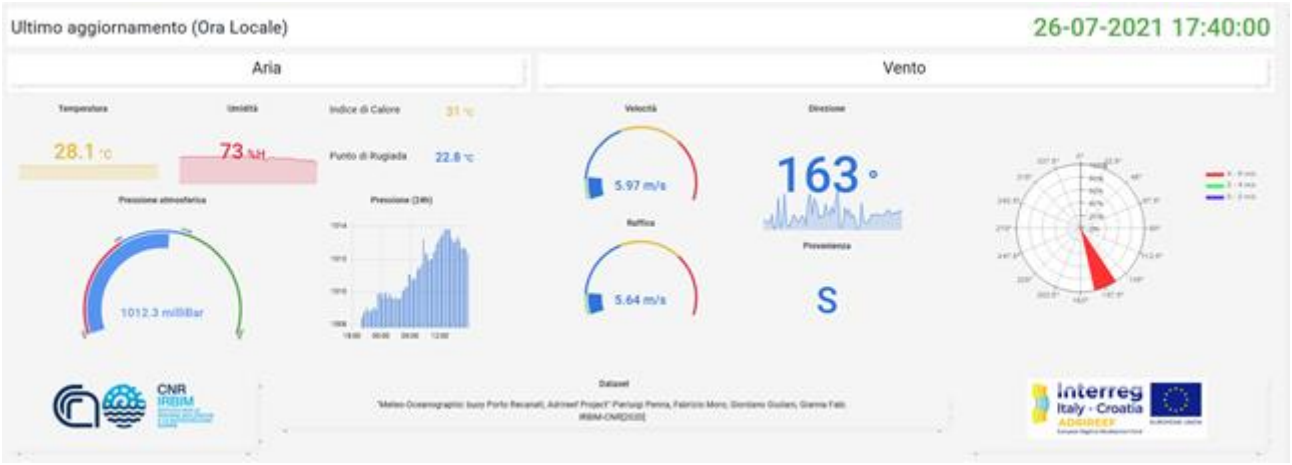

kiosk site: weather section (air temperature, humidity, pressure and wind).

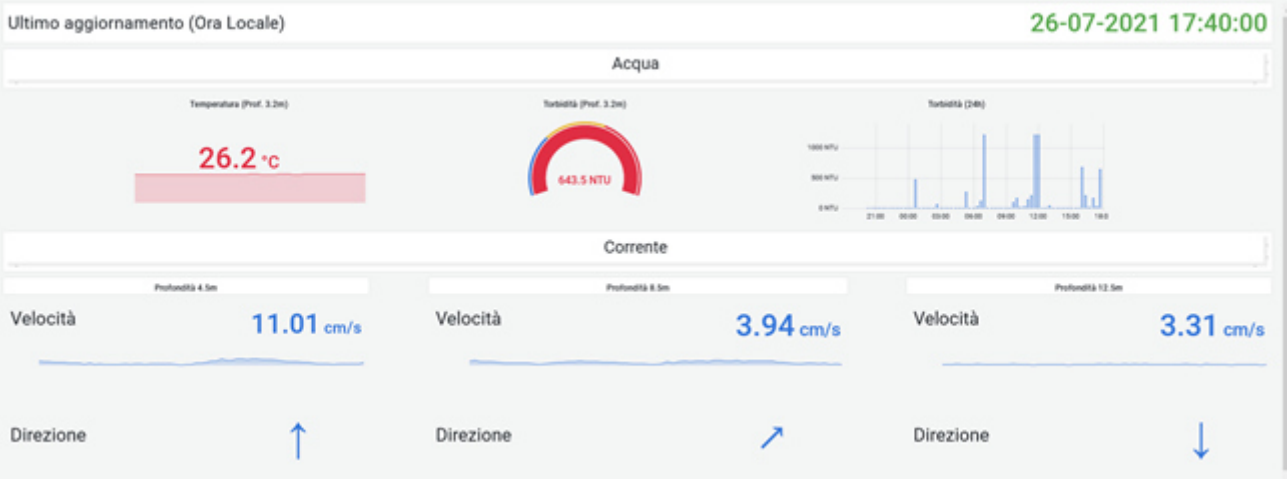

kiosk site: water section (water temperature, turbidity and currents).

All websites are accessible without authentication. Users can open or close a specific section by clicking in the header row. End users can manage the time ranges of data being visualized by acting on the time range controls.

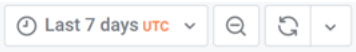

The following time units are supported: s (seconds), m (minutes), h (hours), d (days), w (weeks), M (months), and y (years). The current time range, also called the time picker, shows the time range currently displayed in the dashboard or panel you are viewing.

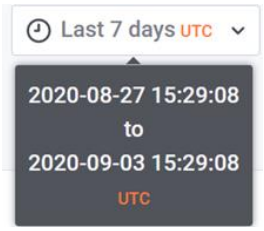

User can click on the current time range to change the time range and it's possible to change the current time by using a relative time range, such as the last 5 minutes, or an absolute time range, such as 2020-08-31 00:00:00 to 2020-09-03 23:59:59.

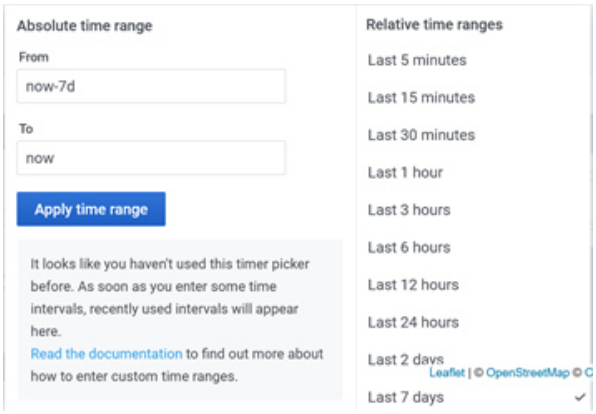
Absolute time range
From
now-7d
To
now
Apply time range
It looks like you haven't used this timer picker before. As soon as you enter some time intervals, recently used intervals will appear here.
Read the documentation to find out more about how to enter custom time ranges.
Relative time ranges
Last 5 minutes
Last 15 minutes
Last 30 minutes
Last 1 hour
Last 3 hours
Last 6 hours
Last 12 hours
Last 24 hours
Last 2 days
Last 7 days
Leaflet | © OpenStreetMap

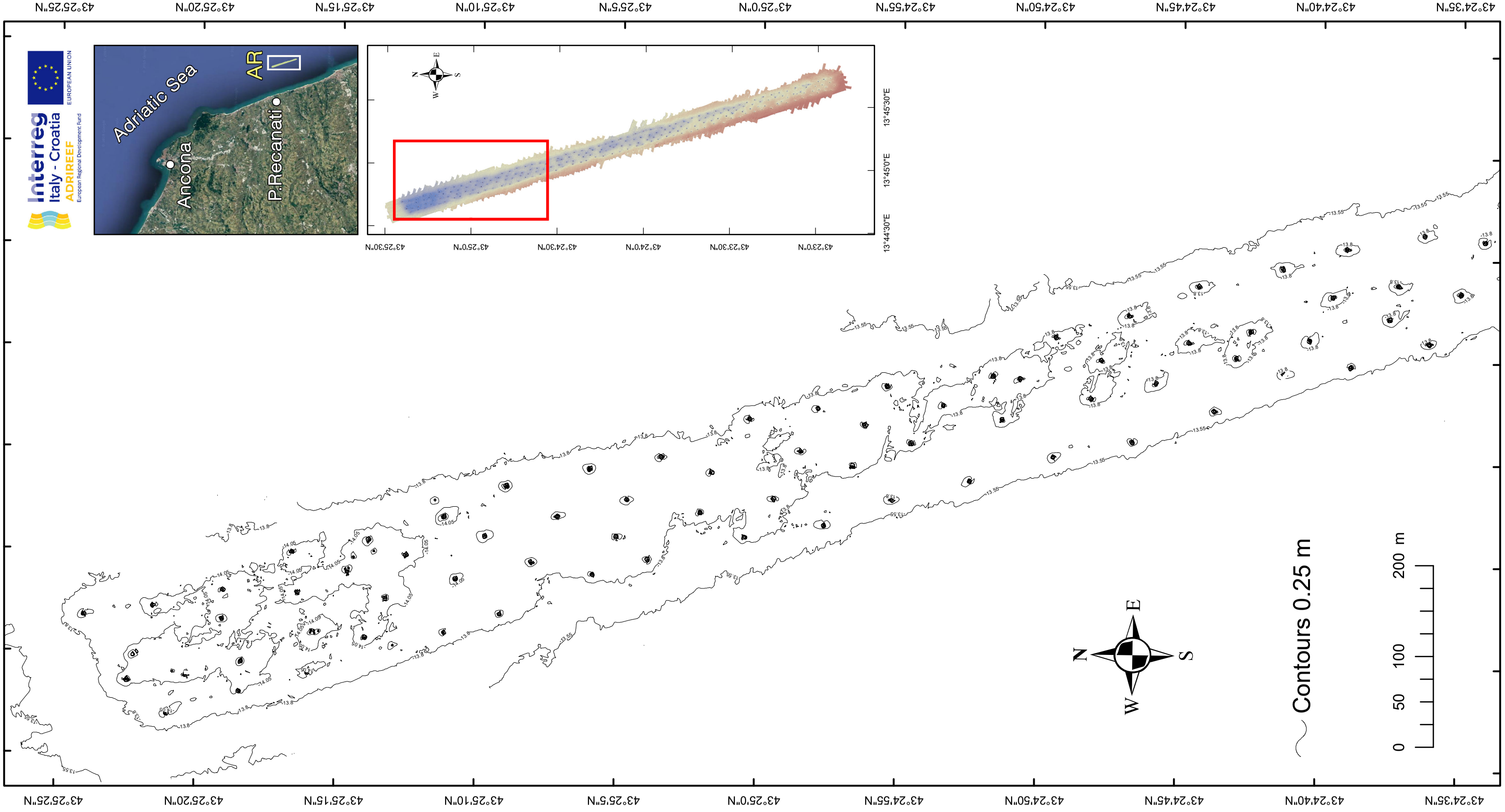
Interreg
Italy - Croatia
EUROPEAN UNION
ADRIREEF
European Regional Development Fund
Adriatic Sea
Ancona
P.Recanati
AR
Contours 0.25 m
0 50 100 200 m
N
S
E
W
13°44'35"E
13°44'40"E
13°44'45"E
13°44'50.01"E
13°44'55.01"E
13°45'0.01"E
13°45'5.01"E
13°45'10"E
43°24'35"N
43°24'40"N
43°24'45"N
43°24'50"N
43°24'55"N
43°25'0"N
43°25'5"N
43°25'10"N
43°25'15"N
43°25'20"N
43°25'25"N

Interreg
Italy - Croatia
EUROPEAN UNION
ADRIREEF
European Regional Development Fund

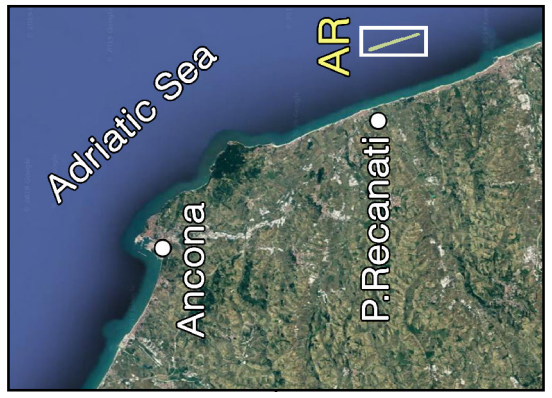

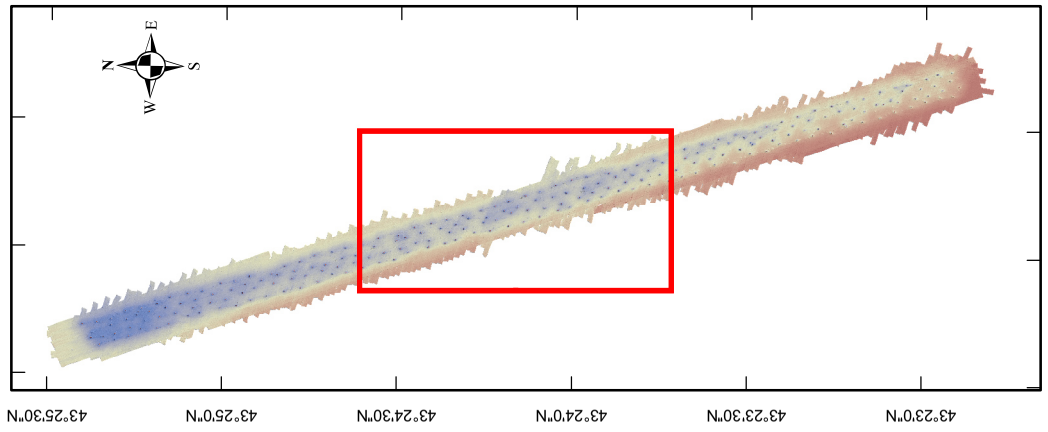

43°24'35"N
43°24'30"N
43°24'25"N
43°24'20"N
43°24'15"N
43°24'10"N
43°24'5"N
43°24'0"N
43°23'55"N
43°23'50"N
43°23'45"N

13°44'55.01"E
13°45'0.01"E
13°45'5.01"E
13°45'10"E
13°45'15"E
13°45'20"E
13°45'25"E

13.8
13.55

N
E
S
W

Contours 0.25 m

0 50 100 200 m

Interreg
Italy - Croatia
EUROPEAN UNION
ADRIREEF
European Regional Development Fund

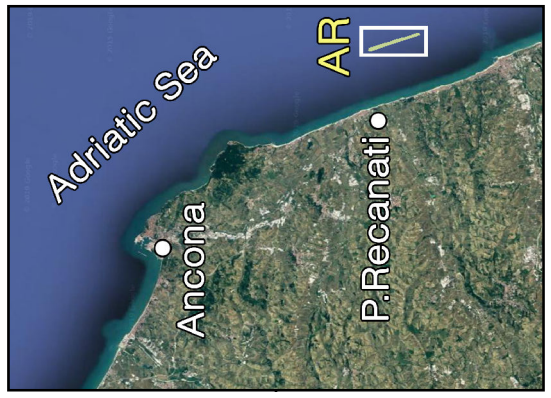

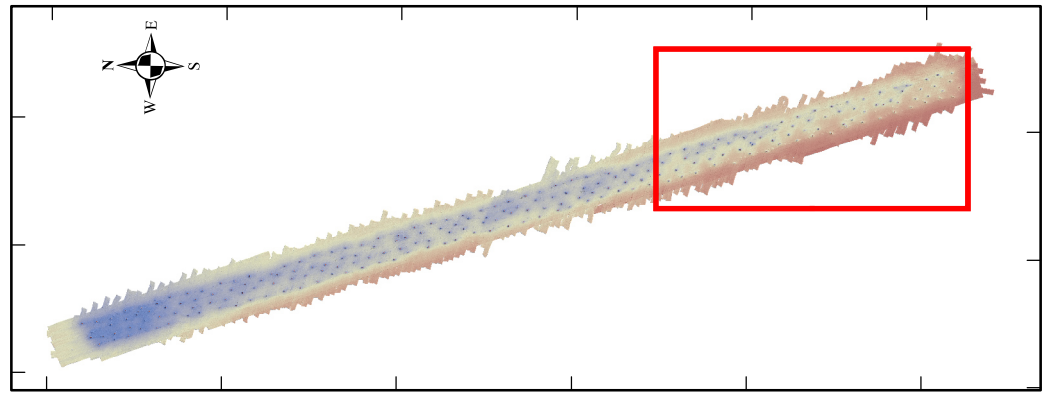

43°22'55"N
43°23'0"N
43°23'5"N
43°23'10"N
43°23'15"N
43°23'20"N
43°23'25"N
43°23'30"N
43°23'35"N
43°23'40"N
43°23'45"N

13°45'15"E
13°45'20"E
13°45'25"E
13°45'30"E
13°45'35"E
13°45'40"E
13°45'45.01"E

Contours 0.25 m

0 50 100 200 m

N E S W

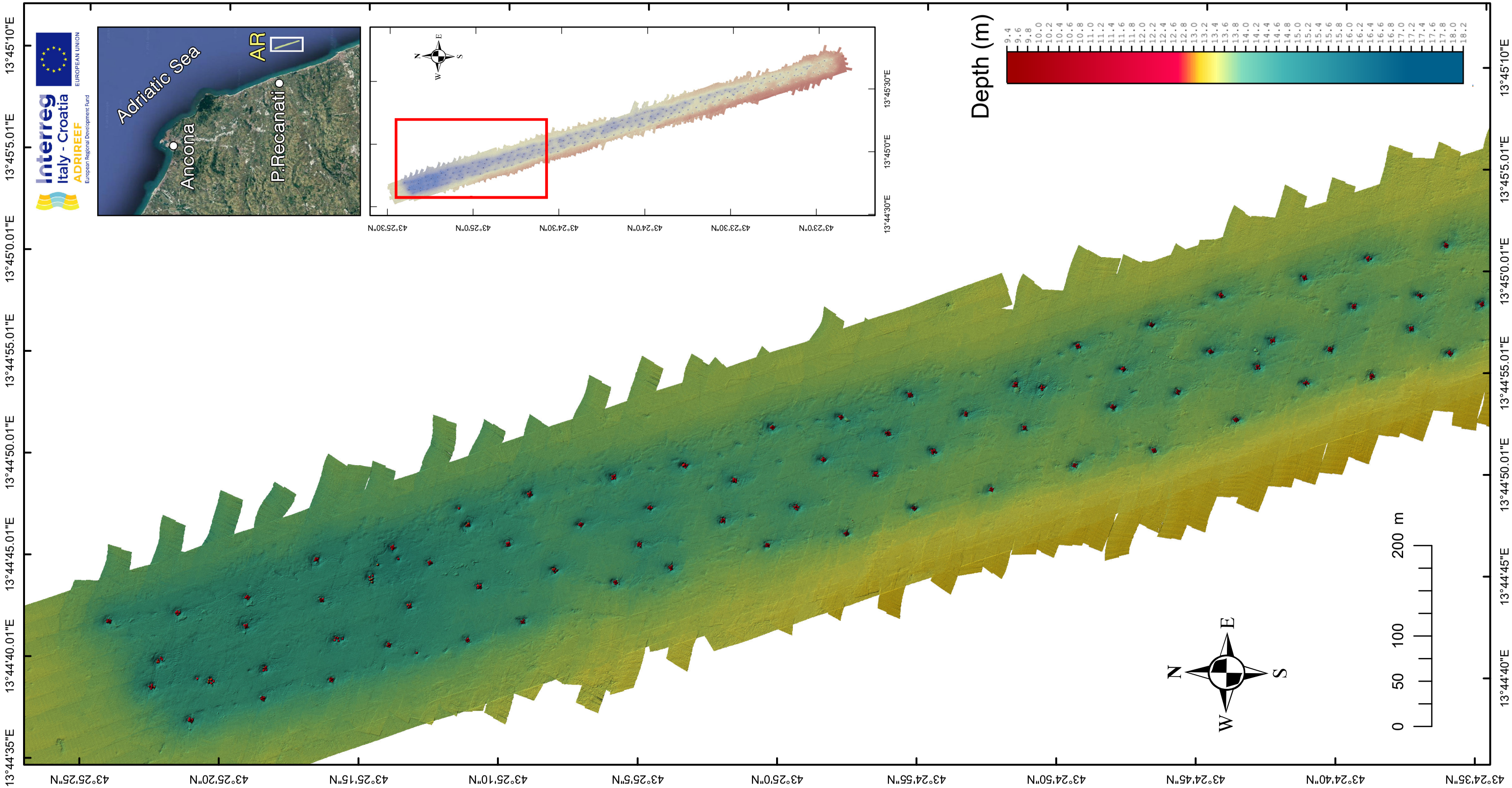
Interreg
Italy - Croatia
ADRIREEF
European Regional Development Fund
EUROPEAN UNION
Adriatic Sea
Ancona
P.Recanati
AR
Depth (m)
9.4
9.6
9.8
10.0
10.2
10.4
10.6
10.8
11.0
11.2
11.4
11.6
11.8
12.0
12.2
12.4
12.6
12.8
13.0
13.2
13.4
13.6
13.8
14.0
14.2
14.4
14.6
14.8
15.0
15.2
15.4
15.6
15.8
16.0
16.2
16.4
16.6
16.8
17.0
17.2
17.4
17.6
17.8
18.0
18.2
N
S
E
W
0
50
100
200 m
13°44'35"E
13°44'40.01"E
13°44'45.01"E
13°44'50.01"E
13°44'55.01"E
13°45'0.01"E
13°45'5.01"E
13°45'10"E
13°44'30"E
13°45'0"E
13°45'30"E
43°24'35"N
43°24'40"N
43°24'45"N
43°24'50"N
43°24'55"N
43°25'0"N
43°25'5"N
43°25'10"N
43°25'15"N
43°25'20"N
43°25'25"N
43°23'30"N
43°24'0"N
43°24'30"N
43°25'0"N
43°25'30"N

Interreg
Italy - Croatia
ADRIREEF
European Regional Development Fund
EUROPEAN UNION

Adriatic Sea
Ancona
P.Recanati
AR

Depth (m)
9.4
9.6
9.8
10.0
10.2
10.4
10.6
10.8
11.0
11.2
11.4
11.6
11.8
12.0
12.2
12.4
12.6
12.8
13.0
13.2
13.4
13.6
13.8
14.0
14.2
14.4
14.6
14.8
15.0
15.2
15.4
15.6
15.8
16.0
16.2
16.4
16.6
16.8
17.0
17.2
17.4
17.6
17.8
18.0
18.2

N
E
S
W

0 50 100 200 m

13°44'55.01"E
13°45'0.01"E
13°45'5.01"E
13°45'10"E
13°45'15"E
13°45'20"E
13°45'25"E
13°45'30"E
13°44'30"E
13°45'0"E

43°23'45"N
43°23'50"N
43°23'55"N
43°24'0"N
43°24'5"N
43°24'10"N
43°24'15"N
43°24'20"N
43°24'25"N
43°24'30"N
43°24'35"N
43°23'0"N
43°23'30"N
43°24'0"N
43°24'30"N
43°25'0"N
43°25'30"N

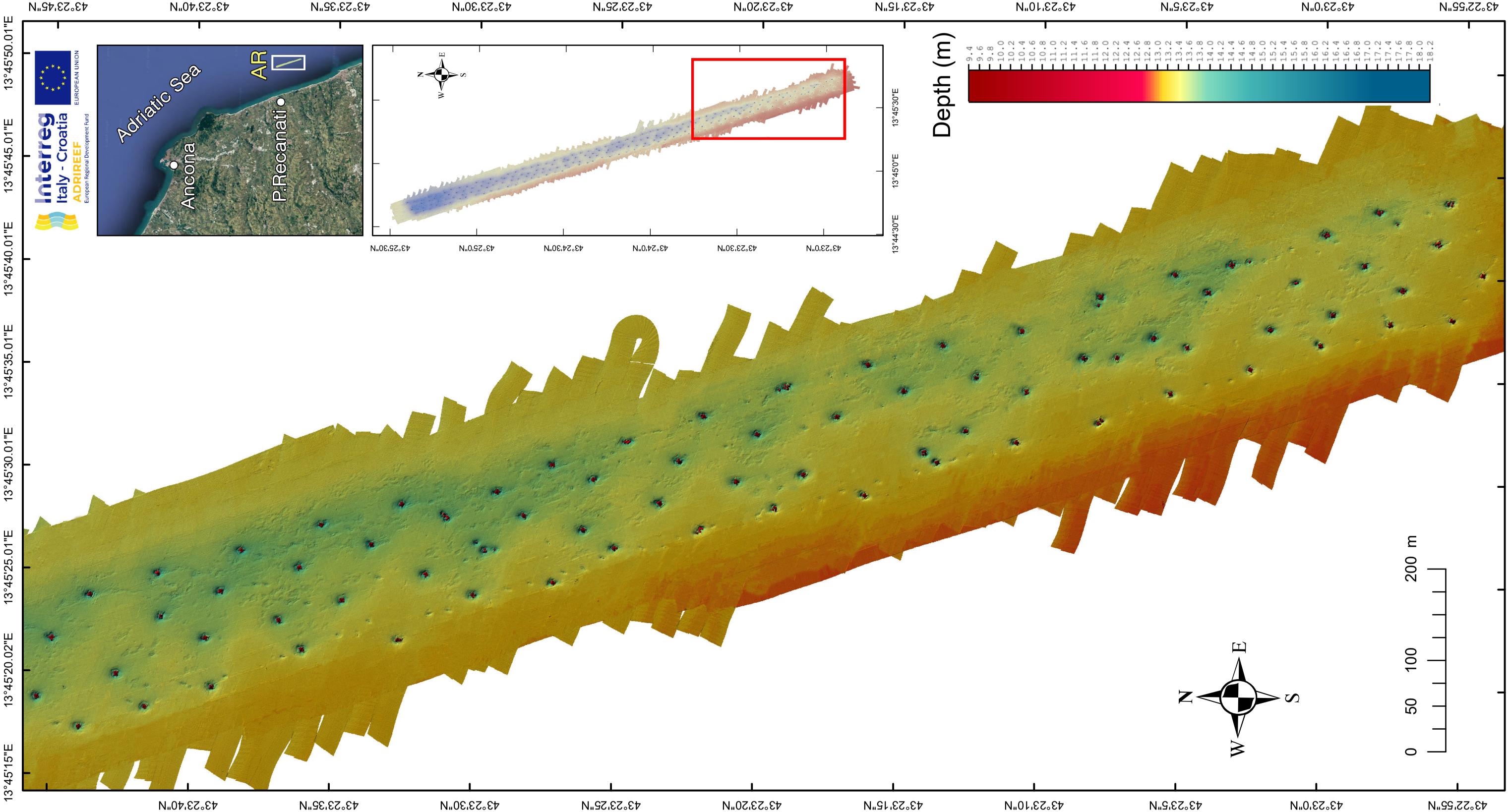
Interreg
Italy - Croatia
ADRIREEF
European Regional Development Fund
EUROPEAN UNION
Adriatic Sea
Ancona
P.Recanati
AR
Depth (m)
9.4
9.6
9.8
10.0
10.2
10.4
10.6
10.8
11.0
11.2
11.4
11.6
11.8
12.0
12.2
12.4
12.6
12.8
13.0
13.2
13.4
13.6
13.8
14.0
14.2
14.4
14.6
14.8
15.0
15.2
15.4
15.6
15.8
16.0
16.2
16.4
16.6
16.8
17.0
17.2
17.4
17.6
17.8
18.0
18.2
N
E
S
W
0
50
100
200 m
13°44'30"E
13°45'0"E
13°45'30"E
43°23'0"N
43°24'0"N
43°24'30"N
43°25'0"N
43°25'30"N
13°45'15"E
13°45'20.02"E
13°45'25.01"E
13°45'30.01"E
13°45'35.01"E
13°45'40.01"E
13°45'45.01"E
13°45'50.01"E
43°22'55"N
43°23'0"N
43°23'5"N
43°23'10"N
43°23'15"N
43°23'20"N
43°23'25"N
43°23'30"N
43°23'35"N
43°23'40"N
43°23'45"N

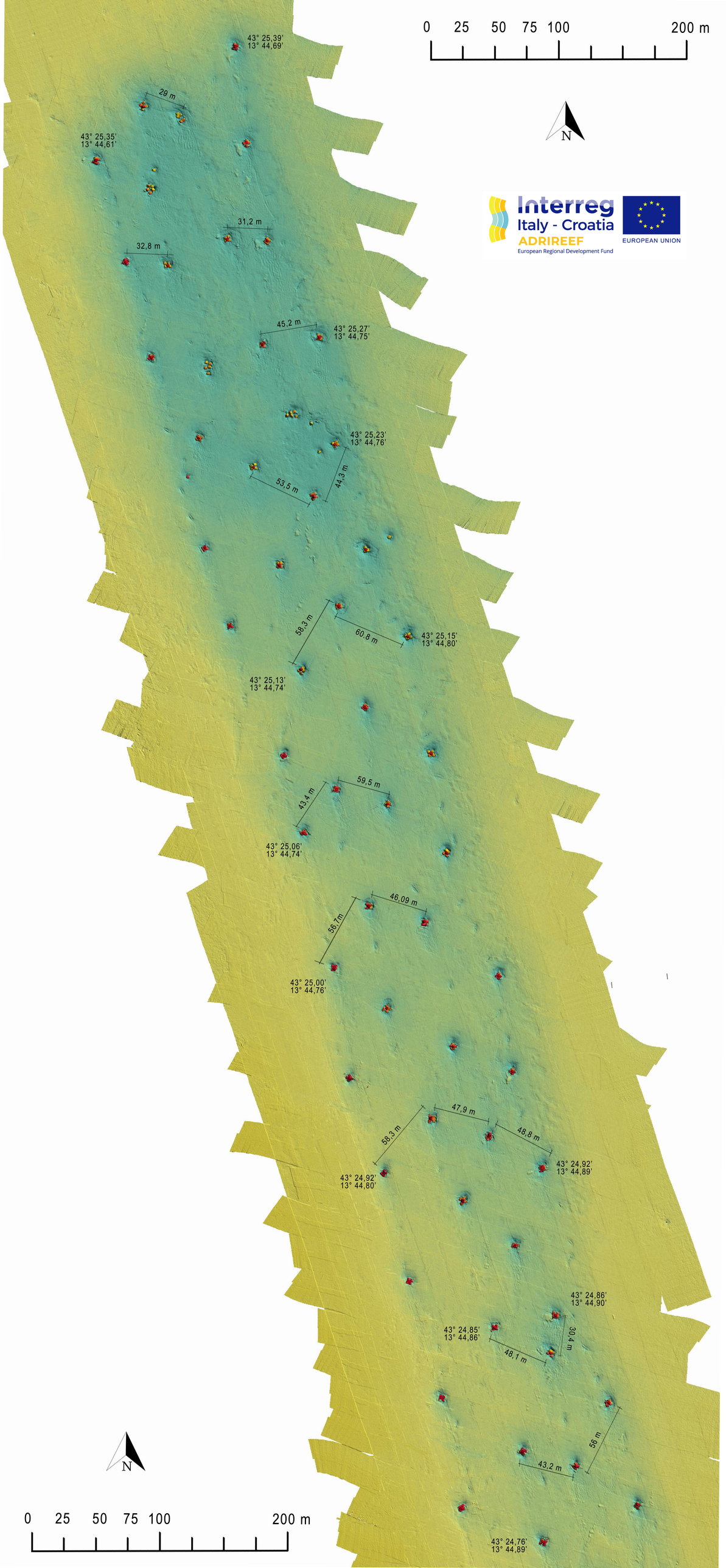
0 25 50 75 100 200 m
N
Interreg
Italy - Croatia
ADRIREEF
European Regional Development Fund
EUROPEAN UNION
43° 25,39'
13° 44,69'
29 m
43° 25,35'
13° 44,61'
31,2 m
32,8 m
45,2 m
43° 25,27'
13° 44,75'
43° 25,23'
13° 44,76'
53,5 m
44,3 m
58,3 m
60,8 m
43° 25,15'
13° 44,80'
43° 25,13'
13° 44,74'
59,5 m
43,4 m
43° 25,06'
13° 44,74'
46,09 m
56,7m
43° 25,00'
13° 44,76'
47,9 m
58,3 m
48,8 m
43° 24,92'
13° 44,89'
43° 24,92'
13° 44,80'
43° 24,86'
13° 44,90'
43° 24,85'
13° 44,86'
30,4 m
48,1 m
56 m
43,2 m
43° 24,76'
13° 44,89'
N
0 25 50 75 100 200 m